NORTHWESTERN UNIVERSITY

Investigation of Non-Innocent Ligands as Platforms for Studying Mixed Valency

A DISSERTATION

SUBMITTED TO THE GRADUATE SCHOOL
IN PARTIAL FULFILLMENT OF THE REQUIREMENTS

for the degree

DOCTOR OF PHILOSOPHY

Chemistry

By

Cole Carter

EVANSTON, ILLINOIS

December 2022

Abstract

Synthesis and characterization of mixed valent molecules which contain two or more metals in different oxidation states is a rich field of chemistry informing fundamental electronic structure and electron transfer theories. Traditionally these studies are concerned with the direct electronic interaction between metals, but recent work on redox non-innocent ligands has shown that forms of "metal-organic" mixed valency are prevalent but understudied. Using a redox non-innocent ligand as a bridging ligand for a mixed valent system allows investigation of this metal-organic delocalization in the context of the metal-metal interactions. In chapter two the effect of a trinuclear mixed valent system with a delocalized bridging ligand is investigated by permuting the c coordination chemistry of one of the metals and observation that this had little to no effect on mixed valent properties owing to the strong ligand based nature of the delocalization. In chapter three the effect of metal ionic radius and the consequent change in coordination sphere size is investigated for how it affects the bridging ligand geometry. Because molecular geometry is intimately connected to electronic states for mixed valent compounds, this consequently *does* influence the mixed valent properties of complexes, as seen through increase in NIR charge transfer intensity when small metals that enforce more rigidity are employed.

Acknowledgment

Nobody succeeds alone, and that is especially true for a PhD. I've found many adopted social and academic families that have given me invaluable support and advice through the years. A vibrant online community of scientists have provided extremely helpful technical advice out of their free time—the names of these folk is too long to enumerate. It is no hyperbole to say this thesis would not be possible without the networking and conversations I have obtained outside of Northwestern, particularly though online platforms. To those kind souls I am deeply indebted and hope to pay it forward for those who follow behind me.

In addition to my advisor, Tobin marks, I also need to thank Alex Mason, Jake Rothbaum, Rachel Dicken, and Yosi Kratish for social support and productive scientific conversations. Outside our group, I also need to thank Alexandra Berl, Eliot Woods, Alex Tamerius, Zoha Syed, Andrew Rosen, and Alexandra Barth for giving me outside perspectives that stimulated exciting new ideas, as well as technical advice for new experiments. I appreciate my "stupid questions" being answered fully and deeply.

I also need to personally thank Craig Fraser, Tim Dreier, Nick Randell, Dani Arias-Rotondo, Lyndsay Kissel, Zeus de los Santos, Dan Kurtz, Paul Lummis, Theo Rusmore, and Ross Koby. Especially during a pandemic, finding a supportive close group of friends who understand the trials and tribulations of a PhD is challenging. Thank you for all your support, it helped bring me to the finish line.

Table of Contents

List of Tables

List Schemes

List of figures

Chapter 1

Introduction to mixed valency and redox non-innocence

1 Chapter 1

1.1 Introduction to Electronic Coupling

Studying the connection between molecular and electronic structure is a cornerstone of chemistry, and presents many avenues of study that are of both applied and fundamental interest. Many molecules, especially organic molecules, are well-described by Lewis Theory and can be interpreted by inspection by assigning mostly localized bonds and using resonance and induction arguments to describe molecular properties. However, highly delocalized molecules often exhibit electronic structures that are harder to parse by inspection owing to the large number of orbital interactions and π bonds that are closely spaced in energy, which makes analysis difficult. This is particularly true in inorganic systems where the frontier orbitals have symmetry for many types of bonding interactions. Yet knowing the character of these bonds is crucial to understanding structure and reactivity. One notable complication that makes understanding delocalized inorganic structures challenging is the phenomenon of electronic coupling. Within chemistry, the concept of coupling is the realization that two molecular fragments, atoms, or sub atomic particles (e.g., electrons or nuclei) can intimately affect the properties of each other. Many frontiers of scientific theory and technological advancement depend on coupled phenomena. As an example, quantum computation research often exploits the coupling between electron magnetic spins as a way of carrying out operations. This is because the interdependence of bits on each other results in an exponential scaling in computational power instead of the linear scaling in traditional computers. This magnetic coupling is well-explored in the molecular magnet literature and is a continued field of inquiry. Electronic coupling, where the electronic state of one atom influences the electronic

state at a distant atom, has been intensely studied since the 1950's and led to the development of Marcus theory to explain electron transfer.

1.2 Introduction to Mixed Valency

While electron transfer and electronic coupling can be found in many systems, the typical systems for study are mixed valent inorganic complexes since they exhibit many unusual physical and electronic properties that cannot be explained without electronic coupling. Beyond curiosity and development of theory, mixed valency and electronic coupling are critical properties for diverse list of chemistries including quantum-dot redox catalysis, photovoltaics, and energy transfer in enzymes. By allowing sites separated far apart in space to interact without direct bonding interactions, electronic coupling allows for controlled energy transfer inside of, and between, complexes. Additionally, strongly electronically coupled metal systems delocalize d-electrons between multiple metals. When this interaction is intramolecular, the delocalization stabilizes unusual oxidation states and in the case of iron-sulfur clusters in proteins, allows for storage of electrons that can be released at particular gated events (e.g., conformational changes that allow for electrons to continue down a pathway). This type of electron buffer allows electron transfers to be carefully timed and orchestrated relative to each other. Photosynthesis, biological nitrogen reduction, and the respiration electron transport chain represent critical systems that rely on electronic coupling and gated electron transfers for their function.

1.3 Theory of Electronic Coupling

Electronic coupling is best explained broadly within chemical intuition before examining detailed physical underpinnings. Topically, electronic coupling can be understood in both Lewis and Molecular Orbital formalisms. In Lewis Theory, it can be considered as the resonance

interaction between two metals, and the degree of coupling is represented by how equally two structures contribute to the hybrid: e.g., how fully delocalized the electrons are between metals. In a molecular orbital Linear Combination of Atomic Orbitals (LCAO) approach, one can consider how equally weighted orbitals from each metal are in the frontier molecular orbitals. As coupling increases to the strong coupling limit, the frontier orbitals contain equal character from both metals (or equivalently, each resonance structure contributes equally to the hybrid). As a consequence of electrons delocalizing over both metals, electronic changes at one site influences properties at the other since the delocalized orbital can transmit perturbations.

There are 3 broad classes of mixed valent compounds, designated as class I, II, and III. Class I compounds exhibit no (or functionally no) electronic coupling. Formally, a class I compound cannot undergo electron transfer between metals, because a nonzero amount of electronic coupling is required for electron transfer. However, electronic coupling is geometry dependent and thermal energy can be enough to transiently adopt a geometry that imbues a small but nonzero amount of electronic coupling. For weakly coupled metals (class II), the metals are valence trapped and orbitals are mostly localized on each center. In such situations, formal oxidation states can be assigned and retain some meaning since electron counting still correlates to actual charge at the metal. In such compounds, the two metals form a donor-acceptor pair and can undergo charge transfer between them (termed a metal-metal or intervalence charge transfer). For symmetric complexes, there is no free energy change for an electron transfer between metals since there is no net change to the molecule since the metals are related by symmetry. However because the electron transfer causes a change in molecular dipole direction, the solvation sphere must reorient. Additionally, metal-ligand bond lengths and angles must shift to accommodate the new oxidation state. For this reason, while the electron transfer is energy neutral

thermodynamically (for symmetric molecules), there exists a barrier to electron transfer, which can be surmounted optically or thermally. As a consequence, the observed properties of class II compounds are temperature dependent, where they can form valence tautomers with discrete oxidation states at low temperature, but charge delocalized with indistinguishable metals at elevated temperature due to rapid electron transfer. Class III compounds, on the other hand, have orbitals that are fully delocalized between metals, formal oxidation states cease to have meaningful interpretations, though a formal non-integer oxidation state can be assigned. No metal-metal charge transfer occurs in class III compounds, but they adopt new photophysical properties that provide insight into the electronic structure.

More thoroughly, we can consider two states of a molecule with an extra electron residing on one metal or the other (M^{II}-(μ-L)-M^{III} and M^{III}-(μ-L)-M^{II}) and a reaction coordinate describing structural distortion required by the reorganization energy. In the absence of electronic coupling, the two states can be described as defined separately with their own wavefunctions, Ψ_a and Ψ_b and energies, G_a and G_b. They can be well described as separate non-interacting potential energy surfaces. In such cases, the system is class I mixed valency.

In the presence of weak electronic coupling (the class-II regime), however, there is interaction between the wavefunctions of metals that aren't directly bonded together. As such, treating the wave functions as separate entities ceases to be useful. Instead, the now interacting wave functions form a linear combination: $\Psi_1 = c_a\Psi_a + c_b\Psi_b$ and $\Psi_2 = c_a\Psi_a - c_b\Psi_b$. Where Ψ_1 is the new ground state, and Ψ_2 is the new excited state. However because of weak coupling, charge is mostly localized on one metal or the other, and the reaction coordinate has two minima that can be described with transition-state theory. This situation intersects closely with the Born-

Oppenheimer approximation, which states that electron distribution rapidly equilibrates during a slowly changing molecular geometry. As such, a slow change from a geometry that would otherwise be described by Ψ_a to a geometry that would be described by Ψ_b results in a continuously changing electronic structure, and a continuous potential energy surface must connect the two geometries: the electronic and geometric structures are said to be coupled. The energy of the new wavefunctions (G_1 and G_2 describing Ψ_1 and Ψ_2) depend not only on the linear combination of G_a and G_b, but a parameter H_{ab}, the electronic coupling constant. Two important consequences arise: the electrons at each metal can be delocalized between metals according to the relative weights of c_a and c_b, and there is now a Metal-Metal Charge Transfer (MMCT) that can be driven optically (by vertical excitation from Ψ_1 to Ψ_2), or thermally (by acquiring enough thermal energy to distort the geometry which then drives charge transfer).

In the case where metals are strongly coupled (the class III regime) where metal orbitals are fully delocalized there is a single geometry that describes the ground state, and the double well potential seen in the weakly coupled cases becomes a single well. In these strongly coupled class III compounds, no charge transfer available as there is no longer a source nor a sink of electrons.

1.4 Design of Mixed Valent Systems

Electronic coupling is most often studied within inorganic chemistry since metal centers are exceptionally versatile as both electron donors and acceptors. Most commonly this manifests in compounds featuring two (or more) metals—one in a higher oxidation state and one in a lower oxidation state. These “mixed-valence” compounds are particularly well suited for study because this produces a facile donor-acceptor pair that allows for a metal to metal charge transfer. Furthermore, since metals have flexible oxidation states they are amenable to the electron

withdrawing and donating effects of delocalizing charge across its ligands and potentially into another metal. When a ligand is highly conjugated, the electrons within the M-L bonding interaction are distributed not only between the metal and the donor atom, but also atoms several bonds away. In addition, metal centers are amenable to a wide host of spectroscopies, allowing for deep characterization of their electronic structure. While mixed valency has been studied across an uncountably many different metal pairs and structure types, ferrocene holds a privileged position within mixed valence research. The reason ferrocene is so often employed in mixed valent research is its well-studied electronic structure, well-behaved redox chemistry, lack of strong spin-orbit coupling, and synthetic accessibility makes it an exceptional model system.

By connecting two ferrocenes with a conjugated linker and modifying the linker with different electronics, lengths, geometries, etc., different parameters of molecular structure can be isolated to study their effect on the strength of electronic coupling and the consequential impact of coupling on electron-transfer properties. Subtle changes to the linker have surprisingly dramatic impacts on the degree of electronic coupling, leaving much left unexplored in terms of linker design despite decades of research. Beyond simple static geometries, another emerging area is experimental exploration of how ultrafast dynamics such as vibration and rotation affect electronic coupling. Such effects have been known to be important, as orbital overlap changes during thermal distortions. However, such dynamics are challenging to systematically explore, though emerging multidimensional and ultrafast techniques are graining traction.

In evaluating effective linkers, the frontier orbitals should be both highly delocalized, similar in energy to the metals they connect, and of the right symmetry for interacting with the metals. As abstracted design principles, these are highly reminiscent of ligand design for redox

non-innocent ligands. Redox-non-innocent ligands are ligands that render oxidation states of metals ambiguous either due to delocalization of metal d-orbitals over the ligand, or through redox tautomerism. Since non-innocent ligands have been heavily studied in recent years there is a wealth of characterizations and detailed synthetic procedures for many different structures. For these reasons, modifying redox non-innocent ligands to accommodate multiple metals and using them as connecting units for mixed valent studies is an auspicious strategy. In fact, non-innocent complexes can be considered a form of metal-organic mixed valency, which presents the opportunity to study organic fragments as redox partners participating in the coupling between metals. While such "three-state" systems are not unknown, the accompanying theory to rigorously describe systems with more than 2 coupled fragments is less studied compared to traditional 2-state systems.

Additionally, use of non-innocent ligands alleviates a significant difficulty with studying electronic coupling: coupling is highly dependent on a host of variables such as symmetry, substitution, conformation, orbital energies, symmetry, etc. These multitude of variables makes generating a series of isostructural and/or isolobal compounds challenging since one change in a molecule often affects multiple parameters. This problem is exasperated when attempting to design systems with high nuclearity and different multiple metal identities.

However, we resolve this difficulty by using the pyridine diimines (PDI) and pyrrole diimines (PyrDI) as bridging ligands. The flanking aryl groups can be exchanged for ferrocenes while retaining a binding site for an additional metal. In this way, the biferrocenyl mixed-valent compound acts as a ligand towards another metal, with the 3rd metal can be exchanged while keeping other molecular properties constant. PDI family has been studied extensively due to its

facile synthesis and its ability to stably occupy 4 redox states (from neutral to triple anion) as a pure organic apoligand. Its accessible redox activity increases further upon attachment to redox active metals. Furthermore, it features significant delocalization in its HOMO and LUMO, which causes complexes of PDI ligands to exhibit frontier orbitals that have both d-orbital and organic π character. Intriguing coordination chemistry and reactivity have been found with these complexes, which have been reviewed extensively elsewhere. Notably however, PDI ligands have more difficulty in tight binding to hard d^0 metals such as the lanthanides. Because lanthanides generally form labile bonds to neutral nitrogen donors, PDI-Ln complexes have some reversible binding. An interesting complement to the neutral PDI ligand, is its anionic cousin PyrDI. Because of the acidic pyrrolic proton, PyrDI binds to hard d^0 metals more tightly, whereas PDI is noted to feature more labile binding to lanthanide ions.

We became interested in using heterocyclic diimine ligands as connecting units for ferrocenes to make mixed valent compounds for several reasons:

1. Their modular synthesis and the ability to permutate multiple positions allows structural and electronic diversity
2. As a tight-binding ligand, it allows a 3rd metal to be incorporated into the mixed valent system, affording easy access to a 4-state system
3. Frontier orbitals are localized in prime positions for overlap with ferrocene orbitals
4. All 3 metals would be connected by few bonds, enhancing to likelihood of electronic coupling

The ability to exchange the metal in the central binding pocket allows for exploring four-way electronic coupling between different metal identities, and between those metals and the organic

pi-system. Extending the nuclearity or evaluating the effects of perturbing a mixed-valent system is generally challenging because it is difficult to install new metals without changing either the conformation or internuclear distance (both important parameters in electronic coupling).

Chapter 2

Bis-Ferrocenyl-Pyridinediimine Trinuclear Mixed-Valent Complexes with Metal-Binding Dependent Electronic Coupling: Synthesis, Structures, and Redox-Spectroscopic Characterization

Portions of this chapter appear in the following publication:

J. Am. Chem. Soc 2020, 142, 43, 18715–18729

2.1 INTRODUCTION

Traditional paradigms in understanding the reactivity of coordination complexes focus predominantly on metal identity and formal oxidation state.[1] In catalysis, the metal center is conventionally viewed as the primary site of reactivity, and this metal-centric view is fruitful when the metal center's properties and it's interactions with substrates can be reliably predicted—as is often the case in second- or third-row transition metals where strong ligand fields tend to localize frontier orbitals on either the metal or ligand.[1, 2] However there is growing recognition that this view is not generalizable to all complexes,[3] particularly those of first-row metals with highly conjugated ligands.[4] The combination of weak ligand fields and highly delocalized frontier orbitals generates complexes with properties not uniquely defined by metal identity and oxidation state, as the frontier orbitals involve substantial mixing with the π-ligand backbone.[5, 6] As such, these catalytic systems can be viewed as electronically coupled between metal and ligand—as delocalization of frontier orbitals across metal and ligand causes changes at one site to perturb chemistry at the other.[7]

An increasing number of catalysts take advantage of such "non-innocent" ligands[8-10] that are electronically coupled to metal centers. Although most ligands can become "non-innocent" under the right conditions,[4, 7] the pyridinediimine ("PDI"; **Scheme 2.1**) ligand family has become a prominent example in non-innocent ligand catalysis.[11-14] PDI ligands can act as electron reservoirs to store electrons or other reducing equivalents (e.g. hydrides or alkyls at electrophilic sites)[15] during catalytic cycles,[10, 16-21] permitting first-row metal complexes to both emulate the 2-electron chemistry of noble metals, as well as access highly reduced states.[10] While the reactivity of such metal-ligand coupled systems has been extensively studied, challenges remain in defining electron localization/delocalization throughout the complex, and reliably predicting which

scaffolds will exhibit strong delocalization. Such questions are core to the study of mixed-valent compounds, which contain multiple metal centers in different oxidation states connected by π-linkers that serve as a conduit for delocalization.[22-25] Diverse spectroscopic and theoretical tools have been developed for quantifying and characterizing the degree of coupling and delocalization in mixed-valent systems such as NMR, XPS, EPR, UV/vis-NIR, CV, DSC, Mössbauer, and IR/Raman techniques.[20, 24-27]

Mixed-valent compounds have attracted attention from both physical and synthetic chemists for their interesting electronic structures and electron transfer properties, resulting in a wide diversity of synthetic and structural data to utilize in catalyst design.[25] The impetus for such longstanding interest is driven by potential applications in molecular wires,[28-30] nonlinear optics,[31, 32] catalysis,[33-35] and testing models for electron transfer.[36, 37] However the application of mixed-valency in structures capable of acting as ligands towards other transition metals is rare. Indeed, there is great interest in metal-ligand redox and reactivity cooperativity and metallo-ligand mediated electronic coupling between metals in the chemistry community. Despite interest, the application of mixed valency towards exploring the effects of electronically coupled bi-nuclear scaffolds that could be applied to catalysis has been challenging,[38-40] due to issues of A) chemical stability in different redox states;[41] B) establishing clear design criteria for engendering strong coupling, as similar structures often exhibit different coupling strengths as a result of the balance between geometric and electronic factors that lead to coupling;[23, 42-44] and C) designing scaffolds that are modular enough to retain coupling while parameterizing steric and electronic properties to optimize catalysis.

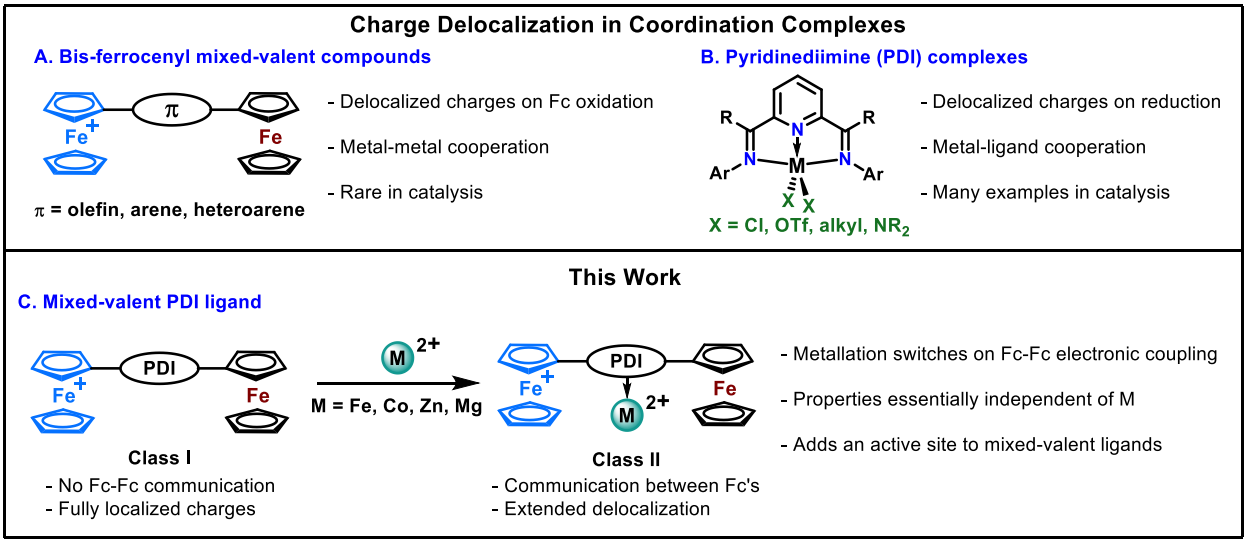

Scheme 2.1. Generic bis-ferrocenyl and PDI complexes, and guiding design of a bis-ferrocenyl PDI complex.

Most mixed-valent catalysts capitalize on cooperative effects between metals that have different chemistries in different oxidation states (e.g. using Class-I mixed-valent structures with little to no delocalization between metals), or otherwise do not well characterize the effect of metal delocalization on reactivity.[39, 45, 46] However, work in direct metal-metal interactions between ferrocene and d^0 metals has revealed promising electronic structures and catalytic activity.[47-54] We are exploring electronically coupled metal sites as an opportunity to engineer gated electron transfer and multi-electron redox events, binuclear mechanisms, strong electric field gradients, and other properties that feature prominently in efficient biological and abiotic catalysts.[55] Despite this open question in inorganic chemistry, mixed valent motifs with known Class-II or -III behavior exist prominently in biological systems. Notably, iron-sulfur clusters are ubiquitous in proteins and serve as both electron buffers and electron-transfer conduits for intermediates in enzymatic catalysis.[56-60] Given mixed valency's ubiquity in nature, inorganic catalysis could benefit from the

detailed study of how electronic coupling affects catalyst structure and reactivity. Under this lens, mixed valency provides an opportunity to explore chemical space in non-innocent ligand catalysis while capitalizing on well-characterized electronic structures, synthetic strategies, and established theoretical frameworks. Nevertheless, such systems are challenging to create in a reliable, modular way, and the chemical space explored remains insufficient to deduce general principles.[39, 41, 42, 61-66]

Thus, we sought to construct ferrocene-based ligand frameworks with well-understood electronic structures to better characterize the interactions between metals and their mechanisms of interaction. The PDI ligand structure (**Scheme 1.1**) was targeted because heteroaromatics such as pyrrole and pyridine are known to enhance coupling between ferrocenyl groups.[23, 43, 67, 68] Furthermore, both ferrocenes and the central metal share bonding with the imines, providing short through-bond connectivity, and a low-lying π* network[13] to mix the metal orbitals—both important for strong electronic communication.[22, 69, 70] Note that thus far only the main group coordination chemistry of ferrocene-substituted PDI ligands has been reported,[71, 72] and the transition metal chemistry remains unexplored. Here we report the synthesis, solid state structural, and spectroelectrochemical characterizations of a series of s- and d-block ferrocenyl PDI ("Fc_2PDI") complexes (Scheme 1). Intriguingly we find the electronics of these complexes to be largely independent of the central metal ion identity, yet that metal binding is required for coupling between ferrocenes. This finding is further explained by DFT computation, showing that the frontier orbitals are primarily ferrocene- and PDI- based, featuring little MCl_2 character. Electronic characterizations suggest that M(II) binding stabilizes the ligand π-system which increases mixing of the Fc moiety and imine π-orbitals, providing a conduit for delocalization. Notably a 3-state IVCT mechanism involving mutual coupling from the Fc units to the pyridine aryl system in the

excited state is suggested as the mode of coupling. Furthermore, crystallography and DFT analysis performed on the mixed valent (Fc/Fc^{+}) and doubly oxidized (Fc^{+}/Fc^{+}) species indicate significant structural changes upon oxidation, which may limit the degree of coupling but presents the Fe(III) ferrocenium close to the MCl_2 center, suggesting opportunities for catalysis.

2.2 Synthesis and Characterization of PDI Complexes

Synthesis. The **Fc_2PDI** ligand synthesis was modified from literature[73, 74] to streamline the procedure (**Scheme 2.2**). Ferrocene can be selectively mono-lithiated using *t*-BuLi and *t*-BuOK, which was trapped with iodine to afford iodoferrocene (FcI) as a black oily crude that may crystallize on standing if sufficiently

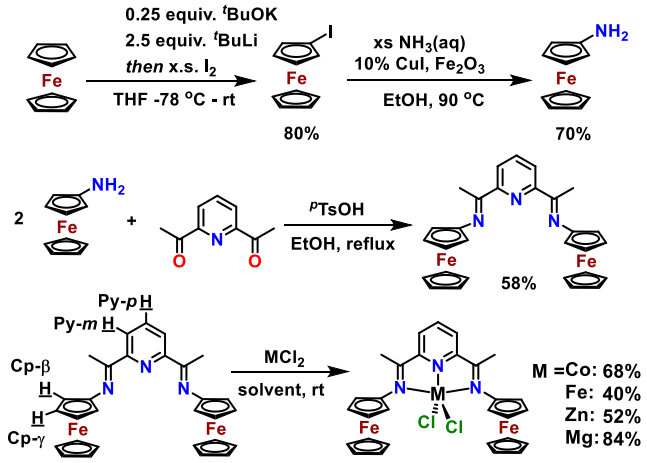

Scheme 2.2. Synthesis of the **Fc_2PDI** ligand and **$(Fc_2PDI)MCl_2$** complexes.

pure. After purification through a silica plug and removal of unreacted ferrocene by sublimation (100 °C, 0.1 Torr), pure product was obtained as dark orange needles in 80% isolated yield on scales up to 15 g. Amination of FcI with aqueous ammonia using a Fe_2O_3/CuI catalyst system was carried out following a literature procedure,[74] while the amino ferrocene ($FcNH_2$) was purified by sublimation (90 °C, 0.1 Torr) instead of chromatography. Note that $FcNH_2$ gradually decomposes in air to an NMR indistinguishable ($CDCl_3$) brown solid (presumably the n-oxide) at ambient

temperature, and therefore should be stored in the freezer under inert atmosphere or in a glovebox. Purification can be readily achieved by sublimation or passage through an alumina plug with hexanes/EtOAc elution (1:1). $FcNH_2$ was condensed[75-77] with diacetyl pyridine under reflux in dry degassed ethanol with a catalytic amount of *p*-TsOH to afford the air-stable product as a microcrystalline solid. The color of the product ranges from bright red to maroon depending on purity, crystallinity, and crystal polymorph (cations and acids can be coordinated and impart purple coloration). **Fc_2PDI** was isolated in 58% yield as red/purple microcrystals by filtration and washing with cold ethanol. If required, **Fc_2PDI** can be recrystallized by DCM/pentane layering.

Next, the Co, Fe, Zn, and Mg complexes of the **Fc_2PDI** ligand were prepared by direct metallation with corresponding MCl_2 precursors, in decent to good isolated yields (**Scheme 2.2**). Note that in our hands, we experienced high levels of static electricity which can result in somewhat diminished isolated yields on small scales. The rate of metallation varies with solvent for each MCl_2 species—presumably due to solubility considerations. $ZnCl_2$ and $CoCl_2$ react readily with 1.0 eq of the ligand overnight in DCM affording blue-purple crystalline complexes. For $FeCl_2$ and $MgCl_2$, the metallation is prohibitively slow in DCM and requires THF or MeOH for metallation to occur. All complexes were purified by trituration with ether or recrystallization from layered DCM/ether solvent to yield dark blue/purple solids. The complexes exhibit varied stabilities under ambient conditions, as the **(Fc_2PDI)$CoCl_2$** and **(Fc_2PDI)$ZnCl_2$** complexes are reasonably resistant to small amounts of air and moisture for days, while solutions of **(Fc_2PDI)$FeCl_2$** turn brown and precipitate overnight, and **(Fc_2PDI)$MgCl_2$** turns red immediately on exposure to moisture.

CV experiments (**Figure 2**) indicate that oxidation occurs at similar potential to ferrocene, rendering the slightly more oxidizing actylferrocenium and Ag^+ salts as suitable oxidants to

generate the mixed valent species. Initial attempts to oxidize with $AgPF_6$ were hindered by high insolubility of the product PF_6^- salt, preventing further characterization. However, careful layering of a DCM solution of **$(Fc_2PDI)CoCl_2$** on top of a DCM solution of $AgPF_6$ inside an NMR tube slowed the reaction enough to allow precipitation to occur in the form of single crystals suitable for diffraction. Attempts with other complexes yielded crystalline material not suitable for single crystal X-ray diffraction studies. Using $BArF^-$ salts to improve solubility presented unpredicted complications, as multiple attempted oxidations of **$(Fc_2PDI)FeCl_2$** with 1 equiv. of [AcFc][BArF] in DCM resulted in a black solution, which was dried and washed with pentane to remove acetylferrocene byproduct, and used directly for crystallization. Interestingly the dication, **$[(Fc_2PDI)FeCl_2][BArF]_2$**, rather than the expected monocation, crystallizes from the solution as X-ray suitable crystals (**Figure 2.1F**). We believe that a small equilibrium amount of the dication is present due to intermolecular electron transfer (disproportionation constant: $K \sim 0.001$ based on 200 mV separation between first and second oxidations—see electrochemistry below). The dication likely preferentially crystallizes in the nonpolar DCM solvent, permitting isolation in a similar way to crystallization of $MgMe_2$ through the Schlenk equilibrium of Grignards.[78, 79] We emphasize that the mixed-valent species are stable in solution, indicated by CV and spectroelectrochemistry.

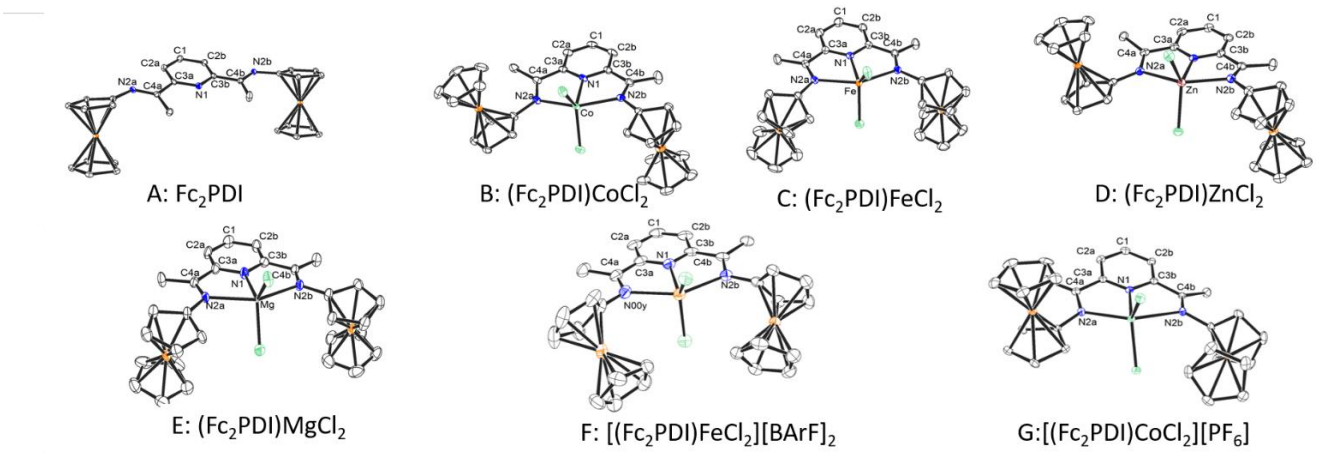

Figure 2.1. Single-crystal X-ray structures for the free ligand, $(Fc_2PDI)MCl_2$ (M = Co, Fe, Zn, Mg), and oxidized $(Fc_2PDI)MCl_2$ (M = Fe, Co) complexes. Thermal ellipsoids are drawn at 50% probability. Hydrogen atoms and solvent molecules are omitted for clarity. For structure F and G, $BArF^-$ and PF_6^- anions are omitted, respectively.

NMR Spectroscopy. While **$(Fc_2PDI)FeCl_2$** and **$(Fc_2PDI)CoCl_2$** are paramagnetic and did not provide informative NMR spectra, the comparison of the free ligand with the corresponding diamagnetic complexes **$(Fc_2PDI)MgCl_2$** and **$(Fc_2PDI)ZnCl_2$** affords interesting insight into the change in magnetic and electronic environment upon coordination. The *para*-pyridyl protons of the Mg and Zn complexes appear as apparent doublets of doublets rather than triplets, due to second order effects.[80, 81] The Cp protons shift substantially downfield upon metallation, from δ 4.46 to 5.13 ppm for β-Cp protons, and δ 4.26 to 4.51 ppm for γ-Cp protons distal to the imine (**Table 2.1**; **Scheme 2.2**). Notably, asymmetry in ferrocene Cp magnetic environment (e.g., different resonance frequencies for different Cp protons) has been previously assigned to differential occupation of the d_{xy}/d_{x2-y2} and d_{xz}/d_{yz} orbitals caused by donation into or withdrawal from the Fc center.[47, 54, 82, 83] The pyridyl region also exhibits substantial changes, but interestingly with opposite shift trends for *meta* and *para* protons. Upon coordination, the pyridyl *meta* protons

shift upfield from δ 8.29 to 8.13 ppm, while the *para* protons shift downfield from δ 7.81 to 8.29 ppm (**Table 2.1**). Different shielding effects on the *meta* and *para* protons might be explained given that the pyridine based frontier orbitals are largely bonding with respect to the *ipso* and *meta* carbons, but antibonding with respect to the *meta* and *para* carbons.[17, 19, 84, 85] That is, the different magnetic response at each position may reflect different bonding character at each position. However, the crystallographic data (*vide infra*) suggest that rotational freedom about the C_{ipso}-C_{imine} bond produces an "open" conformer (**Figure 2.1A**) and a "closed" conformer (**Figures 2.1B-G**). These conformational changes may also impact the observed chemical shifts, though symmetry (e.g. relative overlaps should be conserved) suggests that orbital interactions and therefore electronic communication should not change between conformers.

Table 2.1. ^{1}H NMR Chemical shift data (ppm) for selected resonances of **Fc_2PDI**, **(Fc_2PDI)$ZnCl_2$**, and **(Fc_2PDI)$MgCl_2$** in CD_2Cl_2 at 25 °C.

	Fc_2PDI	**(Fc_2PDI)$ZnCl_2$**	**(Fc_2PDI)$MgCl_2$**
Py-*4*	7.81	8.29	8.29
Py-*3*	8.27	8.13	8.07
Cp-*2*	4.46	5.13	5.11
Cp-*3*	4.26	4.51	4.52

Solid State Structures. Single crystals of (Fc_2PDI)MCl_2 (M = Fe, Co, and Zn) complexes suitable for X-ray diffraction studies were grown from DCM/pentane, while diffraction quality crystals of the Mg complex were grown from DCM/Et_2O. **[(Fc_2PDI)$CoCl_2$][PF_6]** was crystallized

by layering DCM solutions of $AgPF_6$ and **$(Fc_2PDI)CoCl_2$**, while crystals of **$[(Fc_2PDI)FeCl_2][BArF]_2$** were grown from DCM/pentane layering of the crude reaction product prepared by treatment of **$(Fc_2PDI)FeCl_2$** with one equivalent of [AcFc][BArF] in DCM. Refinement statistics are summarized in the Supporting Information (**Tables A.1 and A.2**). Crystal structures are shown in Figure 1 and key structural characteristics are compared in Table 2. All structures have eclipsed ferrocene conformations. The complexes all exhibit slight deviations from Cp-PDI-Cp coplanarity, with torsions between the Cp-imine planes on the order of 7°-30°, which may reflect crystal packing forces.[22, 30, 68, 86, 87] The Zn and Co structures also exhibit a distortion of the PDI backbone, manifested as a puckering of the imine carbons above and below the ligand plane. Interestingly, in contrast to other PDI complexes that generally have coordination geometries approaching square pyramidal,[85] all structures in this study are distorted trigonal bipyramidal. The ligand bond lengths in all the neutral complexes are essentially equivalent (within the given ESD for each bond) and consistent with a neutral ligand bound to a M(II) fragment.[16] The free ligand adopts an "open" conformation in the solid state, likely due to steric factors. The mixed valent **$[(Fc_2PDI)CoCl_2][PF_6]$** shows a break in symmetry, as the oxidized ferrocene swings to be nearly orthogonal (83°) to the backbone plane. The site of oxidation is assigned by slight contraction of the Fe-Cp distance, and high numbers of close cation-anion distances on inspecting the extended crystal packing which features a sheet of alternating ferrocenium cations and PF_6^- anions (see SI). Furthermore, the imine connected to this ferrocenium contracts slightly, and the $CoCl_2$ center drifts away from the ferrocenium arm. These changes on oxidation suggest a weaker degree of coupling, as differences in coordination geometry between metal sites leads to large reorganizational energies, and higher barriers to electron transfer.[24]

We point out that stronger ion pairing is known to stabilize localized cations and weaken coupling, motivating crystallization with $BArF^-$ anions. While the monocationic $BArF^-$ salt could not be crystallized, the doubly oxidized structure, **$[(Fc_2PDI)FeCl_2][BArF]_2$** shows both ferrocenes canted nearly orthogonal (85°) but a more symmetric coordination environment about the $FeCl_2$ center.

Table 2.2. Selected bond distances (Å) and bond angles (deg) for Fc_2PDI ligand and **$(Fc_2PDI)MCl_2$** complexes (M = Zn, Co, Fe, and Mg). "Cp torsion" is measured between planes defined by the Cp ring and the Cp_α-N_{im} and C_{im}=N_{im} bonds.

Key bond lengths and angles			
Fc_2PDI			
C_4-N_2	1.285(2)	Cp torsion[a]	22.7°
			28.1°
$(Fc_2PDI)MgCl_2$			
N_1-Mg	2.0907(2)	N_{2a}-Mg-N_{2b}	148.19°
N_{2a}-Mg	2.2826(2)	Cp torsion[a]	13.4°
N_{2b}-Mg	2.2518(2)		13.9°
C_4-N_2	1.2909(1)	Cl-Mg-Cl	124.95°
$(Fc_2PDI)ZnCl_2$			
N_1-Zn	2.044(3)	N_{2a}-Zn-N_{2b}	150.00 °

Key bond lengths and angles			
N_{2a}-Zn	2.304(3)	Cp torsion[a]	17.63°
N_{2b}-Zn	2.255(3)		14.91°
C_4-N_2	1.289(4)	Cl-Zn-Cl	124.28°
$(Fc_2PDI)FeCl_2$			
N_1-Fe	2.067(2)	N_{2a}-Fe-N_{2b}	149.1°
N_{2a}-Fe	2.227(2)	Cp torsion[a]	18.8°
N_{2b}-Fe	2.262(2)		13.5°
C_4-N_2	1.289(3)	Cl-Fe-Cl	125.7°
$(Fc_2PDI)CoCl_2$			
N_1-Co	2.003(2)	N_{2a}-Co-N_{2b}	152.98°
N_{2a}-Co	2.222(2)	Cp torsion[a]	29.49°
N_{2b}-Co	2.199(2)		8.98°
C_4-N_2	1.294(3)	Cl_1-Co-Cl_2	127.40°
$[(Fc_2PDI)CoCl_2][PF_6]$			
N_1-Co	2.01247(8)	N_{2a}-Co-N_{2b}	150.94°
N_{2a}-Co	2.37077(8)	Cp torsion[a]	4.18°
N_{2b}-Co	2.17412(8)		95.32°
C_4-N_2	1.28654(5)	Cl_1-Co-Cl_2	118.37°
	1.27531(5)		

Key bond lengths and angles

[(Fc$_2$PDI)FeCl$_2$][BArF]$_2$			
N_1-Fe	2.07669(4)	N_{2a}-Fe-N_{2b}	148.45°
N_{2a}-Fe	2.29128(5)	Cp torsion[a]	65.82°
N_{2b}-Fe	2.28597(5)		76.07°
C_4-N_2	2.29128(5)	Cl_1-Fe-Cl_2	130.25°
	2.28597(5)		

Electrochemistry. Due to the highly reversible and stable Fc/Fc^+ redox couple, electrochemistry is an informative tool in evaluating electronic communication between Fc groups.[22, 25] For symmetric, uncoupled Fc sites, a single concerted oxidation wave is expected. However, if oxidation of one Fc perturbs the electronic environment of the second, i.e., the metal centers are coupled, then the second oxidation occurs at increased potential, resulting in sequential waves. There are multiple mechanisms that can give rise to split redox waves,[22, 24, 27] and the observed ΔE is a net sum of: $\Delta E_{obs} = \Delta E_{resonance} + \Delta E_{electrostatic} + \Delta E_{statistical} + \Delta E_{inductive} + \Delta E_{exchange}$. Due to the difficulty in delineating individual contributions to ΔE, it is challenging to quantitatively assess delocalization by CV.[27] However, since the exchange and statistical terms are typically small (~36 mV at 25°C)[22] and inductive effects are often assumed small for ferrocenes separated by multiple bonds, electrostatic and resonance effects typically dominate the observed $\Delta E_{1/2}$. Furthermore, because electrostatic effects are dependent on geometry, solvent, and electrolyte; an isostructural series of compounds enables more direct evaluation of delocalization. Thus, the separation between ligand oxidations can be correlated as a function of metallation (e.g., with

$FeCl_2$, $CoCl_2$, $ZnCl_2$, or $MgCl_2$) with the delocalization of charge between the two ferrocene groups.[22, 23, 43]

With these considerations in mind, CV was performed in DCM because coordinating solvents promote ECE mechanisms in PDI complexes,[88] while TBA-BArF electrolyte was employed both to improve the electrochemistry in this nonpolar solvent,[89] and also because the PF_6^- salts of these complexes are insoluble, precipitating onto the electrode. **Figure 2.2** shows that the free ligand displays a concerted two-electron wave, suggesting weak to no coupling. Most complexes show sequential 1 e^- waves separated by ~200 mV (**Table 2.3**). Notably **(Fc$_2$PDI)FeCl$_2$** exhibits a larger $\Delta E_{1/2}$ by 60 mV. The first oxidation is approximately isoenergetic with free Fc in these compounds ($E_{1/2}$ = 590 mV vs Cp^*_2Fe for Fc),[90] which suggests that the Fc-based occupied orbitals are not substantially perturbed. Upon complexation, the oxidation shifts slightly to higher potential--an additional 20-40 mV higher potential than **Fc$_2$PDI**, reflecting Fc bonding orbital stabilization. Reductions and oxidations are assigned as primarily be ligand-based, since Zn(I)[91] and Zn(III)[92] species are implausible, and the free ligand decomposes at -1.5 V. Note that no additional redox couples are observed within the DCM solvent window of -1.5 V to 1.5 V. We propose that when a central metal is coordinated by **Fc$_2$PDI**, the reduced ligand is stabilized in solution. Note that the **(Fc$_2$PDI)FeCl$_2$** compound exhibits the largest ΔE, suggesting it for spectroelectrochemical investigation (*vide infra*).

UV-vis Spectra. Because CV data cannot unambiguously assign the reason for underlying sequential oxidation, redox splitting can be misleading in assessing electronic coupling.[27] Therefore it is more prudent to combine electrochemical data with optical spectroscopy, through both traditional and spectroelectrochemistry experiments. The visible electronic transitions in ferrocene are best considered d-d transitions,[93, 94] so by exploiting the well understood electronic

spectrum of ferrocene, the Fc d-orbital mixing can be tracked as a perturbation of the relevant d-d transitions. For consistency, we refer to the visible region band as "the ferrocenyl band" to remain agnostic as to its character, i.e., d-d, charge transfer (CT), or overlapping d-d and CT transitions. Furthermore, we differentiate between the ferrocenyl iron and the organic pyridine parts of the ligand when describing "metal" versus "ligand" centered processes. The UV-visible spectra of the **Fc_2PDI** ligand and its **$(Fc_2PDI)MCl_2$** complexes were recorded in DCM, using amino ferrocene ($FcNH_2$) for comparison.

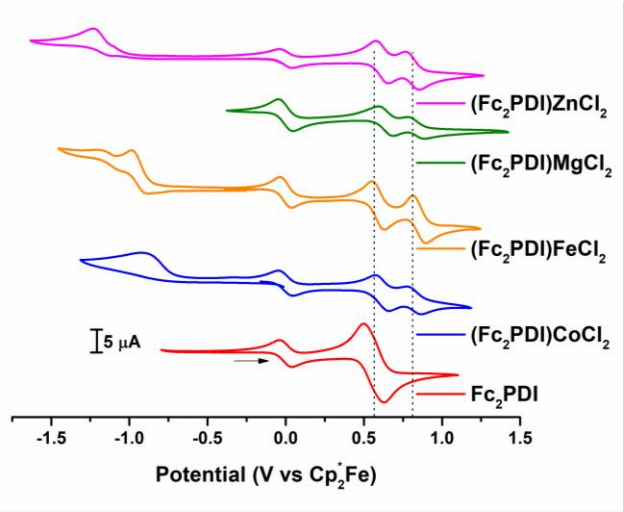

Figure 2.2. Cyclic voltammograms of **Fc_2PDI**, **$(Fc_2PDI)FeCl_2$**, **$(Fc_2PDI)CoCl_2$**, **$(Fc_2PDI)ZnCl_2$**, and **$(Fc_2PDI)MgCl_2$** (bottom to top); scan rate: 100 mV/s; 1 mM analyte, 100 mM TBA-BArF in dry degassed DCM under N_2 at 25° in the dark. CVs are referenced to Cp^*_2Fe internal standard at 0.0 mV.[95] Dotted lines at 564 mV and 810 mV correspond to **Fc_2PDI** and **$(Fc_2PDI)ZnCl_2$** oxidations for comparison. Reduction waves not presented for **Fc_2PDI** and **$(Fc_2PDI)MgCl_2$** due to rapid decomposition and electrode fouling.

Table 2.3. Cyclic Voltammetry data for **(Fc$_2$PDI)MCl$_2$** (M = Co, Fe, Mg, Zn), values in mV vs Cp*$_2$Fe.

Compound	1st $E_{1/2}$[a]	2nd $E_{1/2}$[a]	$\Delta E_{1/2}$[a]
Fc$_2$PDI	564	--	--
(Fc$_2$PDI)CoCl$_2$	617	820	203
(Fc$_2$PDI)FeCl$_2$	584	867	264
(Fc$_2$PDI)MgCl$_2$	641	835	194
(Fc$_2$PDI)ZnCl$_2$	616	810	194

From the UV-vis data shown in **Figure 2.3**, the first observation of note is the substantial increase in ferrocenyl transition intensity in **Fc$_2$PDI**. For simple ferrocene derivatives, the absorptivity of this symmetry-forbidden transition is ~100-200 $M^{-1}cm^{-1}$.[94, 96] The ferrocenyl band in $FcNH_2$ shows an absorptivity of $\epsilon \approx 200$, which increases to $\epsilon \approx 2800$ $M^{-1}cm^{-1}$, or 1400 per Fc center, for **Fc$_2$PDI**. This absorptivity range is consistent with a symmetry allowed transition, but likely not a full charge transfer which would typically have ϵ > 5,000-10,000 $M^{-1}cm^{-1}$.[96] Interestingly, the absorptivity of the band does not change significantly upon metallation, except for the **(Fc$_2$PDI)ZnCl$_2$** complex which shows a greater absorptivity (≈4000 $M^{-1}cm^{-1}$). The energy of this ferrocenyl band changes between ligand formation and metallation, however. While the $FcNH_2$ ferrocenyl band is centered at 442 nm—typical for a Fc derivative, **Fc$_2$PDI** exhibits a 35 nm redshift to 478 nm. The **(Fc$_2$PDI)MCl$_2$** complexes further redshift ~125 nm to ~600 nm. The Zn and Mg complexes display the ferrocenyl band at slightly higher energy (ca. 10 nm) than the Fe and Co complexes (**Figure 2.3**). It is interesting that all four **(Fc$_2$PDI)MCl$_2$** (Co, Fe, Mg, Zn)

metal complexes have similar absorption in the range of 600 nm which is not strongly affected by the metal. This suggests that the orbitals responsible for this transition are not localized on the central metal center and are probably mainly ligand centered orbitals. Note also the changes in bandwidth from Fc, to **Fc$_2$PDI**, to the **(Fc$_2$PDI)MCl$_2$** compounds which is another indication of delocalization in the donor/acceptor orbitals. To more concretely analyze these changes, the experimental spectra were fit to gaussians using the known electronic structure of ferrocene. The ferrocenyl band[94] (442 nm in $FcNH_2$) is known to contain two transitions—which can be successfully fit to two Gaussian peaks (**Figure A.9-A.14; Table 2.4**). The full width at half-maximum (FWHM) of each ferrocenyl transition increases from 70-80 nm for $FcNH_2$ to 100-102 nm for **Fc$_2$PDI**, and to ~160-175 nm for the **(Fc$_2$PDI)MCl$_2$** complexes (**Table 2.3**).

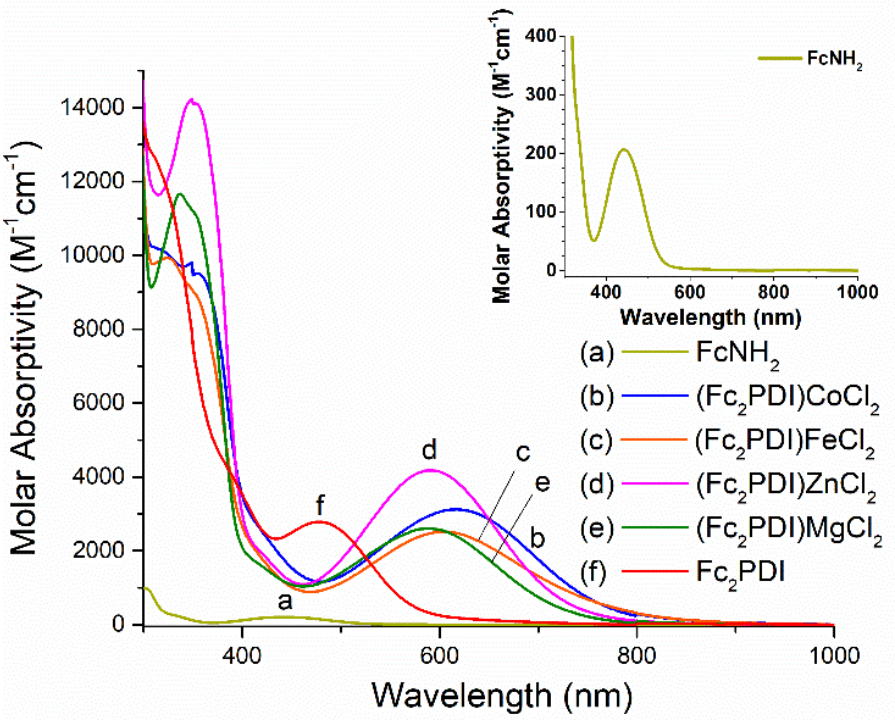

Figure 2.3. UV-vis spectra of **FcNH$_2$**, **Fc$_2$PDI**, and **(Fc$_2$PDI)MCl$_2$** (M = Co, Fe, Zn, Mg) in dry, degassed DCM. Inset: enlarged spectrum of $FcNH_2$.

Table 2.4. Summary of experimental UV-vis band parameters and fitting of the ferrocenyl band in **Figure 2.3** to two Gaussians. FWHM: full-width-at-half-maximum.

Molecule	**UV-vis Bands**		**Gaussian Fitting**		
	λ	Absorptivity	λ	Absorptivity	FWHM
$FcNH_2$	442	207	468	131	79
			422	142	70
Fc_2PDI	478	2782	458	1791	102
			504	1406	100
$(Fc_2PDI)CoCl_2$	616	3120	577	1950	174
			651	1650	150
$(Fc_2PDI)FeCl_2$	605	2517	576	1660	160
			648	1210	160
$(Fc_2PDI)MgCl_2$	590	2601	552	1320	170
			660	1520	148
$(Fc_2PDI)ZnCl_2$	590	4179	568	2200	160
			612	2200	146

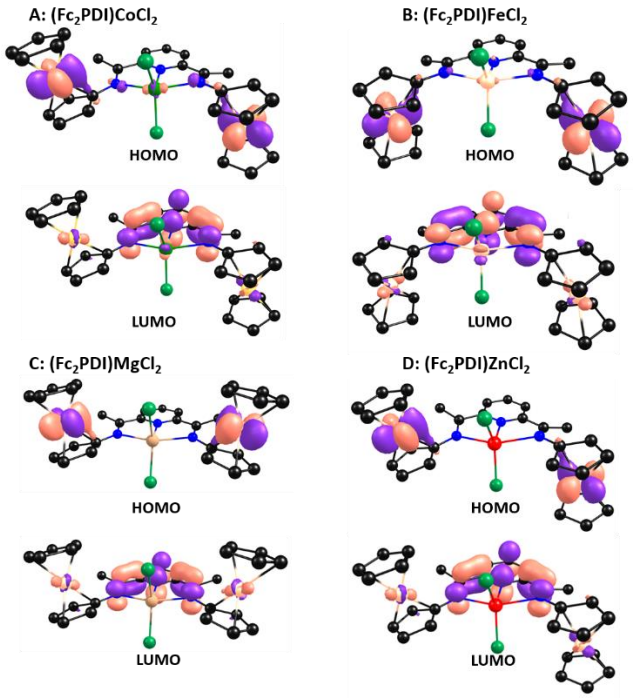

Figure 2.4. DFT-computed frontier molecular orbitals of the indicated $(Fc_2PDI)MCl_2$ complexes (M = Co, Fe, Zn, Mg).

To probe the optical spectroscopic assignments further, DFT and time-dependent DFT calculations were carried out. Geometry optimizations for the structures of **$(Fc_2PDI)MCl_2$** (Co, Fe, Mg, Zn) were carried out at the B3LYP/6-31+G(d,p) level of theory and are in excellent agreement with the X-ray structures geometries. B3LYP was applied here based on its success in analogous mixed-valent complexes,[42, 97] and the excellent agreement with our experimental and computed geometries as well as our experimental and computed UV/visible spectra. According to the DFT calculations, all four complexes have nearly identical frontier molecular orbitals (**Figure 2.4**) in which the HOMO is localized in the d-orbitals of the two ferrocene substituents (d_{xy}/d_{x2-y2}) with minor contribution from nitrogen and central metal orbitals. The LUMO, in contrast, is mainly delocalized over the pyridine and imine groups with some contribution from the ferrocene d_{xz}/d_{yz}

orbitals. In other studies, small levels of delocalization have been seen even in cases of direct metal-metal interaction from donation of ferrocene into high valent metals.[50] In addition, the calculated UV-vis spectra are in good agreement with the experimental values; for more details see the SI. The observed absorption of these complexes in the range of 600 nm is attributed, according to the calculations, to the HOMO → LUMO transition. Thus, the DFT calculations support the empirical findings for orbital combinations and bonding.

Spectroelectrochemistry: To reinforce assignments from the UV-Vis experiments and DFT, spectroelectrochemistry measurements were employed.[98] This technique was performed by measuring the UV-vis spectrum of aliquots taken during bulk electrolysis, and thus detecting electronic structure changes resulting from oxidation.[98] Spectroelectrochemistry was performed in a quartz Schlenk cuvette with 100 mM TBA-$BArF_{24}$ electrolyte, using carbon foam working and Pt counter electrodes, with an Ag wire pseudo reference. The sharp spectroscopic features near 2000 nm are due to quartz absorptions and solvent vibrational overtones, as demonstrated by solvent blanks (see **Figure A.15**). Upon oxidation, **Fc_2PDI** changes from red to blue/green via a 2 e^- event—at constant voltage, two equiv. of charge are transferred. This correlates with a decrease in the 478 nm ferrocenyl band (**Figure 2.5A**), reflecting removal of the electron in the Fc-based donor orbital in this transition. The growth of a broad band at low energy centered around 776 nm (**Figure 2.5A)** is also observed, which contrasts with the free Fc^+ LMCT band, which is comparatively narrow and centered at 625 nm.[94]

Given that **(Fc_2PDI)$FeCl_2$** displays the largest ΔE in the CV experiments, we decided to explore the spectroelectrochemical properties of this compound. Immediately evident is that the complex becomes black upon oxidation in a 1 e^- event. There is a slight decrease in its corresponding ferrocenyl band (at 605 nm) as well as substantial broadening. A new band system

at ~850nm appears, presumably of ferrocenium LMCT character. Interestingly, a very broad transition appears in the NIR that best assigns to a metal-metal charge transfer (MMCT) between the ferrocene and ferrocenium groups. This assignment is confirmed by further oxidation by 1 e- to the **$[(Fc_2PDI)FeCl_2]^{2+}$** state, forming a yellow/green solution lacking MMCT features.

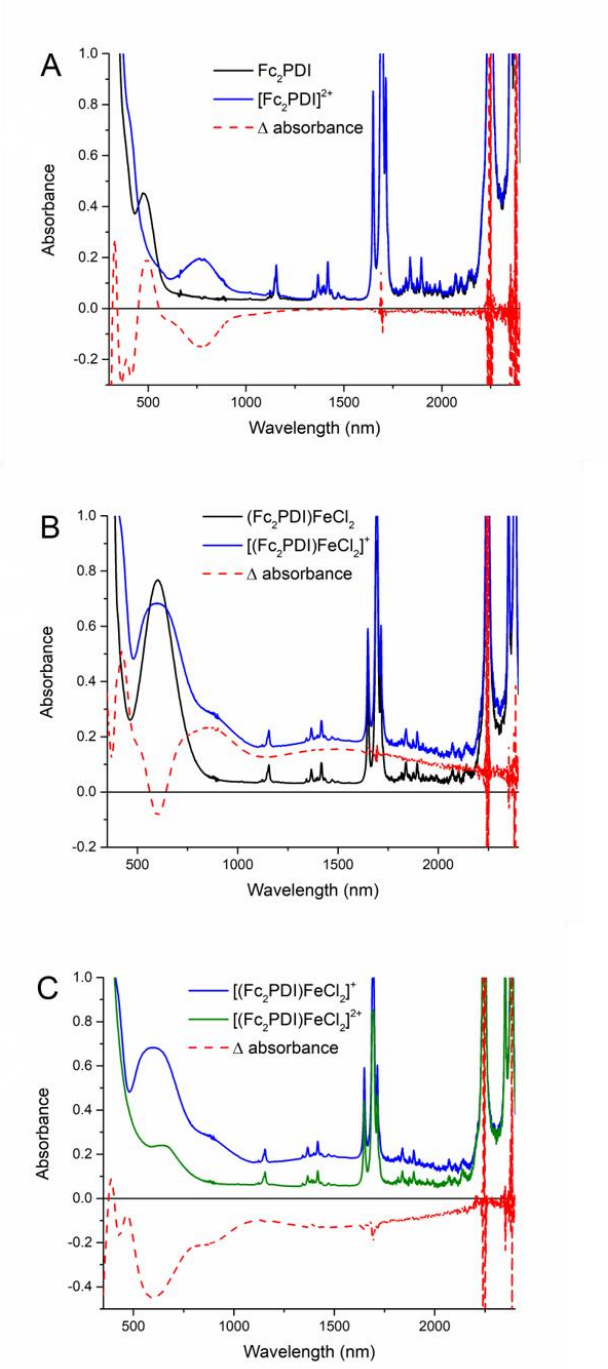

Figure 2.5. UV-vis-NIR spectra of **A**. **Fc_2PDI** (black) **$[Fc_2PDI]^{2+}$** (blue) and change upon oxidation (red dashed); **B**. **$(Fc_2PDI)FeCl_2$** (black), **$[(Fc_2PDI)FeCl_2]^{+}$** (blue) and **C.** **$[(Fc_2PDI)FeCl_2]^{+}$** (blue), **$[(Fc_2PDI)FeCl_2]^{2+}$** (green) and change upon oxidation (red dashed). under spectroelectrochemical conditions.

2.3 Investigation of Electronic Structure

Metallation-induced Electronic Coupling. After metallation, electronic coupling between the ferrocenes is observed, as evidenced by the oxidation of one ferrocene perturbing the oxidation potential of the second via cyclic voltammetry. While there does seem to be an increase in rigidity of the ligand scaffold upon metallation, rigidity does not explain the lack of coupling in low valent main group Fc_2PDI complexes reported by the Ragogna group.[72] Furthermore we observe increased redox stability, demonstrated through highly reversible oxidation events. In marked contrast, the main group analogs reported previously yielded CV data suggestive of decomposition during redox events. These combined observations lead us to conclude that the electronic manifold is different in the transition metal series versus the main group series. This conclusion is further supported by the small ΔE in the more metallic Sn compound, which is absent in the P, Se, S, Te, and Ge complexes, indicating that transition metal chemistry of this ligand is fundamentally different from the nonmetallic main group analogues. If different conformers gave rise to different electrochemistry, we would expect an admixture of signals or an ECE mechanism in the rapid exchanging free ligand—which is not observed. It seems that more acidic heteroatoms in the binding pocket are necessary for this coupling to occur, suggesting that the effect is not due to conformational changes. Conformation changes would explain the data if interaction between the ferrocenes was predominantly electrostatic (e.g., changes in inter-ferrocene distance altering the electrostatic interaction between them). Rather, it appears that the coupling is driven by coordination of **Fc_2PDI** to a transition metal. Observation of d-element-driven coupling is not unprecedented, as dithiolato ligands undergo "π-reorganization" upon coordination to transition

metals. This reorganization modifies the electronic structure of the dithiolate ligand to promote Proton Coupled Electron Transfer (PCET) chemistry.[99, 100]

Furthermore, the reported lack of coupling in low-valent main group **Fc_2PDI** complexes provides a clue to the mechanism of coupling. Less acidic P(I), Te(II), Se(II), and S(II) centers do not promote interaction between ferrocenes, while more acidic M(II) ions are likely to stabilize the electron-rich Fc_2PDI ligand system, enhancing the energy match between metal and organic π^* orbitals. Lowering the energy of the LUMO would better facilitate a 3-state mechanism for electron transfer, resulting in coupling between metals. This argument is supported by The present crystallographic, CV, UV-vis, and spectroelectrochemistry data. Depiction of the proposed coupling process and the molecular orbital level is then given in **Figure 2.6** and explained below.

XRD. Though one expects that a coplanar conformation would induce optimal coupling, ferrocenyl groups exhibiting substantial torsions in the solid state can still engage in electronic coupling in solution.[23, 25, 68, 86] This suggests that as long as coplanar geometries are readily sampled at room temperature then coupling remains intact, even if it is not the sole conformation. We also conclude that changes in conformation ("open" vs. "closed") have little bearing on the occupied bonding orbitals, as the ligand bond distances do not significantly vary in any of the compounds studied. This suggests that conformational changes do not appreciably alter the bonding characteristics, which is to be expected based on symmetry—similar orbital overlaps in both conformations. No change in bond lengths suggests that for the neutral species, spectral changes originate largely from orbital interactions occurring in the unoccupied manifold of the MO diagram, which cannot be probed by XRD. This is also evidenced by a more extreme reduction potential for **Fc_2PDI** compared to the **$(Fc_2PDI)MCl_2$** complexes, suggesting a stabilization of the π^* system upon metallation ($E_{red} \sim$ -1.5 V for **Fc_2PDI**, $E_{red} \sim$ -0.9 to -1.2 V for **$(Fc_2PDI)MCl_2$**).

Interestingly, the conformation of the oxidized ferrocene changes, canting inwards towards the chloride ligands. The distance between chloride and ferrocenyl iron is ca. 4.2 Å, suggesting an electrostatic attraction rather than formal coordination. This has the added effect of decreasing the intermetallic distance, which leads to uncertainty in extracting an electronic coupling constant using Hush theory, which employs the internuclear distance as a parameter. This distortion also shines light on a complication infrequently discussed in mixed valent studies--that changes in charge distribution upon oxidation can promote rearrangements that may explain why some highly conjugated and promising scaffolds fail to engender strong coupling. In **(Fc$_2$PDI)FeCl$_2$,** this distortion brings the formally Fe(III) center closer to the chlorides in the MCl_2 fragment and likely stabilizes a localized Fe(III) center. Thus, the structure change likely limits the ultimate amount of charge delocalization. This would be akin to ion pair effects known to have strong impacts on degree of delocalization, as probed as a function of supporting electrolyte in CV experiments.[22] Because electronic coupling is weak in this system (*vide infra*) and it is not clear how exchange of chlorides would affect the geometry since steric and electronic factors of individual ligands may lead to different conformers. We focus here on suggesting how this conformer suggests interesting prospects for reactivity as opposed to how to optimize towards increased delocalization. This structure change, bringing the cationic Fe(III) into the secondary coordination sphere of the MCl_2 fragment suggests that substrates bound to the central M(II) center can interact—covalently or electrostatically—with the Fe(III) in a cooperative way. Ferrocenium is a useful mild oxidant that given the close distance to ligands on the central metal may undergo facile oxidation of reaction intermediates. Furthermore, a cationic Fe(III) can generate local electric field gradients and polarize substrates, the LMCT states have been shown to be useful in photocatalysis,[101, 102] and it is known to act as a Lewis acid catalyst.[103] Addition of Lewis Acids in the secondary coordination

sphere is an attractive strategy in bond activation.[104] Furthermore, the acceptor orbital in charge transfer transitions for the neutral complexes (see theory section) features a similar ligand centered LUMO that is one of the occupied frontier orbitals in highly reduced PDI structures.[85] Suggesting that an internal electron donor could function as a photoreductant in lieu of aggressive reductants such as $NaEt_3BH$ or Na(Hg). Electronic coupling in excited states is an area of continued interest and exploration[105] and the easily accessible charge transfer in this system yields only a partial hole (see theory section) at ferrocene, which may reveal interesting properties

Spectroelectrochemistry: In accord with the CV experiments, free **Fc_2PDI** is not stable in its mixed valent state and cannot be observed by spectroelectrochemistry—constant potential electrolysis continues until $2e^-$ are removed from the molecule. If electrolysis is halted after $1e^-$ is removed, all species coexist in equilibrium due to disproportionation. **(Fc_2PDI)$FeCl_2$** is stable in its mixed valent form. Pausing electrolysis after oxidation by one electron reveals a broad low energy feature assignable as an IVCT. Fitting IVCT bands and application of Marcus-Hush theory allows for the electronic coupling of two metal sites to be extracted based on the electron transfer properties.

$$H_{ab} = \frac{2.06 \times 10^{-2} (\nu_{max} \varepsilon_{max} \Delta\nu_{\frac{1}{2}})^{1/2}}{r_{ab}}$$

Where H_{ab} is the electronic coupling constant, while ν_{max} ε_{max}, $\Delta\nu_{1/2}$, and r_{ab} are the energy of the IVCT band, the extinction coefficient, band FWHM, and distance between metal sites a and b, respectively. Application of this theory gives an electronic coupling of 348 cm^{-1}, taking r_{ab} to be the crystallographically determined distance between ferrocenes in the neutral (all Fe(II)) structure (8.1 Å) and ϵ calculated as an upper bound based on the initial electrolysis concentrations (e.g. ignoring solvent evaporation). This is a modest degree of electronic coupling, indicating Class II behavior, but represents a rare example of a bis-ferrocenyl complex acting as a ligand to another

metal fragment that is in a known catalytically active structure (e.g. PDI catalysts). While CV strongly suggests IVCT occurs between ferrocenes (as the second ferrocene is the most easily oxidizable group) on closer inspection, it is interesting that ET occurs between the more disparate metals. This could be explained by a 3-state electron transfer mechanism[24] through mutual coupling of each Fc to the ligand π system, providing a mode for electronic coupling--through unoccupied orbitals using a superexchange mediated electron transfer mechanism.[106] This would also explain the lack of decreased intensity for the ferrocenyl band, as 3 state coupling results in an increase in the intensity and broadening of absorption features on the unoxidized metal. It appears possible to modify the ancillary chloride ligands (e.g., with larger ligands such as bromide) to allow better energy matching so that the MX_2 fragment participates in the HOMO or LUMO to involve it inside the superexchange mechanism and engender coupling through all three metals. Under this understanding, the

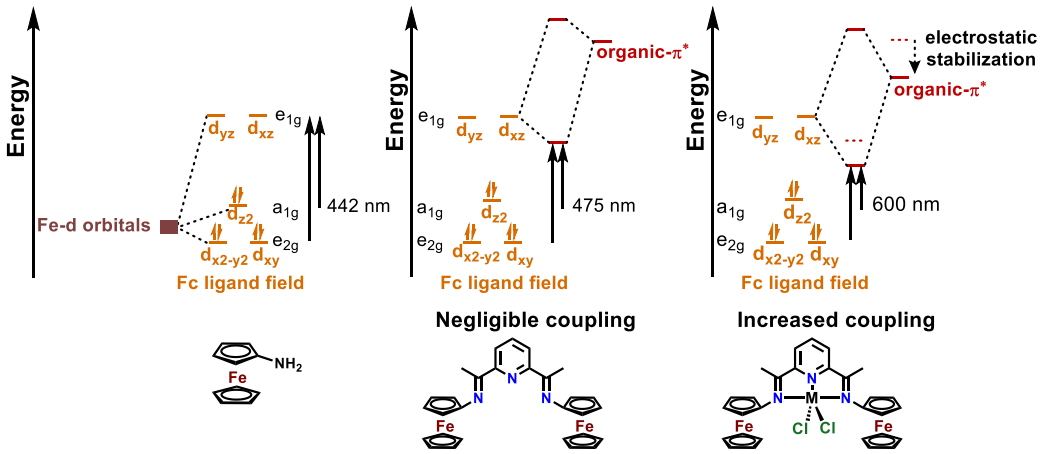

Figure 2.6. Qualitative MO diagram for proposed electronic interactions between the ferrocene and organic π system. D_{5d} ligand field symmetry labels are used for the ferrocene fragmentcalculated H_{ab} is better considered an effective coupling constant, since a two state model is applied. This approximation is invalid in the case of strong coupling,[107] which does not appear present.

UV/Vis/DFT. The orbital interactions can be further understood on the basis of the intensities, energies, and line shapes of the ferrocenyl transitions. Since transitions occur from occupied to unoccupied orbitals, we can infer characteristics of the higher energy orbitals unobservable by x-ray diffraction. In observing a large increase in absorptivity for the ferrocenyl band in the **Fc_2PDI** ligand relative to ferrocene, it is logical to conclude that the symmetry forbidden transition has become symmetry-allowed. Similar results are seen in Fc-Ru and Fc-Pd/Pt compounds where mixing of Fc orbitals with other ligand or metal orbitals breaks inversion symmetry and leads to absorptivity increases.[49, 54, 102] We infer that mixing of Fc and imine orbitals can explain a breaking of symmetry, but cannot posit *a priori* if the organic character is in the HOMO or LUMO. Given that the HOMO energy of the present ferrocenes is not significantly perturbed (see

electrochemistry section), and bond distances do not change substantially (see crystallography), the mixing likely involves the Fc LUMO, Fe centered d_{xz}/d_{yz} orbitals. Inspection of the DFT results (Figure 4) supports this assertion, as the HOMO is largely Fc d_{xy}/d_{x2-y2} while the LUMO displays d_{xz}/d_{yz} character on the ferrocene units and a large amount of organic PDI character.

To further understand the DFT results, which suggests mixing of Fc d_{xz}/d_{yz} orbitals with the imine π* instead of π, we consider the effects of each interaction. Donation from the imine π into the unoccupied d_{xz}/d_{yz} orbitals would result in a bonding/antibonding interaction, raising LUMO levels, changing imine bond strengths, and placing more electron density in the ferrocene system. Instead, the electrochemistry supports a largely unperturbed ferrocene HOMO, and the spectroscopy supports a stabilized ligand LUMO (red-shifted absorption). Rather, mixing between the Fc unoccupied d_{xz}/d_{yz} and imine π* orbitals such that the excited state assumes ligand character and becomes more delocalized (Figure 6) is consistent with the experimental data and DFT results. Similar observations and conclusions that binding of PDI macrocycles to Lewis Acids stabilizes the PDI π* orbitals and leads to better energy matching between metal and organic orbitals, causing greater delocalization.[108] We can thus describe a metal to mixed metal-ligand charge transfer ("MMMLCT") in analogy with mixed metal-ligand to ligand CT ("MMLLCT") excitations.[99, 109, 110] As shown in Figure 6, this assignment explains the present observations of an unperturbed HOMO and a red-shifted HOMO-LUMO transition.

The red-shift of the ferrocenyl band in **Fc_2PDI** is relatively small, suggesting the degree of mixing between metal and organic orbitals is too small to produce coupling that can be observed by CV. Nevertheless, the increase in intensity allows us to confidently assign a break in symmetry and demonstrate orbital interaction. Fitting the spectrum to Gaussians reveals two transitions within the 478 nm band, which accounts for both d-d transitions seen in the similar region of free

Fc. Furthermore, a weak tail is also observed, which is intuitively assigned to the spin-forbidden counterpart transition, as observed in ferrocene.[94] Partial allowedness (symmetry-allowed, spin forbidden) causes the intensity to increase from 7 $M^{-1}cm^{-1}$ (seen in ferrocene), to ~50-100 $M^{-1}cm^{-1}$.We are unable to model the pure Fc d-d transitions at 442 nm, meaning we are only able to account for all the ligand field transitions by assigning this as a metal to mixed metal/ligand CT rather than a new MLCT to the PDI backbone in addition to the original Fc d-d transitions. This is also in accord with this transition being weaker than expected for a full MLCT (ϵ = 1,400 per metal center, rather than ϵ > 5,000-10,000). This band must be a shift of the Fc d-d transition rather than a new MLCT in addition to the normal Fc transitions. It is uncommon to observe shifts larger than ca. 10-15 nm in simple ferrocenyl compounds, consistent with the donor and acceptor orbitals in ferrocene being metal-centered and insensitive to ligand perturbation.[93] In **Fc_2PDI**, a change in the ligand field appears to take place since it exhibits a much larger shift (36 nm). This is reminiscent of observations by Diaconescu and coworkers, where arylamino substituted ferrocenes show more ligand character in the LUMO, whereas the HOMO is generally still metal-centered, lowering the HOMO-LUMO gap.[93]

To find support for the present assignments in the literature, UV/vis spectra of several mixed-valent Fc compounds were also considered. However, since Fc mixed-valent studies typically focus on the NIR region and the related MMCT transitions arising from electronic coupling, it is challenging to directly compare the present results to known Class II and Class III mixed valent compounds. Note however that some Fc conjugated systems have absorbances in the 500-600 nm range, however it is unclear if these represent Fc mixing, MLCT, or π/π^* transitions.[31, 111] As a further complication, in cases where low energy CT bands are observed, they do not

correlate in a consistent way with the degree of coupling. Thus, cases with coupling and no spectral shifts are observed, [87, 112] as are cases with spectral shifts and no coupling.[113]

Central metal not directly engaging in coupling pathway.

The imine bond lengths do not change significantly upon metallation, suggesting that π bonding between the organic π* system and MCl_2 d_π orbitals is insignificant—as seen in other neutral first row PDI complexes.[16, 114] The DFT analysis further supports this picture as negligible π-bonding is observed in the frontier orbitals. Elongation of the imine bond is frequently used to estimate the degree of electron density residing in PDI π/π* networks.[16] The unchanged imine bond distances argue that only small amounts of electron density are transferred from the MCl_2 fragment onto the ligand or from the ligand π system into the MCl_2 fragment. For this reason, the Fc delocalization onto the MCl_2 fragment cannot be directly implicated. Small contributions from the MCl_2 fragment are seen in the DFT orbitals, and small spectral/electrochemical changes are seen, suggesting it is a non-negligible but weak locus of bonding. Thus, the MCl_2 fragment can be thought of as triggering coupling although it does not participate substantially in the delocalization pathway. Since π-bonding does not seem to be important, it is proposed that an electrostatic interaction triggers coupling. Similar interactions are proposed in ferrocenyl polypyridyl complexes, where coordination to Lewis acids creates intense charge transfer transitions from ferrocene and is useful for ion sensing.[66, 115] Moreover, the present observation of similar electronic properties across a series of metals with diverse coordination chemistries is highly unexpected since mixed-valent compounds typically exhibit high physicochemical sensitivities to substitution and modification. This affords a unique reactivity possibility that the coupling triggered by metal ion binding will be seen with a variety of ions, increasing the versatility of this ligand system. Insensitivity of the interaction towards metal identity in the Fc_2PDI system is further rationalized

on similar ionic radii and identical charge numbers, leading to similar electrostatic stabilizations. This suggests that fine tuning of the coupling interaction is possible by substituting metal ions with different charge densities. Note however that the larger $\Delta E_{1/2}$ for **(Fc$_2$PDI)FeCl$_2$** vs the other complexes suggests there are further effects to be studied, and that our optical, electrochemical, and crystallographic characterizations do not uniquely define these effects.

2.4 CONCLUSIONS

Structural, electrochemical, spectroscopic, and computational evidence argues that metal binding to **Fc$_2$PDI** triggers mixing of **(Fc$_2$PDI)MCl$_2$** (M=Fe, Co, Mg, Zn) ferrocenyl Fc d-orbitals with the PDI π* network, engendering coupling between the two Fc sites. Curiously, this coupling appears dependent on metal ion binding but does not disappear when different s- or d-block metals are employed—demonstrating the coupling is generalizable and worth exploring further. This is an interesting contrast to p-block analogues which do not exhibit coupling in most cases. CV displays a ~200 mV separation between oxidation of each ferrocene for the Fe, Co, Zn, and Mg complexes, but no separation is seen in the free ligand. Minimal π interaction between the ligand and MCl_2 fragment is evident in the crystal and DFT computed structures, which show no variation in back-bonding into imine π* orbitals between the free ligand and the complexes. UV-vis spectroscopy shows mixing of Fc d orbitals with ligand π orbitals, with the extent of mixing dependent on metal binding but not appreciably on metal identity. Upon oxidation, broad and low energy ferrocenium transitions appear—indicative of highly delocalized mixed metal-ligand orbitals. Importantly we also observe a very broad IVCT in the NIR, which clearly indicates coupling between the ferrocenes. We assign this as a Class II compound based on the weak (<5000 $M^{-1}cm^{-1}$) and broad (>2000 cm^{-1}) IVCT feature. We propose that when Fc_2PDI binds to a Lewis acidic MCl_2 fragment, coupling is promoted by a better energy match between Fc and organic π

orbitals. Crystallography suggests that in the mixed valent state the ferrocenium pivots into the MCl_2 coordination sphere, potentially opening doors for cooperative catalysis. Interestingly, this system displays orbital mixing between PDI and Fc orbitals, but most delocalization is seen in unoccupied orbitals. We propose that 2nd and 3rd row transition metals that are known to engage in stronger back bonding into PDI ligands[116, 117] may place electron density in the orbitals engaged in the delocalized orbitals, leading to stronger coupling and possibly new coordination chemistry.

2.5 EXPERIMENTAL SECTION

General Considerations. All procedures for air- and moisture-sensitive compounds were carried out with rigorous exclusion of O_2 and moisture in flame or oven-dried Schlenk-type glassware interfaced to a dual-manifold Schlenk line or Ar fed high-vacuum (10^{-6} – 10^{-7} Torr) line using an oil diffusion pump, or in an Ar-filled MBraun glovebox with a high capacity recirculator (<0.5 ppm O_2). Argon for high-vacuum lines (Airgas, UHP grade) was purified by passage through MnO/vermiculite and Davison 4Å molecular sieve columns. All solvents were degassed by freeze-pump-thaw techniques, excepting tetrahydrofuran (THF) and diethyl ether (Et_2O) which were freshly distilled from sodium using benzophenone indicator (persistent purple). All solvents were stored under inert atmosphere in a Teflon-sealed solvent flask for syringe or vacuum transfer. Dichloromethane (DCM) was distilled off CaH_2. Methanol and ethanol were dried over 3Å molecular sieves and filtered through a cannula (oven dried with a glass fiber filter). NMR solvents were purchased from Cambridge Isotope Laboratories (>99 atom % D). CD_2Cl_2 used for NMR characterization of complexes was distilled off CaH_2, degassed by freeze-pump-thaw method, and vacuum transferred as needed into Teflon valve-sealed NMR tubes (dried in an oven overnight). Iodoferrocene[73] and aminoferrocene[74] were synthesized according to literature procedures. Electrodes were purchased from Bioanalytical Services in West Lafayette, IN.

Physical and Analytical Measurements. Solution ^{1}H and ^{13}C NMR spectra were recorded on a 500 MHz Bruker Avance III HD system equipped with a TXO Prodigy probe. Chemical shifts for ^{1}H and ^{13}C spectra were referenced using internal solvent resonances and are reported relative to tetramethylsilane (TMS). UV-vis measurements were taken on a Perkin Elmer LAMBDA 1050 double beam spectrophotometer, using a 1cm quartz cuvette in dry-degassed DCM. Fitting of the UV-vis spectra was done using Fityk software[118] using pure Gaussian peaks. Elemental analyses were performed in an air free glovebox by Midwest Microlab, Indianapolis, Indiana for % C, N, H. Crystallographically observed DCM solvates were included in % C, H, N determination.

Computational Methods. All quantum chemical calculations were performed using the Gaussian 09.D01 software.[119] Geometry optimizations of all complexes were carried out at the B3LYP[120, 121]/6-31+G(d,p) level of theory. Frequency calculations at the same level were performed to validate each structure as a minimum. The UV-visible spectra of all complexes were calculated using TD-DFT theory at the B3LYP/6-311++G(d,p) level of theory. The dichloromethane solvent effect was calculated by the Polarizable Continuum Model (PCM).[122]

Crystallography. Single crystals were mounted in Paratone® oil and transferred to a cold nitrogen gas stream of a Bruker Kappa APEX CCD area detector equipped with a MoKα microsource. The crystal was maintained at 100.0 K during data collection. The structures were solved using Olex2[123] with the XT structure solution program[124] and refined using the ShelXL refinement package with full-matrix least-square procedures.

Electrochemistry. Electrochemistry was performed in dry-degassed DCM. The electrolyte, tetrabutylammonium tetrakis[3,5-bis(trifluoromethyl)phenyl]borate[89] (TBA-BArF) was prepared according to literature procedures.[125] CV was performed in the dark under a dynamic blanket of N_2 (100mM TBA-BArF, 1mM analyte) using Pt working and counter electrodes, and an Ag wire

pseudo-reference with a Cp^*_2Fe internal standard[95] of known concentration. The working electrode was polished with alumina paste, while the counter electrode was flame polished and the silver wire was polished with fine sandpaper.

Spectroelectrochemistry. Spectroelectrochemistry was performed on a CH Instruments Electrochemical Workstation through bulk electrolysis in a glovebox using a carbon foam working electrode, Pt wire counter electrode, and Ag pseudoreference (prepared as described above). Aliquots were taken and transferred to a dried 0.2 cm quartz cuvette sealed with a Teflon valve. Spectra were taken on a Shimadzu UV-36000 plus UV-vis-NIR spectrometer (300 - 3000nm). The difference spectra were generated by subtraction of the scan featuring the previous electrochemical species (e.g. neutral/monocation, monocation/dication). Due to solvent evaporation over long electrolysis times, these plots are presented in un-normalized absorbance units. Potential was incremented by 50 mV steps until potentiometry indicated oxidation was sustained at the working electrode and maintained until current became negligible.

Syntheses.

Fc_2PDI. *para*-toluenesulfonic acid (~2 mg, ~0.01 mmol), 2,6-diacetal pyridine (154 mg, 0.94 mmol), and 399 mg of $FcNH_2$ (1.98 mmol) were added to a dry Schlenk flask under inert atmosphere. A dry reflux condenser was attached, and the atmosphere was replaced with N_2. Then, 10 mL of dry and degassed ethanol was added by syringe and the reaction was allowed to reflux for 18 h, over which time the solution turned dark red and crystalline material precipitated from solution. The reaction mixture was cooled to 0 °C, concentrated in vacuo, and filtered by cannula. The red crystalline product was washed with cold ethanol and dried. Isolated yield: 292 mg, 58%. Further product can be recovered from the filtrate by recrystallization from DCM/pentane. ^{1}H NMR (CD_2Cl_2, 500 MHz): 8.27 (d, J = 7.8 Hz, 2H, Py-3), 7.81 (t, J = 7.8 Hz, 1H, Py-4), 4.46 (t,

J = 1.9 Hz, 4H, Cp-2), 4.26 (t, *J* = 1.9 Hz, 4H, Cp-3), 4.21 (s, 10H), 2.56 (s, 6H, C*H*$_3$). ^{13}C (CD_2Cl_2, 126 MHz): 166.15(C=N), 157.08 (Py-2), 136.95 (Py-*4*), 121.66 (Py-*3*), 103.98 (Cp-1), 69.93 (Cp), 67.29 (Cp-2), 66.16 (Cp-3), 16.82 (CH_3). Anal. Calcd for **Fc$_2$PDI**, formula $C_{29}H_{27}N_3Fe_2$: C, 65.81; H, 5.14; N, 7.94. Found: C, 65.66; H, 4.99; N, 7.87.

(Fc$_2$PDI)CoCl$_2$. **Fc$_2$PDI** (50 mg, 0.094 mmol) and 12 mg (0.094 mmol) of anhydrous $CoCl_2$ were added to a flame-dried Schlenk flask in a glovebox. Then, 10 mL of DCM was added via syringe and the reaction was allowed to stir at room temperature for 24 h as it turned from red to blue. Over this time blue crystals fell from solution. The solution was diluted with DCM to dissolve all the blue solids and filtered by cannula. The filtrate was subsequently concentrated and diluted with diethyl ether to precipitate the product. The product **(Fc$_2$PDI)CoCl$_2$** was washed with diethyl ether under inert atmosphere until the filtrate was clear, and recrystallized by DCM/diethyl ether layer at -40 °C. Isolated yield: 42 mg of blue crystals 68%. Anal. Calcd for **(Fc$_2$PDI)CoCl$_2$**•DCM (1 crystallographic DCM per unit cell), formula $C_{30}H_{29}N_3Fe_2CoCl_4$: C, 45.43; H, 3.74; N, 5.08. Found: C, 44.92; H, 3.77; N, 5.07.

(Fc$_2$PDI)FeCl$_2$. Fc$_2$PDI (100 mg, 0.0198 mmol) and 24 mg (0.0198 mmol) of anhydrous $FeCl_2$ were added to a dried Schlenk flask under inert atmosphere. 5 mL of freshly distilled THF was added by syringe and the reaction was allowed to stir at room temperature for 24 h. The solvent was removed under vacuum and the crude mixture was taken up in minimal DCM and filtered by cannula. Twice the volume in freshly distilled Et_2O was layered on-top and the mixture was allowed to crystallize at -40 °C. The resulting blue crystals were collected by cannula filtration and dried under high vacuum overnight to give **(Fc$_2$PDI)FeCl$_2$**. Isolated yield: 50 mg of blue-crystals (40%). Anal. Calcd for **(Fc$_2$PDI)FeCl$_2$**, formula $C_{29}H_{27}N_3Fe_3N_3Cl_2$: C, 52.73; H, 4.14; N, 6.16. Found: C, 53.10; H, 4.15; N, 6.41.

(Fc$_2$PDI)ZnCl$_2$. **Fc$_2$PDI** (400 mg, 0.76 mmol) and 100 mg of $ZnCl_2$ (0.73 mmol) were added to a dried Schlenk flask under inert atmosphere, and 5 mL of DCM was added. The reaction was allowed to stir overnight at room temperature. The resulting blue solution was filtered by cannula and the microcrystalline product was washed with ether to give **(Fc$_2$PDI)ZnCl$_2$**, which was recrystallized by DCM/diethyl ether layer at -40 °C. Isolated yield: 260 mg of blue crystals (52%). ^{1}H NMR (CD_2Cl_2, 500MHz): 8.29 (pseudo-dd, *J* = 8.3, 7.6 Hz, 1H, py-*4*), 8.13 (d, *J*=8.0 Hz, 2H, py-*3*), 5.13 (t, *J* = 2.0 Hz, 4H, Cp-2), 4.51 (t, *J* = 2.0 Hz, 4H, Cp-3), 4.29 (s, 10H, Cp), 2.82 (s, 6H, C*H*$_3$). ^{13}C (CD_2Cl_2, 126 MHz): 157.44 (C=N), 151.44 (Py-2), 143.68 (Py-*4*), 124.08 (Py-*3*), 97.15 (Cp-1), 70.82 (Cp), 70.07 (Cp-2), 69.50 (Cp-3), 18.88 (CH_3). Anal. Calcd for **(Fc$_2$PDI)ZnCl$_2$**•DCM (1 crystallographic DCM per unit cell), formula $C_{30}H_{29}N_3Fe_2ZnCl_4$: C, 48.01; H, 3.89; N, 5.60. Found: C, 48.28; H, 3.78; N, 5.82.

(Fc$_2$PDI)MgCl$_2$. **Fc$_2$PDI** (212 mg, 0.4 mmol) and 38 mg (0.4 mmol) of anhydrous $MgCl_2$ were added to a dry Schlenk flask under inert atmosphere. Then, 5 mL of anhydrous DCM and 5 mL of anhydrous MeOH were added by syringe and the solution was allowed to stir for 24 h at room temperature. The solvent was evaporated under vacuum and the blue/purple solids were re-dissolved in DCM, then filtered by cannula. The solution was concentrated under vacuum and the complex was recrystallized overnight by layering with diethyl ether at -40 °C. The highly moisture-sensitive crystals were dried under high vacuum overnight to give **(Fc$_2$PDI)MgCl$_2$**. Isolated yield: 211 mg of blue/purple plate-like crystals (84%). ^{1}H NMR (CD_2Cl_2, 500 MHz): 8.29 (pseudo-dd, *J* = 8.3, 7.7 Hz, 1H, py-*p*), 8.07 (d, *J* = 8.1 Hz, 2H, Py-*m*), 5.11 (t, *J* = 2.0 Hz, 4H, Cp-γ), 4.52 (t, *J* = 2.0 Hz, 4H, Cp-β), 4.30 (s, 10H, Cp), 2.85 (s, 6H, C*H*$_3$). ^{13}C (CD_2Cl_2, 126 MHz): 161.31 (C=N), 153.08 (py-ipso), 143.94 (Py-*p*), 123.99 (Py-*m*), 97.72 (Cp-ipso), 70.82 (Cp), 69.89 (Cp-γ), 69.43

(Cp-β), 19.10 (CH_3). Anal. Calcd for **(Fc_2PDI)$MgCl_2$**•0.5DCM, formula $C_{30.5}H_{28}N_3Fe_2MgCl_3$ C, 53.74; H, 4.72; N, 5.97. Found: C, 53.42; H, 4.55; N, 6.22.

Chapter 3

Influence of Rare Earth Metals' Ionic Radius on Metal-Metal Charge Transfer in Trinuclear Mixed-Valent Complexes

Chapter 3

3.1 INTRODUCTION

When multiple metal ions are connected by a delocalized bridging ligand, the conjugation can allow the d-orbitals on the metal ions to electronically couple to each other. This coupling enables electron transfer between metal centers and delocalization of d-electrons over the bridge. While the properties and physical underpinnings of such electronic coupling between redox-active metal centers in mixed valent systems have been well studied,[24, 26, 107] there are still challenges in understanding structure-property relationships in complex molecules. Generally, mixed-valent systems are studied by permutating a library of conjugated bridging ligands and observing the effects of substitution to infer the variables influencing the metal-to-metal charge transfer (MMCT) that arises from electronic coupling.[25] However, it is often difficult to predict which bridging ligands will lead to strong MMCTs, given that electronic coupling can be very sensitive to variables that are difficult to finely tune and deconvolute, such as bond angles, torsions, energetic separation between orbitals, solvation etc. Furthermore, in solution, thermal motion can result in an ensemble of geometries that can be averaged on the spectroscopic timescale.[25] Because any substitution often changes both molecular and electronic structure, it can be difficult to isolate variables for analysis. One such challenging variable is the effect of extended nuclearity in a mixed valent system. Metallation often has dramatic impacts on both the geometry and electronics of the ligand, with the exact effects depending on the identity of the metal. To this end, it would be desirable to design bridging ligands that are both rigid and can accommodate multiple metal types in a symmetric geometry to decrease the number of free variables when analyzing MMCT properties.

Fortunately, the field of non-innocent ligands has established several families of conjugated ligands that display extensive delocalization between metals and ligands,[4, 7, 9] suggesting them as

good candidates as bridging ligands. Such metal-ligand delocalization can be considered a form of metal-organic mixed valency, harnessing proper orbital overlaps and orbital energies for delocalization across the complex. Using such ligands as a starting point provides well-studied electronic structures and modular syntheses for exploring traditionally challenging to study elements of electronic coupling. For example, studying the effect of increasing nuclearity in an already electronically coupled mixed valent system is a challenging synthetic problem (e.g., installing multiple binding sites that can be metallated in a controlled way) for which there is no obvious general strategy. Additionally, investigations of the direct participation of the bridging ligand in electron transfer mechanisms where the charge transfer is a blend of MLCT (or LMCT) and MMCT require bridging ligands with significant electronic coupling between metal and ligand in addition to coupling between metals, which is afforded by non-innocent ligands. From the non-innocent ligand literature, we know that metal binding and delocalization of frontier orbitals between metal and ligand impart emergent properties to the complex.[10, 18, 85] As such, one reasonably expects that by converting a non-innocent ligand into a mixed valent system by replacing aryl groups with redox-active groups such as ferrocenyls, it should be possible to generate a mixed valent compounds that can bind to an additional metal. In this design, we can modify the geometry and electronics of the bridging organic linker between ferrocenes by permutating the additional third metal.

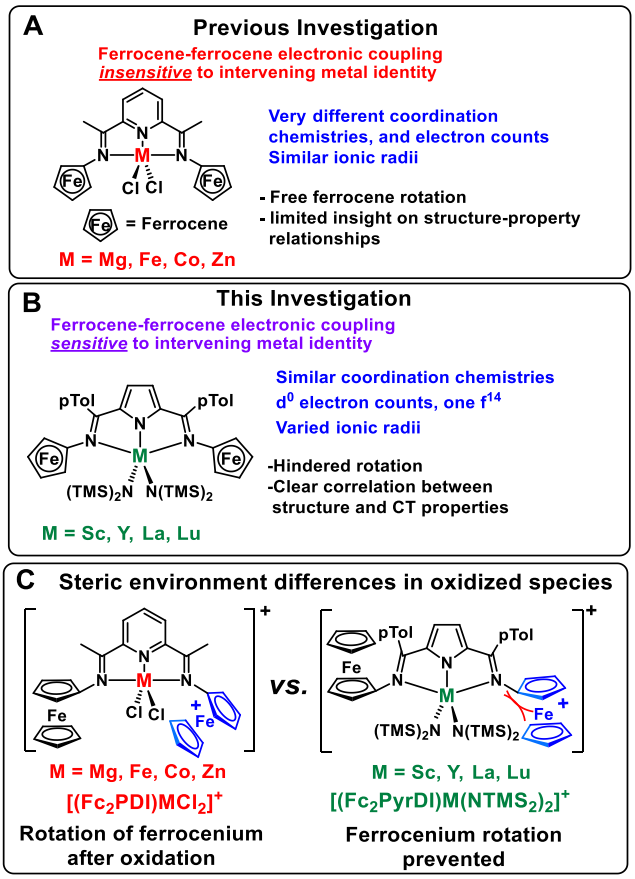

Figure 3.1. Comparison of **A.** TM-pyridine and **B.** RE-pyrrolate complexes and their mixed valent properties. **C.** shows the different steric environments afforded by the RE-pyrrolate complexes

In a recent study, we reported that the addition of a transition metal ion to a bis-ferrocenyl pyridinediimine ligand switched it from a Class 1 to a Class 2 mixed valent system (**Figure 3.1A**).[126] Interestingly, the additional metal ion did not participate directly in the electronic coupling itself, nor did metal ions of different coordination chemistries (Mg, Fe, Co, and Zn) impart significantly different properties. This raised questions about whether structural influences from metalation are relevant to the emergent behavior of electronic coupling even if varying coordination chemistries was not. Metallation of polydentate delocalized ligands has many effects

on the ligand itself, such as electron withdrawal/donation from Lewis Acidic/Basic d-orbitals and rigidification/templating of the ligand around the metal ion. Isolating such variables is vital to understand how the interaction between a bis-ferrocenyl ligand and an extra metal center affects the interaction between ferrocenes. However, when working with transition metal ions, it is challenging to isolate the geometric and electronic effects that the metal has on the surrounding ligands. Transition metal ions have different levels of covalency, preferred coordination geometry, and acidity/basicity that are interdependent and difficult to deconvolute. In contrast, rare earth ions (defined by IUPAC as the lanthanides as well scandium and yttrium)[127] are generally thought to display very similar coordination chemistries,[128] but differ primarily in ion size, and thus charge density. These ionic radius differences[129] (r = 88.5, 100, and 104 pm for Sc, Lu, and Y—respectively) can change the polarization across the ligand due to different charge densities, and alter bond and torsion angles as a result of different sized coordination spheres (**Figure 3.1B**).[130-132] Recognizing this opportunity to isolate the geometric influence of metal ionic radius from intrinsic coordination chemistry, we synthesize and characterize an series of d^0 rare earth complexes coordinated by an anionic bis-ferrocene pyrrolediiminato ligand (**Figure 3.1B and 3.1C**). In doing so, we probe the effects of metal ion size on the electronic structures of the mixed valent state in these complexes and, consequently, it's role in modulating the charge transfer between ferrocene moieties.

3.2 Synthesis and Characterization of Bisferrocenyl Pyrrolate Complexes

Synthesis of Fc_2PyrDIH (1)

While pyridine diimine structures are good ligands for transition metals (**Figure 3.1A**), rare earth ions bind only loosely to neutral nitrogen donors and generally require harder anionic O^- or N^- donors. For this reason, a pyrrole diimine ligand was targeted for this study (**Figure 3.1B**). The

precursor 2,5-diacyl pyrroles are generally challenging to prepare. However, McNeece et al. [133] reported a straightforward adaptation of a benzothioloxium protection and pyrrole oxidation protocol, affording 2,5-ditolylacylpyrrole in good yield on a multigram scale. As reported by McNeece et al. the intermediates for the diacyl pyrrole were used without purification or characterization between steps. Adding RCOOH (R = *p*Tol) to 2-mercaptophenol in $POCl_3$ and heating to 110 ˚C for ten minutes yielded the benzothioloxium salt, which was isolated by precipitation with HBF_4 and ether (**Scheme 3.1A**, Step a). **Caution:** quenching of large quantities of $POCl_3$ can lead to large runaway exotherms that can occur rapidly and unexpectedly. Next, addition of pyrrole to the benzothioloxium salt in acetonitrile at room termpature in presence of pyridine led to a hot yellow solution which was stirred for 45 minutes, affording the benzothioloxium protected pyrrole as a brown oil after extraction with $CHCl_3$ and a 5% $NaOH_{(aq)}$ wash (**Scheme 3.1A**, step b). This oil was suspended in glacial acetic acid, and 30% H_2O_2 was added, at which point the reaction mixutre was heated to 110 ˚C for 30 minutes. After cooling, H_2O and $CHCl_3$ were added and the $CHCl_3$ layer was washed with 10% $NaOH_{(aq)}$. After evaporation, washing the solid with methanol afforded the diacylpyrrole as an offwhite solid (30-40% overall yield)[133].

Iodoferrocene was synthesized according to literature[73] by lithiation of ferrocene with Schlosser base (equimolar ^{t}BuLi/^{t}BuOK) in THF at -78 ˚C, and subsequent lithium-halogen exchange with elemental iodine (1 equiv. vs ^{t}BuLi). An excess (1.5-2 equiv.) of ^{t}BulLi/^{t}BuOK can be used to moderately increase yields without dilithiation. Extraction with hexanes and washing with sat. thiosulfate afforded iodoferrocene in good yields (**Scheme 3.1B**, step a; typical yields of 60-80%). Iodoferrocene was aminated with 30% NH_4OH in EtOH at 90 ˚C for 6 hours in a pressure vessel using a Fe_2O_3/CuI catalyst system (**Scheme 3.1B**, step b).[74] After dilution with ether and aqeuous

base wash, the crude amino ferrocene was purified by column chromotography on silica using a 20-70% EtOAc/hexanes gradient to give a polycrystaline orange solid (typical yields: 40-60%). Note: aminoferrocene is moderately air sensitive and oxidation products can interfere with the subsequent chemistry; we recommend storage under inert atmosphere or purification before use. After repeated use, NH_4OH degrades viton o-rings, which can lead to reaction failure and/or low yields due to leakage and loss of ammonia and/or introduction of oxygen. The o-ring on the pressure vessel should be inspected and replaced (if necssary) before use. Unfortunately, the subsequent imine condensation (**Scheme 3.1C**, step a) suffers from significant thermodynamic and kinetic limitations, as reported by McNeece et al., who condensed the diketone at 140 °C in neat cyclohexylamine for 48 h. Since aminoferrocene is a sublimable solid and the more precious substrate, modification of this procedure was required. We find that affixing a Soxhlet apparatus filled with activated (400 °C under diaphragm pump vacuum for 24 h) molecular sieves[134] efficiently desiccates the reaction, enabling high conversions of the diacylpyrrole to roughly 50% diiminopyrrole and 40% monoiminopyrrole. The reaction times appear to be dictated by the water removal rate, which depends on factors such as scale and glassware, so conversions were checked every 24 h by NMR until conversion halted. The monoimine can be isolated for further condensation reactions if desired. An additional modification was replacing the acetic acid catalyst with diphenyl acetic acid to prevent azeotropic acid removal. All reaction components are readily separated by chromatography on *deactivated* basic alumina (5-10% w/w H_2O/Al_2O_3 starting from Bockman I grade activated alumina) using a 15-40% EtOAc/hexanes gradient. Using activated alumina as received resulted in strong adsorption to the solid phase and poor separation, while silica chromatography resulted in rapid hydrolysis and/or protonation depending on the level of silica hydration. Protonation is readily identified by conversion to a green species. Red crystals of

Fc_2PyrDIH (**1**) can be obtained from layered water/THF, and the structure was verified by X-ray diffraction (**Figure 3.2A**). See below for additional **1** structural information.

As expected, addition of 1 eq. of $AgBF_4$ in THF to Fc_2PyrDIH in DCM led to the formation of complex $[Fc_2PyrDIH]^+[BF_4]^-$ ($\mathbf{1}^+$) (**Scheme 3.1C**, step b) which was also characterized by X-ray diffraction (**Figure 3.2B**).

Scheme 3.1. Synthetic route to Fc_2PyrDIH (**1**)

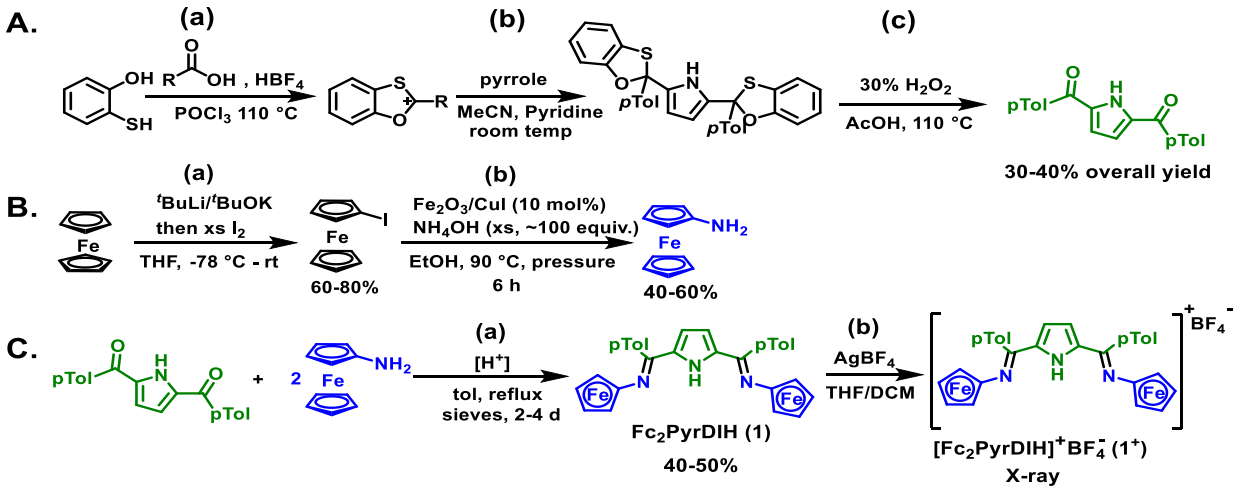

Metallation reactions of 1

Metallation of the **Fc_2PyrDIH** ligand was pursued via protodeamination of the appropriate $M(N(TMS)_2)_3$ with **Fc_2PyrDIH** (**Scheme 3.2A).** Trisamido metal precursors were employed because the bulky TMS groups apply steric pressure to prevent the free rotation of the ferrocene fragments (*vide infra*). Note that these complexes are significantly less air stable than the parent trisamides, decomposing nearly instantly and stoichiometrically on exposure to trace air or moisture. Decomposition also occurred on storage inside the glovebox. Therefore, rigorously dry and deoxygenated solvents and reaction conditions are essential, and complexes were used immediately after synthesis. For these reasons, Teflon-sealed glass flasks were used for metallation

reactions and o-ring sealed glassware for workup and product isolation. Recycling of solvent for extraction as described in the experimental minimizes moisture introduction from trace levels in solvent and facilitates purification. Thus, the addition of 1 equiv. Fc_2PyrDIH (**1**) to $Sc(N(TMS)_2)_3$ in toluene achieves quantitative formation (>95%, estimated by NMR yield) of **2-Sc** after 48h at 70˚C (**Scheme 3.2A**). The complex **2-Sc** crystallizes as purple crystals from green solutions, and the structure is verified by X-ray diffraction (**Figure 3.2C**) and further characterized by NMR and UV/vis-NIR. For additional information about the structure of **2-Sc** see below. Similarly, the analogous Lu complex was obtained (**2-Lu**) in quantitative conversions using a 1 : 1 mixture of Fc_2PyrDIH (**1**) and $Lu(N(TMS)_2)_3$. Complex **2-Lu** can be isolated as a purple powder and was characterized by NMR, UV/Vis-NIR, which supports the proposed structure. Attempts to grow single crystals suitable for X-ray measurement were unsuccessful due to partial decomposition during storage and during crystallization attempts, suggesting thermal instability.

While it was anticipated that the high steric congestion would inhibit mutiple additions of **1** to $M(N(TMS)_2)_3$ during metallation, at 1:1 stoichiometry multiple addition prevales for the larger metal ions such as Y and La (**Scheme 3.2A**). For Y, this results in ~10-20% conversion to $(Fc_2PyrDI)_2Y(N(TMS)_2)$ (**3-Y**) and nearly 50% conversion to the analogous La complex, **3-La**. The addition of 2 equiv. of **1** to $Y(N(TMS)_2)_3$ affords no **1-Y** at the end of the reaction, but the product displays the same ^{1}H NMR resonances as the impurities ovserved during **2-Y** synthesis, implicating **3-Y** as the likely source of the extra NMR resonances (**Figures B.12)**. The structure of **3-Y** is also supported by X-ray diffraction (**Figure 3.2D).** Note that the same reaction using $Sc(N(TMS)_2)_3$ (**Scheme 3.2B**, **Figure B.10**) does not result in multiple products, as judged by NMR, using either 1 or 2 equiv. of **1**. The formation of only **2-Sc** suggests that the smaller Sc^{+3} size impedes the formation of **3-Sc**. In the case of La, triple addition is also observed, yielding a

9-coordinate compound (**4-La**), $(Fc_2PyrDI)_3La$. This species was challenging to observe via NMR due to broad features that overlap with multiple side products. However, it was characterized by X-ray diffraction (**Figure 3.2E**) during unsuccesful attempts to isolate **2-La.** Observation by single-crystal diffraction suggests that **4-La** is a possible reaction product, indicating the consequence of the large La^{+3} ionic radius on available metal-ligand stoichiometries, though does not confirm it as a primary reaction product. Attempts to grow suitable X-ray crystals of **2-Y** and **2-La** were unsuccessful, probably due to the presence of the over-addition products **3-Y**, **3-La,** and **4-La**, which tend to crystallize first.

Scheme 3.2. A. Yield results of 1:1 equiv. metallation reactions of ligand **1** with various $M(N(TMS)_2)_3$ precursors. **B**. Results of in situ NMR reactions with two ligand equivalents to the various **3-**Metal structures. Yields in blue are isolated yields, while others are NMR yields.

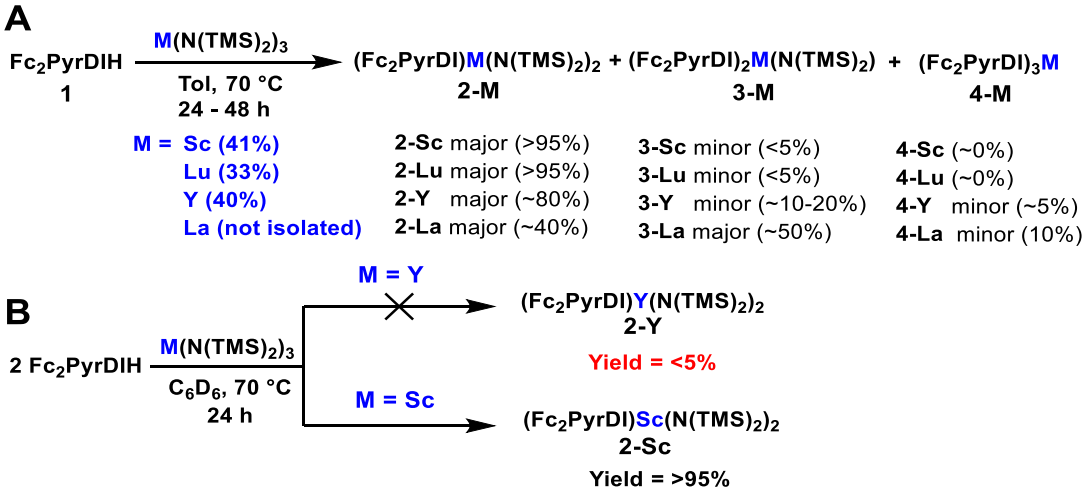

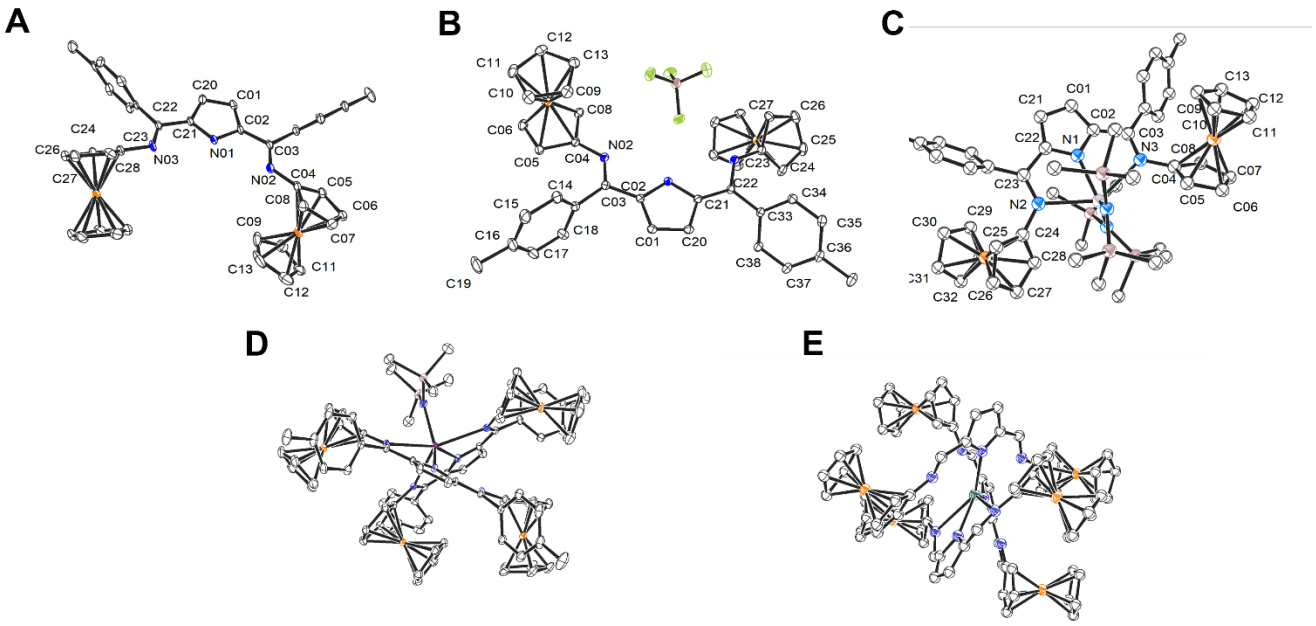

Figure 3.2. Crystal structures of **A**. $Fc_2PyrDIH$ (**1**), **B**. $[Fc_2PyrDIH]^+[BF_4]^-$ ($\mathbf{1}^+$), **C**. $(Fc_2PyrDI)_2Sc(N(TMS)_2)_2$ (**2-Sc**), **D.** $(Fc_2PyrDI)_2YN(TMS)_2$ (**3-Y**) **E.** $(Fc_2PyrDI)_3La$ (**4-La**). Ellipsoids are drawn at 50% probability, and hydrogen atoms are removed for clarity. For **E.** *p*-tol groups are omitted for clarity and ellipsoids are drawn isotropically due to extensive disorder which renders the structure difficult to otherwise inspect. See **Table 3.1** for the key bonding metrics of **1**, $\mathbf{1}^+$, and **2-Sc**

The low thermal stability of **2-Y** and **2-La**, which tend to decompose upon crystalization attempts, is another reason for the challenges in their isolation. The **2-M** complexes can be isolated in good purity by multiple heptane or pentane washes affording materials with fewer impurities based on NMR characterization. However, significant yield losses are observed, and the **3-M** complexes are still present in small quantities in **2-Y** samples (**Figure B.5**). Note that selectivity for the mono substituted **2-M** complexes can be enhanced by using stoichiometric excesses of

Table 3.1. Key bonding metrics for the indicated structures in **Figure 2** (Å)

Fc_2PyrDIH (1)			
Fc1 torsion	48.6(3) °	Fc2 torsion	29.4(3) °
Fc1 Cp-Cp distance	3.314(2)	Fc2 Cp-Cp distance	3.290(2)
C03 – N2	1.291(4)	C01-C21	1.413(4)
N1 – C02	1.374(3)	C01 – C02	1.389(5)
N2 – C04	1.403(4)	C02 – C03	1.456(4)
[Fc2PyrDIH][BF_4] (1^+)			
Fc1 torsion	29.75(8) °	Fc2 torsion	6.11(8) °
Fc1 Cp-Cp distance	3.303(1)	Fc2 Cp-Cp distance	3.291(1)
C03 – N2	1.328(1)	C01 – C21	1.294(1)
N1 – C02	1.381(1)	C01 – C02	1.410(1)
N2 – C04	1.414(1)	C02 – C03	1.421(1)
		C23 – N3	1.294(1)
N1 – C22	1.356(1)	C21 – C22	1.400(1)
N3 – C24	1.395(1)	C22 – C23	1.455(1)
Fc_2PyrDISc(N(TMS)$_2$)$_2$ (2-Sc)			
Fc1 torsion	35.8(2)	Fc2 torsion	38.4(2)
Fc1 Cp-Cp distance	3.303(1)	Fc2 Cp-Cp distance	3.304(2)
C03 – N2	1.307(3)	C01 – C21	1.404(2)
N1 – C02	1.353(2)	C01 – C02	1.403(4)
N2 – C04	1.424(3)	C02 – C03	1.454(3)

$M(N(TMS)_2)_3$ reagents, which suppresses multiple Fc_2PyrDIH addition. However, the excess lipophilic TMS groups in the reaction crude hindered isolation by crystalization or trituration. Attempts to sublime off the excess metal precursor before pentane washing also led to diminished isolated yields despite improved product selectivity in the crude.

Solid State Structure Characterization

Single crystals of Fc_2PyrDIH (**Figure 3.2A**) grew spontaneously from column fractions (approximately 20% EtOAc/hexanes) during the course of chromatography. Single crystals of $[Fc_2PyrDIH]^+[BF_4]^-$ (**1**$^+$) (**Figure 3.2B**) were grown by dissolving the crude product in toluene and layering with heptane. Over time, single crystals suitable for X-ray diffraction were obtained, although bulk isolable product was not obtained. The **2-Sc** was crystalized by slow evaporation of toluene into paratone oil using a vial-in-vial technique, with paratone oil in the outer vial (**Figure 3.2C**). Because **2-Y**, **2-Lu**, and **2-La** undergo decomposition and/or rearrangement during crystallization, single crystal diffraction data could not be obtained, and instead, crystals of **3-Y** and **4-La** were obtained (**Figure B.13-B.14**).

The neutral Fc_2PyrDI ligand is planar within the pyrrolyl core, with slight torsions about the Cp rings. Ferrocene torsions were calculated by taking the dihedral angle between imine carbon, imine nitrogen, Cp α carbon, and the Fe atom (e.g., C03, N2, C04, Fe1) and reporting the difference from 90° (deviation of the ferrocene ring plane from being perpendicular to the pyrrole plane) **(Figure 3.2).** Neglecting differences in ferrocene torsion, both **1** and **2-Sc** are symmetric with respect to bonding metrics, and only one side of the molecule is reported in **Table 3.1**. In contrast, the mixed valent species **1**$^+$ shows asymmetry in the bond lengths, and the ferrocenes adopt an *anti-*

conformation. For **1**$^{+}$, The region of the structure adjacent to the Fe(III) center exhibits bond elongation in the pyrrole ring

(N1-C02) and imine (C03-N2), while the Fe(II) side shows bond contraction (N1-C22, and C23-N3) compared to the unoxidized ligand **1**. The Cp-Cp distances (computed between the centroids of the Cp rings) are typical for ferrocene compounds and commensurate with oxidation to ferrocenium, as we observe an elongation of this distance.[43, 68, 135] We emphasize that oxidation state assignments are formal assignments based on a predominantly localized structure.

The Fe···Fe distance in ligand **1** is 8.834(3) Å, while the mixed valent species **1**$^{+}$ has a 9.280 Å distance. For **2-Sc,** this distance is 9.568(1) Å. Attempts to grow single crystals of **2-Y**, **2-Lu**, and **2-La** were unsuccessful. However, low-quality single crystals of **3-Y** and **4-La** were obtained in these crystalization attempts. While inadequate for analysis of bond metrics, they gave sufficient diffraction to affirmatively assign the connectivity and stoichiometry as $(Fc_2PyrDI)_2Y(N(TMS)_2)$ (**3-Y**) and $(Fc_2PyrDI)_3La$ (**4-La**). See **Figure 3.2** for these structures.

NMR Spectroscopy

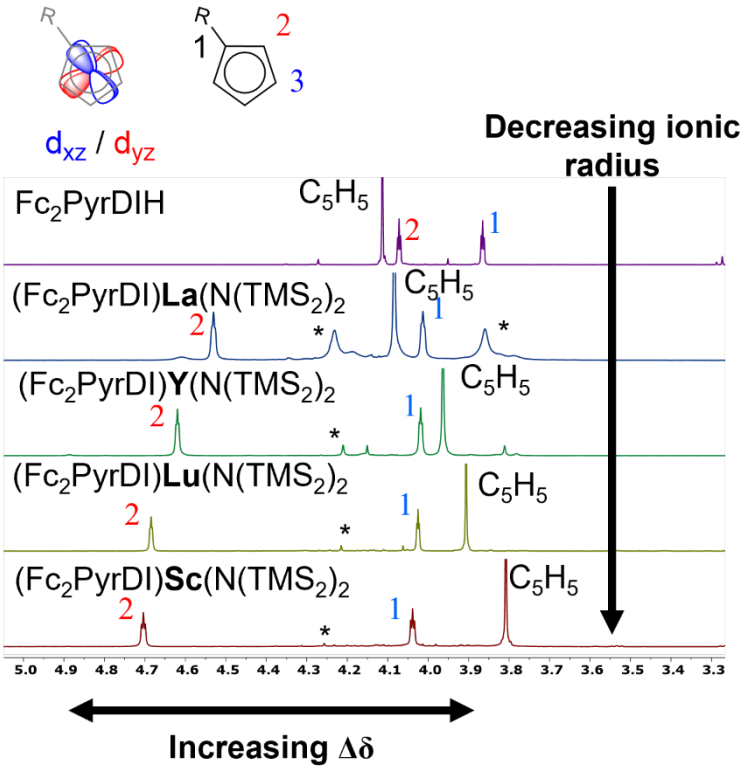

Figure 3.3: 1H NMR spectra of the ferrocene protons for Fc2PyrDI (**1**) and its metal complexes. The β and γ assignments are based on homology with previoulsy published pyridine analogs and confirmed by NOESY experimetns. Stars indicate **3-M** species

Because the pairs of ferrocene Cp protons on the functionalized ring are oriented differently along the ring, they experience different shielding effects by the d_{xz}/d_{yz} and d_{xy}/d_{x2-y2} orbitals (**Figure 3.3**). As such, electron donation and withdrawal effects of one orbital set versus the other will amplify the magnetic non-equivalence. This difference in chemical shift, Δδ, has been correlated with the electron-withdrawing/donating interaction with different d orbitals.[47, 54, 82] Note that a monotonically increasing Δδtrend is observed with Fc_2PyrDIH metalation in order of

decreasing metal ionic radius, **2-La** < **2-Y** < **2-Lu** < **2-Sc**. This trend suggests that metalation with rare earth ions engender a greater interaction between the Fc_2PyrDI π system and the ferrocene d-orbitals, and that the effect is larger when smaller metal ions are used. Such a d-π interaction would produce a significant chemical shift difference compared to when the d-orbitals do not interact.

Intriguingly the substituted Cp protons become less shielded as metal size increases, but the unsubstituted ring becomes deshielded. Differing interactions between the d orbitals and the organic π-system also affect CT properties, which is further discussed in UV/vis-NIR and DFT sections, where additional rare earth element ionic radius and electronic properties trends are identified. While we anticipate some influence on Δδ from the different covalent behaviors between Sc, Y, La, and Lu, the observed trend does not support the interpretation that the covalent bonding between pyrrole and rare earth ion drives the changes in NMR shift. Nevertheless, scandium is notable for having more accessible d-orbitals and generally increased covalent behavior, exemplified by its ability to form imido and alkilidine compounds,[50, 51, 136] which is unusual for the more ionic lanthanides. There is predicted π interactions are predicted between the pyrrole nitrogen and scandium in the 2-Sc LUMO, for example (**Figure B.16**).

Table 3.2: ^{1}H Chemical shifts for Cp protons (ppm)

	1	**2-La**	**2-Y**	**2-Lu**	**2-Sc**
Cp	4.11	4.08	3.96	3.91	4.81
Cp-γ	3.86	4.01	4.02	4.03	4.04
Cp-β	4.06	4.53	4.62	4.68	4.71
Δδ	0.20	0.52	0.60	0.65	0.67

UV-visible-NIR optical spectroscopy

Due to the conjugation of the ferrocene with the diimino pyrrole π-system, the ferrocene d-d transition takes on charge transfer character and increases in intensity, redshifts, and broadens versus an isolated ferrocene. This is illustrated in a shift from 418 nm in free ferrocene[94] to 497 nm in **1** (**Figure 3.4A**). All the present **2-M** complexes show a further redshift of this feature to ~560 nm (566, 564, and 558 nm for **2-Sc**, **2-Lu**, and **2-Y**, respectively). If 1 equiv. of the oxidant "Magic Blue" ([(*p*Br-Ph)$_3$N][SbCl$_6$]) is added to form **2-M**$^+$ species *in situ*, several new features appear between 550 – 2000 nm (**Figure 3.4B**) in all species, yielding a broadened and asymmetric band in the visible region and a new feature in the NIR. These features in the visible region are more clearly observed and analyzed via difference spectra (**Figure 3.6** in the Spectroelectrochemistry section). The NIR regions for **2-Sc**$^+$, **2-Y**$^+$, and **2-Lu**$^+$ (800-2000 nm) show low-intensity broad features, which differ significantly depending on the metal identity.

The NIR features are best viewed in **Figure 3.5A**, plotting the absorptivity versus wavenumbers since the wavelength is not linear with respect to energy and thus distorts bandshapes across this large range. Here we see that the **2-Sc** complex has higher energy and narrower feature near 11500 cm^{-1}, while **2-Y** shows lower energy and broader feature close to 8000 cm^{-1}. **2-Lu,** however, appears to share characteristics of both. As evidenced by inspecting the difference spectrum of **2-Lu** and **2-Y**, which strongly resembles the **2-Sc** NIR feature at 11500 cm^{-1} (**Figure 3.5B)**. We suggest that **2-Sc**$^+$, **2-Lu**$^+$, and **2-Y**$^+$ share similar transitions but in different weights. TDDFT analysis (vide infra) assigns the feature at 8000 cm^{-1} as an interconfigurational d-d transition, while the feature at 11500 cm^{-1} shows mix of MMCT and MLCT characters ("Metal to Mixed Metal-Ligand Charge Transfer", MMMLCT; **Figure 3.7**).

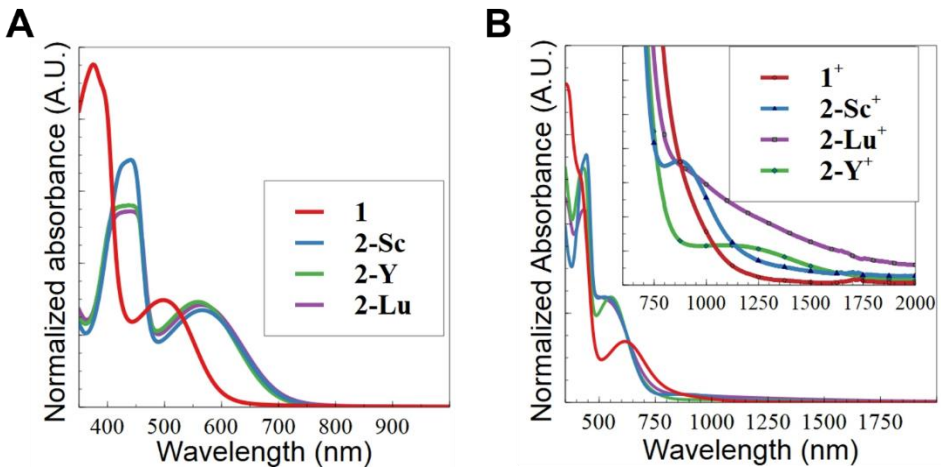

Figure 3.4. UV/visible-NIR spectra (normalized against total intensity) of Fc_2PyrDIH (**1**) and the indicated Fc_2PyrDI)M(N(TMS)$_2$)$_2$ (**2-M**)complexes (M = Sc, Y, Lu), **A.** Before and after **B.** Addition of 1 equiv. of oxidant (Magic Blue). Spectra were obtained on dimethoxyethane solutions.

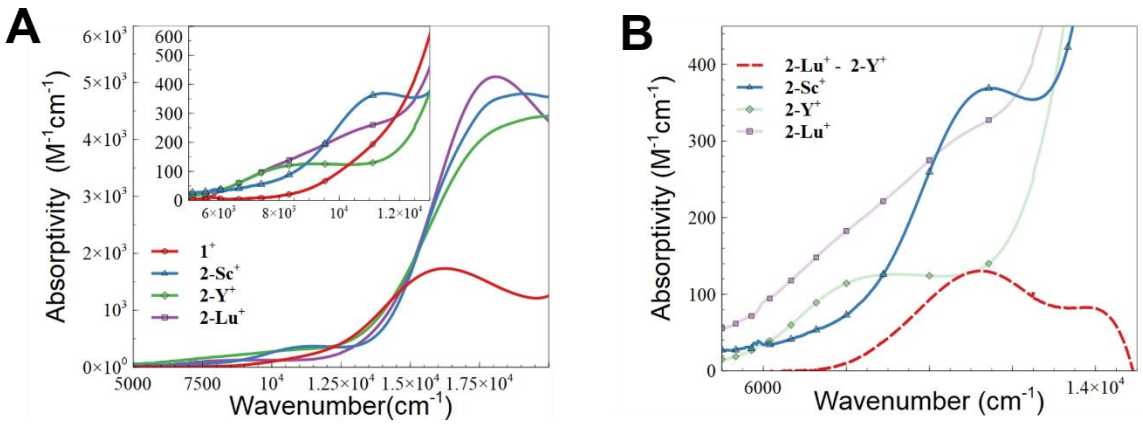

Figure 3.5. A. Replot of the UV/vis-NIR data from **Figure 4B** in absorptivity and wavenumber units. The inset shows the NIR in detail. **B.** Comparison of **2-Sc**$^+$ with the difference (red dashed) between the Y and Lu complexes (faded traces).

Spectroelectrochemistry

The visisble spectrum of the free Fc_2PyrDI ligand displays a charge transfer excitation from ferrocene at 498 nm (**Figure 3.6A**). For $[Fc_2PyrDI]^+$, low energy features are observed between 550 and 1000 nm. Regarding the asymmetry of the main features centered at 600 and 900 nm, we suggest that there are overlapping transitions between 500-700 nm transitions that are a mixture of MLCTs from ferrocene to the pyrrole core and LMCTs to Fe(III).[94] Congruency between spectra obtained by spectroelectrochemistry and chemical oxidation with Magic Blue supports production of the expected mixed valent species. For **2-Sc**, **2-Lu**, and **2-Y,** we observe similar behavior to **1**, but with features shifted to lower energies (**Figures 3.6B-6D**). While more challenging to observe in the chemical oxidation experiments, the SEC difference spectra clearly show that all **2-M** compounds have a common set of features around 900 nm but in different relative intensities and breadths. Note that the relative intensity of the 900 nm feature decreases with $\mathbf{Sc}^+ > \mathbf{Lu}^+ > \mathbf{Y}^+ \sim \mathbf{1}^+$, congruent with observations from chemical oxidation (**Figure 3.5A**). Because conventional electrochemistry solvents such as MeCN, DCM, and THF are reactive towards complexes **2-M** under electrochemical conditions, dimethoxyethane was employed since it has a similar dielectric constant and dipole moment as THF but does not undergo ring-opening polymerization. Unfortunately, the present oxidations were highly irreversible, so we limit our discussion to the optical spectra rather than the voltammograms.

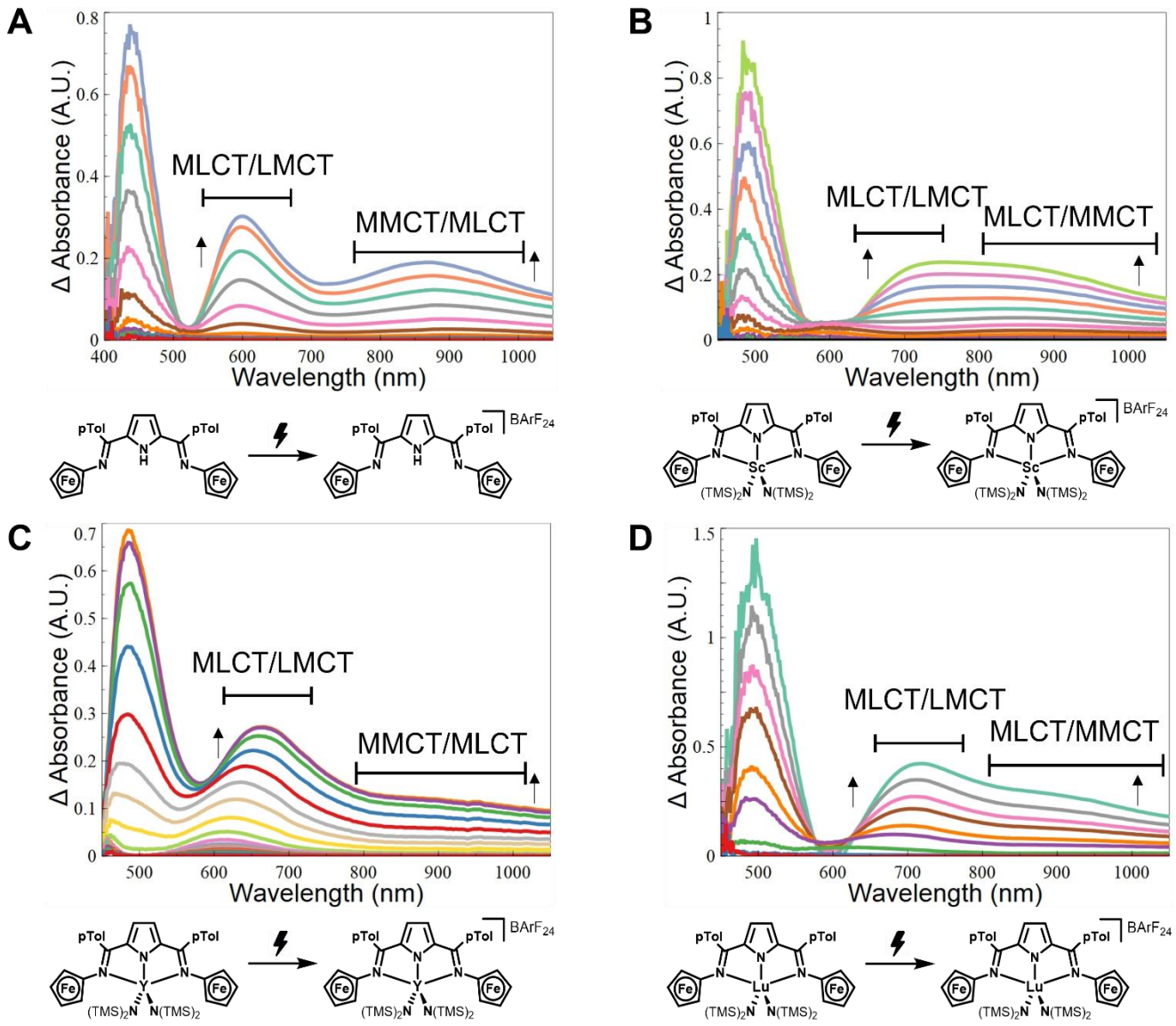

Figure 3.6. Spectroelectrochemistry plots for **1**, **2-Sc**, **2-Lu**, and **2-Y** solutions. Data was collected in dimethoxyethane with 100mM TBA-BarF_{24} electrolyte, using a linear voltage sweep of 5 mV/s. Scans were taken successively during electrolysis at ~25-50 mV increments, and plotted as difference spectra compared to the solution at 0 mV. The difference spectra change with increasing voltage in the direction indicated by arrows. Colors are arbitrary to help distinguish different traces.

Theoretical analysis

The computed bond lengths and angles for **1** are in good agreement with experiment, with the exception that the DFT optimized structure has minor, not unexpected, differences in ferrocene torsions (**Table 3.3**). **Table B.3** shows that computed optical spectra are in good agreement with experiment, with the exception of **1**, where additional low energy transitions are predicted which lead to the effective band position shifting to lower energy (535 vs 497 nm). This is likely reflects the low energy barrier to rotation of ferrocenes, leading to single point calculations to deviate from experimental solution state behavior. The $[Fc_2PyrDI]^+$ cation and $(Fc_2PyrDI)Sc(N(TMS)_2)_2$ structures were optimized from the experimental crystal structures, with the removal of the BF_4^- counterion from the $[Fc_2PyrDIH]^+[BF_4]^-$ crystal. The pyrrole metrical parameters for the computed $\mathbf{1}^+$ structure are in good agreement with crystal data despite the omission of the counterion (**Table 3.3**).

While the computed **2-M** structures are qualitatively similar throughout the series, certain bond angles and lengths show a trend with metal ionic radius. Notable elongation of the M-$N_{pyrrole}$, and M-NTMS distances is observed with increasing metal ionic radius, while the ferrocene torsions within the same molecule become more dissimilar with increasing ionic radius (ΔFc-torsion = difference between Fc1 torsion and Fc2 torsion). Previously, in less encumbered pyridyl complexes and in the free Fc_2PyrDIH ligand, oxidation causes the ferrocenes to distort and rotate out of the plane of the heterocyclic core (**Figure 3.7**).[126] However, the geometries of **2-Sc**$^+$, **2-Lu**$^+$, and **2-Y**$^+$ limit this rotation, as the *p*Tol and $N(TMS)_2$ groups restrict ferrocene group rotation. This rigidification is likely one source of the difference in charge transfer properties between $\mathbf{1}^+$ and **2-M**$^+$, and further explains the differences between **2-Sc**$^+$, **2-Lu**$^+$, and **2-Y**$^+$ (**Table 3.3**), as the ferrocene torsions are more similar in **2-Sc**$^+$ compared to **2-Lu**$^+$ and **2-Y**$^+$ since the range of stable

Table 3.3. Key computed bond lengths and torsions for **1**, $\mathbf{1}^+$, **2-M,** and **2-M**$^+$ complexes (Å)

	M-$N_{pyrrole}$	**C=N_{imine}**	**ΔC=N_{imine}**	**M-$N(TMS)_2$**	**Fc1-torsion**	**Fc2-torsion**	**ΔFc-torsion**
1	N/A	1.292 1.291	0.001	N/A	31.35 °	14.92 °	16.43 °
1^+	N/A	1.319 1.292	0.027	N/A	27.30 °	2.34 °	24.95 °
2-Sc	2.112	1.306 1.306	0.000	2.069 2.074	39.13 °	39.45 °	0.32 °
2-Sc^+	2.123	1.321 1.304	0.017	2.055 2.063	38.31 °	37.84 °	0.47 °
2-Lu	2.219	1.307 1.309	0.002	2.191 2.192	38.04 °	34.45 °	3.59 °
2-Lu^+	2.228	1.333 1.304	0.029	2.190 2.178	29.44 °	35.89 °	6.45 °
2-Y	2.274	1.307 1.309	0.002	2.236 2.239	35.17 °	25.41 °	9.76 °
2-Y^+	2.286	1.333 1.303	0.030	2.220 2.232	27.82 °	34.47 °	6.65 °

torsion angles is likely smaller in the more sterically congested complexes (**Table 3.3** column 8: "ΔFc-torsion"). For consistency of comparison, "Fc1" denotes the ferrocene that undergoes oxidation in all entries of **Table 3.3**. A shorter M-$N_{pyrrole}$ distance and shorter M-$N(TMS)_2$ distances bring the bulky $N(TMS)_2$ groups closer to the ferrocenes and limit their rotational freedom, thereby

restricting geometric changes on oxidation. This situation is also reflected in smaller changes in imine bond lengths on oxidation of **2-Sc** to **2-Sc**$^{+}$, correlating with the enforced symmetry between the ferrocene torsions. The differences in imine bond lengths in the mixed valent forms (ΔC=N, **Table 3.3** column 3) are 0.017, 0.029, and 0.030 Å for **2-Sc**$^{+}$, **2-Lu**$^{+}$, and **2-Y**$^{+}$, respectively. The degree to which a mixed valent compound must rearrange is an important parameter in optical electron transfer, and the larger rare earth metal ions appear to allow greater structural asymmetry between the Fe(II) and Fe(III) halves of the mixed valent complex—evident in both the torsions and the imine bond lengths.

The computed visible spectra of the present neutral and mixed valent complexes are in good agreement with the experiment (**Table B.3)**. The fronteir orbitals are qualitatively the same across the series of neutral compound (**1** and **2-M**, **Figure B.16**), except that in the LUMO, there is a predicted π-interaction between Sc and the pyrrole nitrogen for **2-Sc**, while this interaction is essentially nonexistent in **2-Y** and **2-Lu**. However, as seen in **Figure 3.7B**, little electron density is transferred to scandium in the 11500 cm^{-1} charge transfer—though the LUMO is mixed into the transition in significant weight, the net contribution from scandium is small. This may help explain why metal ionic radius effects dominate over covalency effects, as the rare earth ion participates comparitively little in the charge transfer. In the Marcus-Hush Classical 2-state formalism of evaluating MMCT bands, the excited state represents a direct metal-to-metal electron transfer.[107, 137] Orbitals on the bridging ligand are thus not directly important in analyzing or interpreting the experimental charge transfer between metals in a 2-state model. However, the superexchange formalism introduced by Brunschwig, Creutz, and Sutin[24, 107] incorporates additional charge transfer states involving the bridging ligand in the model. Adding these CT states provides a 3-state model for analyzing complex species where orbitals from the bridging ligand are important

in facilitating the electron transfer. Inspection of the change in electron density during the NIR transitions for **2-M**$^{+}$ complexes reveals both MMCT and MLCT character—i.e., the donor orbital is largely centered on Fe-A, and the acceptor orbital has contribution from both the bridging ligand and Fe-B. From these plots, we see that pure MMCT is not operative, as there is also strong MLCT character as well. It is known that the HOMO-LUMO gap influences superexchange mediated charge transfer,[106, 138] and the charge density of the metal ion—and thus it's ionic radius for a series of 3^{+} metal ions—may have an influence on the HOMO-LUMO gap, and consequently the intensity of a superexchange mediated charge transfer between metals. Such an effect would rationalize the difference between **1**$^{+}$ and **2-M**$^{+}$ NIR spectra, as well as the gradual CT intensity change with ionic radius (**Figure 3.4B**).

Figure 3.7 shows difference density plots for the NIR transitions at 8000 cm^{-1} and 11500 cm^{-1}. These plots reveal the difference in electron density between the ground and excited state for each transition. For all **2-M**$^{+}$ species, the 8000 cm^{-1} feature represents a symmetry forbidden d-d transfer, while at 11500 cm^{-1}, the transition takes on MMCT/MLCT mixed character. We note that as the torsion angle for the donor ferrocene ("Fc2-torsion", column 7 in **Table 3.3**) falls from **2-Sc**$^{+}$ > **2-Lu**$^{+}$ > **2-Y**$^{+}$, the amount of pyrrole character in the donor orbitals increases, as seen in **Figure 3.7** where the density loss is given by the blue shading.

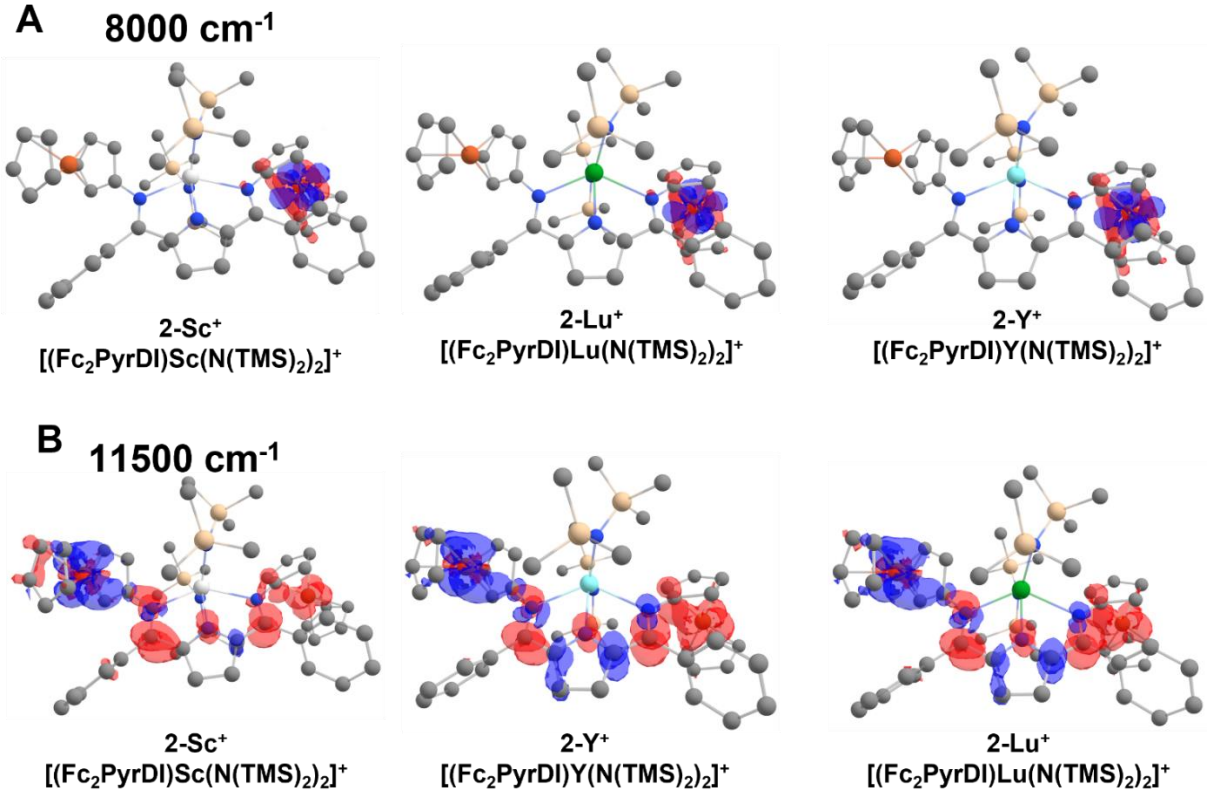

Figure 3.7. TDDFT computed difference density plots for the transitions that comprise the NIR bands for (left to right) **2-Sc**$^{+}$, **2-Lu**$^{+}$, and **2-Y**$^{+}$ for the features at, **A.** 8000cm^{-1} and **B.** 11500 cm^{-1}. Blue represents electron density loss, while red represents electron density gain.

3.2 Structural and Electronic Analysis of Bisferrocenyl Pyrrolate Complexes

While adaptations of Marcus Theory have been successfully employed to describe electron transfer and electronic structures in various mixed valent systems, its generalizability to systems that are not predominantly valence localized or delocalized remains challenging.[24, 26] This is in part because it models the wavefunctions involved as metal-centered. This assumption becomes less straightforward when the orbitals involved in the electron transfer have contributions from the bridging ligand.[109, 139] Models that include the bridging ligand then describe three different

coupling parameters: H_{AL}, H_{BL}, and $H_{AB,}$ which describe the coupling between metal A and the bridging ligand L, between metal B and the bridging ligand, and the direct coupling between metals A and B. Note for symmetric compounds $H_{AL} = H_{BL}$. Efforts continue towards refining these models include additional electronic states and vibrational couplings in an effort to better describe low energy transitions in systems as simple as biferrocene and applied to systems as complex as enzyme active sites.[24, 140] In this scheme, H_{AB} may be small, but H_{AL} and/or H_{BL} may be significant and lead to charge transfer between metals via an intermediate state. In such cases, when the electronics and geometry of the bridging ligand are mechanistically Involved in electron transfer, and greater attention must be paid to the influence of subtle structural factors from the bridging ligand.

While the different covalent bonding behaviors of Sc, Y, and Lu[141] might be expected to influence the π system and thus the optical properties arising from complexes with Fc_2PyrDI, the spectra of **2-Sc**, **2-Y**, and **2-Lu** are nearly identical. There is, however, a slight redshift across the series that correlates with metal size (**Figure 3.4A**: band energy increases 8 nm across Sc < Lu < Y). This echos observations in the NMR shifts observed for the Cp protons, where the difference in chemical shift (Δδ) between β and γ cp protons (**Figure 3.3** and **Table 3.2**) decreases with increasing size. However, upon oxidation to their mixed valent forms, more marked differences are evident in the NIR for the **2-M**$^+$ complexes. **2-Sc**$^+$ shows a more intense, higher energy, narrower NIR feature, while **2-Y**$^+$ displays a weaker, lower energy, and broader feature. **2-Lu**$^+$, however, appears to show an admixture of the two features. Thus, there do not appear to be significant differences in the optical features when the **2-M** complexes are in the neutral state where both Fe centers act as electron donors, and neither is an acceptor. However, oxidation

engenders significant differences between them when the two Fe centers make a donor-acceptor pair.

One possible origin of the above behavior is that in Class 1 and Class 2 mixed valent compounds, the metal centers have different coordination environments (bond lengths and bond angles between metal and ligands, etc.) due to the different oxidation states. Immediately after electron transfer, the structure must reorganize to accommodate the new coordination preferences of the new oxidation states at each metal center. In the highly congested **2-M**$^+$ complexes, these bonding reorganizations may be guided by steric factors. We have observed crystallographically that on oxidation, the Fe(III) center of **1**$^+$ prefers to rotate out of the plane of the bridging ligand π-system to create a torsion relative to the ferrocene Cp ring and the connected imine (**Figure 3.2B**). For all **2-M** complexes, there is no significant change in ferrocene torsion angle upon conversion to the mixed valent form (**Table 3.3**), which is a significant contrast to **1**/**1**$^+$ and pyridyl analogs (**Figure 3.1C**). Within the **2-M**/**2-M**$^+$ series, the ionic radius of the rare earth metal ion alters the size of the coordination sphere and, thus the $N(TMS)_2$-ferrocene group distance. With the bulky $N(TMS)_2$ ligands further from the ferrocenes, there is less steric pressure, allowing the ferrocenes to sample different rotations with respect to the imines, evident in the small torsion angle changes in **2-Sc**/**2-Sc**$^+$ versus **2-Lu**/**2-Lu**$^+$ and **2-Y**/**2-Y**$^+$. Thus, when small geometric differences are fixed and not allowed to average over other conformations, such small changes can significantly influence mixed valent properties. For a series of ansa-biferrocenes, Dong *et al.* found that small differences in the tilt angle (the angle from which the Cp rings deviate from parallel) of only 4.2° between ferrocene Cp rings changes the coalescence temperature on the Mössbauer timescale (~10^{-7} s) from 365 K to 265 K. Also, the tilt angle lowered the HOMO-LUMO gap by nearly 0.5 eV.[44]

The above observations and TDDFT calculations also explain why the visible spectroscopic features for all compounds are similar, as they are dominated by transitions originating from predominantly ferrocene Fe d-orbitals and are accepted by orbitals that are largely pyrrolate centered (**Figure B.16**). In contrast, the NIR transitions have a more mixed Fe-pyrrolate character in the excted state (**Figure 3.7**). Transitions with greater iron-pyrrolate delocalized character should be more influenced by ferrocene torsions, while those closer to typical MLCT would be expected to be less sensitive to the orbital overlaps between the ferrocene Fe and the pyrrolyl imine. TDDFT assigns the feature at ca. 8000 cm^{-1} to a d-d transition while predicting the feature at 11500 cm^{-1} as having MMCT character. For **2-Sc**$^+$, the 8000 cm^{-1} feature is weak and the charge transfer is predominantly at 11500 cm^{-1}. However, this is inversely true for **2-Y**$^+$**,** which only shows significant intensity at 8000 cm^{-1}, while **2-Lu**$^+$ exhibits significant intensity for both. This validates the hypothesis that the rare earth coordination sphere size drives the different optical properties, as the ferrocene torsion angles decrease with increasing metal size.

Applying the classical 2-state Marcus-Hush analysis[24, 137, 142] yields a coupling constant, H_{AB}, of 264 cm^{-1} and $\Gamma = 0.2$ for **2-Sc**$^+$, and both H_{AB} as well as $\Gamma \sim 0$ for **2-Y**$^+$ (the CT band at 11500 cm^{-1} is unresolved). We omit the **2-Lu**$^+$ analysis given the strong band overlap, but the bandshape is similar to **2-Sc**$^+$ but with lower intensity and broader (leading to intermediate H_{ab} and Γ values). Here Γ represents a delocalization parameter[142] and is given by $\Gamma = 1 - \frac{\Delta\nu_{1/2}}{\Delta\nu^{\circ}_{1/2}}$. This parameter describes how well the experimental bandshape ($\Delta\nu_{1/2}$) matches the bandshape predicted by Marcus-Hush theory, where $\Delta\nu^{\circ}_{1/2} = \sqrt{16\ln(2)\,RT\nu_{max}}$ and at room temperature this becomes $\Delta\nu^{\circ}_{1/2} = \sqrt{2310\nu_{max}}$.[143] Values of 0-0.1 describe strongly valence localized molecules, and values of 0.2-0.5 describe weakly valence delocalized molecules. Values of 0.5-1 describe strongly

delocalized systems approaching class III behavior. While a classical 2-state model with direct MMCT is likely not mechanistically applicable in the present system, as evidenced by the difference density plots showing significant pyrrolate character in these transitions (**Figure 3.7**), coupling parameters derived from 2 state models are typically in good agreement with 3 state models for weakly coupled Class II systems.[107] It should be emphasized that for these transitions, the strong bridging ligand character renders the "MMCT" assignment imprecise since the charge transfer involves more than the two metal centers used in 2-state models.[24] The energy and intensity are atypical of a general MMCT, affirming the TDDFT results that the amount of charge transfer between metals is less than that of pure MMCT's and falls between an MMCT and an MLCT.[99, 109] This mixed character helps explain the low intensity and high energy of these features. We nevertheless computed apparent coupling constants and delocalization parameters for completeness and to compare these species.

3.3 CONCLUSIONS

When molecules experience large degrees of conformational freedom, it is difficult to deconvolute molecular and electronic structures due to solution averaging of different conformations. Here we have restricted this conformational freedom to understand how minor structural changes caused by metal ionic radius variation influences mixed valent properties. In contrast to the previous study of pyridine trinuclear mixed valent systems (**Figure 3.1A**),[126] where we found that differing metal coordination chemistries have little effect on mixed valent properties, here have now focused instead on geometric factors. Previously we found that metalation of the bisferrocenylpyridinediimine ligand "switched" the system to a class II mixed valent molecule regardless of the metal identity.[126] However, in the present more congested and rigid Fc_2PyrDI system, important differences in the optical charge transfer properties of **2-M**$^+$ complexes depend

on the rare earth ion radius employed, thereby increasing the coupling strength for smaller ions. By bringing ancillary $N(TMS)_2$ ligands closer to the ferrocenyl groups, metal ion size influences the torsional angle between the Cp rings and attached imine, and consequently, the energy, bandshape, and iron vs. pyrrolate composition of their NIR charge transfers. We conclude that greater steric repulsion between $N(TMS)_2$ ligands and ferrocenes results in a more symmetric structure that lowers the reorganization energy and enhances coupling between metal centers, as supported by the disappearance of a NIR charge transfer as metal ion size increases and steric encumbrance is relieved. While **2-Sc**$^+$ exhibits a dominant NIR feature at 11500 cm^{-1}, **2-Y**$^+$ displays one at 8000 cm^{-1}, and **2-Lu**$^+$ exhibits both features. Because MLCT states can be mixed with MMCT states, and in the Fc_2PyrDI system, these MLCT states are significantly involved, the metal-ligand electronic coupling becomes an important parameter for the overall metal-metal coupling. The compounds in this study, **2-Sc**, **2-Lu**, and **2-Y** do not engage in significant covalent bonding with the Fc_2PyrDI ligand, but we find that the size of their coordination sphere limits the rotational freedom of the ferrocenyl groups. Using the 2-state Marcus-Hush model, these bands correspond to a 264 cm^{-1} coupling constant for **2-Sc**$^+$ and a negligible value for **2-Y**$^+$. This observation gives substance to understanding structure-relationships in mixed valent compounds as we demonstrated that multiple conformers must be considered to deconvolute spectra. Inspecting molecules to determine how static or fluxional the structure is helps inform how strongly intertwined geometry and electronics will be, guiding the design of new electronically coupled systems.

3.4 EXPERIMENTAL SECTION

General Considerations. All procedures for air- and moisture-sensitive compounds were carried out with rigorous exclusion[144] of O_2 and moisture in flame or oven-dried Schlenk-type

glassware interfaced to a dual-manifold Schlenk line or Ar-fed high-vacuum ($<10^{-6}$ – 10^{-7} Torr) line using an oil diffusion pump, or in an Ar-filled Mbraun glovebox with a high capacity recirculator (<0.5 ppm O_2). Argon for high-vacuum lines (Airgas, UHP grade) was purified by passage through MnO/vermiculite and Davison 4Å molecular sieve columns.[145] Where relevant, solvents are designated as from a Pure Process Technology solvent purification system (SPS), or dried more rigorously. More rigorously dried solvents were stirred over potassium metal overnight, after which a few large crystals of benzophenone were added. After degassing through freeze-pump-thaw cycles, the Teflon-sealed flask (still containing potassium) was stirred overnight at 70 °C (or 40 °C for pentane). For pentane and heptane, a small amount of tetraglyme or 18-crown-6 was added to improve the solubility of the ketyl radical. NMR solvents were purchased from Cambridge Isotope Laboratories or Sigma Aldrich (>99 atom % D). Solvents used for NMR characterization of pyrrole and ferrocene intermediates were used as received, while C_6D_6 for characterization of rare earth complexes was dried over potassium metal as described above. Iodoferrocene,[73] aminoferrocene,[74] metal tris(bistrimethylsilyl) amides (metal = Sc, Y, Lu, La)[146], and 2,5-ditolylacetylpyrrole[133] were synthesized according to literature procedures.

Physical and Analytical Measurements. Solution ^1H and ^{13}C NMR spectra were recorded on either a 400 MHz Bruker Avance III Nanobay system with a BBFO Smart probe or a 500 MHz Bruker Avance III HD system equipped with a BBO Prodigy probe. Chemical shifts for ^1H and ^{13}C spectra were referenced using residual solvent resonances and are reported relative to tetramethylsilane (TMS). UV/vis-NIR measurements were taken on an Agilent Cary 5000 double beam spectrophotometer, using a 2 mm quartz cuvette from Spectrocell (transparent to 3000 nm) modified with a Teflon sealed valve and ground glass joint. Elemental analyses were performed in an air-free glovebox by Midwest Microlab, Indianapolis, Indiana for % C, N, H.

Computational Methods. All quantum chemical calculations were performed using Orca5.0[147]. Geometry optimizations of all complexes were carried out at the B3LYP[120, 148-150]/ZORA-def2-TZVP level of theory, with the ZORA-def2-SVP basis set on carbon and hydrogen using ZORA relativistic and D3 dispersion corrections. Frequency and TDDFT calculations were performed at the same level of theory to validate energy minima. To compute the UV/vis-NIR spectra, solvent effects from dimethoxyethane were calculated through the Continuous Polarizable Continuum Model (CPCM)[122] using refractive index and dielectric constants of 1.379 and 7.2, respectively.[151, 152]

Crystallography. Single crystals suitable for diffraction were mounted in Paratone® oil and transferred to a cold nitrogen gas stream of a Rigaku Synergy system with a MoKα microsource. The crystal was maintained at 100.0 K during data collection. The structures were solved using Olex2 1.5[153] with the XT structure solution program[154] and refined using the ShelXL refinement package[155] with full-matrix least-square procedures.

Spectroelectrochemistry. SpecEchem was performed in an Inert Atmospheres glovebox using a 1.7 mm Pine Research electrolysis cuvette using a platinum honeycomb electrode chip with a non-aqueous $Ag/AgNO_3$ reference electrode from Pine Research. The 300-1050 nm spectra were collected using a BWTek BRC741E-02 diode array detector connected via fiber optic cables to the sample inside the glovebox. Electrolysis was carried out with a WaveNow potentiostat using a linear sweep at a rate of 5 mV/s starting at 0V vs. reference. NIR data past 1050 nm was collected by baselining a UV-vis-NIR instrument with a solvent blank. Then the sample spectrum was recorded before, and after one equivalent of Magic Blue (tris(para-bromophenyl) aminium hexachloroantimonate),[90] was added to the sample cuvette (2 mm NIR cuvette from spectrocell).

Syntheses

Fc_2PyrDIH (**1**; **Scheme 3.1**). Diphenylacetic acid (500 mg), 2,5-ditolylacetal pyrrole (2.5 g), and $FcNH_2$ (4.2 g) were added to a dry Schlenk flask under an inert atmosphere. A dry Soxhlet apparatus was attached, and the thimble was charged with activated molecular sieves similar to as described by Stoltz.[134] Then, 25 mL of toluene from an SPS was added by syringe, and the reaction was allowed to reflux briskly for four days, over which time the solution turned dark red. The reaction mixture was then cooled to room temperature, loaded onto a deactivated (5-10% H_2O/alumina) basic alumina column, and eluted with a 15-40% EtOAc/hexanes gradient. The red solid product was further purified by crystallization from a THF/H_2O layered mixture. The red crystalline product was partially dissolved in heptane, and the solvent was evaporated under vacuum to aid in removing THF and water. This procedure was repeated three times. Subsequent drying under vacuum overnight afforded a bench-stable red solid. Isolated yield: 1.1 g (45%). If desired, the intermediate monoimine can be recovered from the column as a purple solid and recycled for further imine condensations. ^{1}H NMR (C_6D_6, 500 MHz): 11.03 (s, 1H, N-H), 7.19 (m, 4H, tol-2), 6.94 (m, 4H, tol-3), 6.23 (s, 2H, pyr-3,4), 4.12 (s, 10H), 4.07 (t, J = 1.8 Hz, 4H, Cp-2), 3.87 (t, J = 1.8 Hz, Cp-3), 2.08 (s, 6H, tol-Me). ^{13}C NMR (C_6D_6, 126 MHz): 157.3(C=N), 138.6 (pyr-2,5), 137.4 (tol-4), 135.2 (tol-1), 129.4 (tol-3), 128.6 (tol-2), 115.4 (pyr-3,4), 103.1 (Cp-1), 70.0 (Cp), 67.2 (Cp-2), 66.6 (Cp-3), 21.3 (tol-Me). Anal. Calcd for **Fc_2PyrDI**, formula $C_{29}H_{27}N_3Fe_2$: C, 65.81; H, 5.14; N, 7.94. Found: C, 65.66; H, 4.99; N, 7.87.

(Fc_2PyrDI)Sc(N(TMS)$_2$)$_2$ (2-Sc; Scheme 3.2). Fc_2PyrDIH (100 mg) and Sc(N(TMS)$_2$)$_3$ (79 mg) were added to a Teflon-sealed reaction tube inside a glovebox. Then, 50 mL of toluene was vacuum transferred directly into the reaction tube from purple K/benzophenone ketyl solution. This evacuated tube was heated to 70 °C for 48 h, over which time it changed color from red to brown/green. The vessel containing the crude reaction product was taken back into the glovebox

and the solution was transferred to a flip-frit with o-ring sealed ball and socket joints. The vessel was placed under high vacuum ($1x10^{-6}$ Torr), and the toluene was evaporated. Next, heptane was vacuum transferred in (from purple K/benzophenone ketyl). Differential pressure for filtration was generated by cooling the receiving flask. After filtration, heptane was re-condensed into the solids flask with dry ice/acetone and extracted again. This process was repeated until the heptane extract was no longer brown and was a faint green color. Toluene was then added back to the solids and slowly evaporated under vacuum. When concentrated to ca. 2 mL, the toluene was decanted to leave behind purple microcrystals. A majority of the yield loss occurred during purification due to small differences in solubility between the product and impurities. The product was dried overnight under vacuum to give 64 mg, (41% yield). ^{1}H NMR (500 MHz, C_6D_6): δ = 7.57 (d, *J* = 8.1 Hz, 4H, tol-2), 6.98 (d, *J* = 8.1 Hz, 4H, tol-1), 6.23 (d, *J* = 2.5 Hz, 2H, pyr-3,4), 4.71 (t, *J* = 1.9 Hz, 4H, Cp-2), 4.04 (t, *J* = 1.9 Hz, 4H, Cp-3), 3.81 (s, Cp), 2.08 (s, 6H, tol-Me), 0.49 (s, 36H, $SiMe_3$). ^{13}C NMR (126 MHz, C_6D_6) δ = 168.9 (C=N), 147. 1 (pyr-2,5), 128.6 (tol-3), 128.3 (tol-2), 117.6 (Pyr-3,4), 103.0 (Cp-1), 70.2 (Cp), 69.3 (Cp-2), 66.6 (Cp-3), 21.3 (tol-Me), 7.1 ($SiMe_3$). While there was sufficient purity for investigation (**Figure B.4**), analytical purity was not achieved due to high sample thermal instability, necessitating characterization immediately after synthesis. Elemental analysis is therefore not provided.

(Fc_2PyrDI)Y($N(TMS)_2)_2$ (2-Y; Scheme 3.2). Fc_2PyrDIH (100 mg) and $Y(N(TMS)_2)_3$ (85 mg) were added to a Teflon-sealed reaction tube inside a glovebox. Next, 5 mL of toluene was vacuum transferred directly into the reaction tube from purple K/benzophenone ketyl solution. The evacuated tube was then heated to 70 °C for 48 h over which time it changed color from red to brown/green. The toluene containing the crude reaction product was taken into a glovebox and transferred to a flipfrit with an o-ring sealed ball and socket joints. The vessel was placed under

high-vacuum ($1x10^{-6}$ Torr), and the toluene was evaporated. Then, heptane was vacuum transferred in from purple K/benzophenone ketyl. Differential pressure for filtration was generated by cooling the receiving flask. After filtration, the heptane was re-condensed into the solids flask using dry ice/acetone and extracted again. This process was repeated until the heptane extract was no longer brown and was a faint green color. A majority of the yield loss occurred during purification due to small differences in solubility between the product and impurities. Vacuum drying overnight afforded the product as a purple solid (65 mg, 40% yield) ^{1}H NMR (500 MHz, C_6D_6): δ = 7.47 (d, *J* = 7.9 Hz, 4H, tol-2), 6.96 (d, *J* = 7.9 Hz, 4H, tol-3), 6.24 (s, 2H, pyr-3,4), 4.62 (t, *J* = 1.8 Hz, 4H, Cp-2), 4.02 (t, *J* = 1.8 Hz, 4H, Cp-3), 3.96 (s, 5H, Cp), 2.08 (s, 6H, tol-Me), 0.50 (s, 36H, $SiMe_3$). ^{13}C NMR (126 MHz, C_6D_6) 170.1 (C=N), 147.3 (pyr-2,5), 139.6 (tol-4), 128.6 (tol-3), 128. (tol-2), 118.7 (Pyr-3,4), 102.9 (Cp-1), 70.5 (Cp), 68.6 (Cp-2), 66.7 (Cp-3), 21.3 (tol-Me), 6.8 ($SiMe_3$). While there was sufficient purity for investigation (**Figure B.5**), analytical purity was not achieved due to high sample thermal instability necessitating characterization immediately after synthesis. Elemental analysis is therefore not provided.

(Fc_2PyrDI)Lu($N(TMS)_2)_2$ (2-Lu; Scheme 3.2). Fc_2PyrDIH (100 mg) and $Lu(N(TMS)_2)_3$ (98 mg) were added to a Teflon-sealed reaction tube inside of a glovebox. Next, 5 mL of toluene was vacuum transferred directly into the reaction tube off of purple K/benzophenone ketyl solution. This tube was heated to 70 °C for 48 h, over which time it changed color from red to brown/green. The toluene containing the crude reaction product was taken into a glovebox and transferred to a flipfrit with an o-ring sealed ball and socket joints. The vessel was placed under high-vacuum ($1x10^{-6}$ Torr), and the toluene was evaporated to dryness. Dry Heptane was vacuum transferred in (off of purple K/benzophenone ketyl), and the mixture was filtered. Differential pressure for filtration was generated by cooling the receiving flask. After filtration, the heptane was re-

condensed into the solids flask using dry ice/acetone and extracted again. This process was repeated until the heptane extract was no longer brown and was a faint green color. Most of the yield loss occurred during purification due to small differences in solubility between the product and impurities. Vacuum drying overnight affords the product as a purple solid (58 mg, 33% yield). ^{1}H NMR (500 MHz, C_6D_6): δ = 7.51 (d, *J* = 8.1 Hz, 4H, tol-3), 6.96 (d, *J* = 8.07 Hz, 4H, tol-2), 6.23 (s, 2H, pyr-3,4), 4.68 (t, *J* = 1.9 Hz, 4H, Cp-3), 4.03 (t, *J* = 1.9 Hz, 4H, Cp-2), 3.91 (s, Cp C*H*$_5$), 2.08 (s, 6H, tol-Me), 0.50 (s, 36H, $SiMe_3$). ^{13}C NMR (126 MHz, C_6D_6) δ = 169.0 (C=N), 147.0 (pyr-2,5), 139.6 (tol-4), 128.6 (tol-3) 128.3 (tol-2), 117.6 (pyr-3,4)), 102.9 (Cp-1), 70.3(Cp,), 69.3 (Cp-2), 66.6 (Cp-3), 21.5 (tol-Me), 7.1 ($SiMe_3$). While there was sufficient purity for investigation (**Figure B.7**), analytical purity was not achieved due to high sample thermal instability necessitating characterization immediately after synthesis. Elemental analysis is thus not provided.

Chapter 4

Thesis summary and outlook

Chapter 4

Chapter 1 described the underlying theory and motivation for mixead valency as a field within chemistry. Despite being studied for decades, new frontiers are being explored that examine electron transfer theory and electronic coupling on increasingly granular scales to establish more refined theories. One such area is the explicit participation of a bridging ligand in the electron transfer process. While electronic coupling has historically been seen as a somewhat exotic phenomenon, it is increasingly observed and invoked in rationalizing optical properties for materials and small molecules. More recently, it has been studied for its role in stabilizing unusual oxidation states in non-innocent ligand studies, demonstrating electronic coupling's permeation through the chemical sciences. The prevalence in various common phenomena motivates further study to understand how to both design electronic coupling into systems, and to analyze its influence in extant systems.

Through chapter 2 a series of complexes with a bis-ferrocenyl pyridinediimine ligand was studied. The various coordination chemistries of Zn, Mg, Fe, and Co were hypothesized to change the electronic coupling between ferrocenyl groups. This hypothesis was discarded as cyclic voltammetry and UV/vis experiments showed remarkably similar properties across the series. Though, crucially, the presence of the additional metal "switched on" electronic coupling between ferrocenes. The exact role that metalation had on the ligand is likely multifaceted, but templating, rigidification, and stabilization of the pyridine π system are proposed as the reasons.

Out of curiosity for the similarity in properties seen in chapter 2, a new study was conducted where instead of coordination chemistry, ionic radius was changed to study geometric effects on the electron transfer properties of trinuclear bisferrocenyl complexes. To this end, rare earth elements were employed because in contrast to transition metals they exhibit remarkably

similar coordination chemistry but vary in size. Ultimately a trend was observed between ionic radius and chemical shifts in NMR, torsion angles in computed geometries, and intensity of NIR charge transfers. Because the only free variable is the ionic radius and its consequent impact on ligand bond angles, we observed evidence that small geometric effects can be influential when structures are rigid and prevented from undergoing rotational averaging.

From all these data and analyses we see that detailed study of molecular and electronic structure for bridging ligands is important for evaluating electronic coupling in mixed valent systems. Modern spectroscopic work focuses on ultrafast techniques to explore vibrational contributions to electron transfer to better understand mechanism. I hope this thesis helps expand the chemical space for study at such increasingly nuanced and detailed scales.

REFERENCES

(1) Crabtree, R. H. *The Organometallic Chemistry of the Transition Metals*, 6; John Wiley & Sons: Hoboken, 2014.

(2) Holland, P. L. Distinctive Reaction Pathways at Base Metals in High-Spin Organometallic Catalysts. *Acc. Chem. Res.* **2015**, *48*, (6), 1696-1702.

(3) Resta, R. Charge States in Transition. *Nature.* **2008**, *453*, 735.

(4) Kaim, W. The Shrinking World of Innocent Ligands: Conventional and Non-Conventional Redox-Active Ligands. *Eur. J. Inorg. Chem.* **2012**, *2012*, (3), 343-348.

(5) Grutzmacher, H. Cooperating Ligands in Catalysis. *Angew. Chem. Int. Ed.* **2008**, *47*, (10), 1814-1818.

(6) Vlugt, J. I. Cooperative Catalysis with First-Row Late Transition Metals. *Eur. J. Inorg. Chem.* **2012**, *2012*, (3), 363-375.

(7) Kaim, W. Manifestations of Noninnocent Ligand Behavior. *Inorg. Chem.* **2011**, *50*, (20), 9752-9765.

(8) Blanchard, S.; Derat, E.; Desage-El Murr, M.; Fensterbank, L.; Malacria, M.; Mouriès-Mansuy, V. Non-Innocent Ligands: New Opportunities in Iron Catalysis. *Eur. J. Inorg. Chem.* **2012**, *2012*, (3), 376-389.

(9) Lyaskovskyy, V.; de Bruin, B. Redox Non-Innocent Ligands: Versatile New Tools to Control Catalytic Reactions. *ACS Catal.* **2012**, *2*, (2), 270-279.

(10) Chirik, P. J.; Wieghardt, K. Radical Ligands Confer Nobility on Base-Metal Catalysts. *Science.* **2010**, *327*, (5967), 794-795.

(11) Flisak, Z.; Sun, W.-H. Progression of Diiminopyridines: From Single Application to Catalytic Versatility. *ACS Catal.* **2015**, *5*, (8), 4713-4724.

(12) Gibson, V. C.; Redshaw, C.; Solan, G. A. Bis(imino)pyridines: Surprisingly Reactive Ligands and a Gateway to New Families of Catalysts. *Chem. Rev.* **2007**, *107*, 1745-1776.

(13) Knijnenburg, Q.; Gamboratta, S.; Budzelaar, P. H. M. Ligand-centered reactivity in diiminepyridine complexes. *Dalton Trans.* **2006**, 5442-5448.

(14) Enright, D.; Gambarotta, S.; Yap, G. P. A.; Budzelaar, P. H. M. The Ability of the α,α'-Diiminopyridine Ligand System to Accept Negative Charge: Isolation of Paramagnetic and Diamagnetic Trianions. *Angew. Chem. Int. Ed.* **2002**, *20*, 3873-3876.

(15) Sandoval, J. J.; Álvarez, E.; Palma, P.; Rodríguez-Delgado, A.; Cámpora, J. Neutral Bis(imino)-1,4-dihydropyridinate and Cationic Bis(imino)pyridine σ-Alkylzinc(II) Complexes as Hydride Exchange Systems: Classic Organometallic Chemistry Meets Ligand-Centered, Biomimetic Reactivity. *Organometal.* **2018**, *37*, (11), 1734-1744.

(16) Römelt, C.; Weyhermuller, T.; Wieghardt, K. Structural Characteristics of Redox-Active Pyridine-1,6-Diimine Complexes: Electronic Structures and Ligand Oxidation Levels. *Coord. Chem. Rev.* **2019**, *380*, 287-317.

(17) Tondreau, A. M.; Milsmann, C.; Patrick, A. D.; Hoyt, H. M.; Lobkovsky, E.; Wieghardt, K.; Chirik, P. J. Synthesis and Electronic Structure of Cationic, Neutral, and Anionic Bis(imino)pyridine Iron Alkyl Complexes: Evaluation of Redox Activity in Single-Component Ethylene Polymerization Catalysts. *J. Am. Chem. Soc.* **2010**, *132*, (42), 15046-15059.

(18) Bouwkamp, M. W.; Bowman, A. C.; Lobkovsky, E.; Chirik, P. J. Iron-Catalyzed [2π + 2π] Cycloaddition of α,ω-Dienes: The Importance of Redox-Active Supporting Ligands. *J. Am. Chem. Soc.* **2006**, *128*, 13340-13341.

(19) Bart, S. C.; Lobkovsky, E.; Chirik, P. J. Preparation and Molecular and Electronic Structures of Iron(0) Dinitrogen and Silane Complexes and their Application to Catalytic Hydrogenation and Hydrosilation. *J. Am. Chem. Soc.* **2004**, *126*, (42), 13794-13807.

(20) Chaudhuri, P.; Verani, C. N.; Bill, E.; Bothe, E.; Weyhermuller, T.; Wieghardt, K. Electronic Structure of Bis(o-iminobenzosemiquinonato)metal Complexes (Cu, Ni, Pd). The Art of Establishing Physical Oxidation States in Transition-Metal Complexes Containing Radical Ligands. *J. Am. Chem. Soc.* **2001**, *123*, (10), 2213-2223.

(21) de Bruin, B.; Bill, E.; Bothe, E.; Weyhermüller, T.; Wieghardt, K. Molecular and Electronic Structures of Bis(pyridine-2,6-diimine)metal Complexes $[ML_2](PF_6)_n$ (n = 0, 1, 2, 3; M = Mn, Fe, Co, Ni, Cu, Zn). *Inorg. Chem.* **2000**, *39*, 2936-2947.

(22) Hildebrandt, A.; Miesel, D.; Lang, H. Electrostatic Interactions within Mixed-Valent Compounds. *Coord. Chem. Rev.* **2018**, *371*, 56-66.

(23) Hildebrandt, A.; Lang, H. (Multi)ferrocenyl Five-Membered Heterocycles: Excellent Connecting Units for Electron Transfer Studies. *Organometal.* **2013**, *32*, (20), 5640-5653.

(24) D'Alessandro, D. M.; Keene, R. Current Trends and Future Challenges in the Experimental, Theoretical and Computational Analysis of Intervalence Charge Transfer (IVCT) Transitions. *Chem. Soc. Rev.* **2006**, *35*, (5), 424-440.

(25) Stephen, B.; Dermot, O. H. Metal−Metal Interactions in Linked Metallocenes. *Chem. Rev.* **1997**, *97*, 637-669.

(26) Demadis, K. D.; Hartshorn, C. M.; Meyer, T. J. The Localized-to-Delocalized Transition in Mixed-Valence Chemistry. *Chem. Rev.* **2001**, *101*, (9), 2655-2685.

(27) Winter, R. F. Half-Wave Potential Splittings $\Delta E_{1/2}$ as a Measure of Electronic Coupling in Mixed-Valent Systems: Triumphs and Defeats. *Organometal.* **2014**, *33*, 4517−4536.

(28) Sil, A.; Ghosh, U.; Mishra, V. K.; Mishra, S.; Patra, S. K. Synthesis, Structure, Electrochemical, and Spectroscopic Properties of Hetero-Bimetallic Ru(II)/Fe(II)-Alkynyl Organometallic Complexes. *Inorg. Chem.* **2019**, 1155-1166.

(29) Makhoul, R.; Gluyas, J. B. G.; Vincent, K. B.; Sahnoune, H.; Halet, J.-F.; Low, P. J.; Hamon, J.-R.; Lapinte, C. Redox Properties of Ferrocenyl Ene-diynyl-Bridged Cp*(dppe)M–C≡C–1,4-(C_6H_4) Complexes. *Organometal.* **2018**, *37*, (21), 4156-4171.

(30) Nemykin, V. N.; Dudkin, S. V.; Fathi-Rasekh, M.; Spaeth, A. D.; Rhoda, H. M.; Belosludov, R. V.; Barybin, M. V. Probing Electronic Communications in Heterotrinuclear Fe-Ru-Fe Molecular Wires Formed by Ruthenium(II) Tetraphenylporphyrin and Isocyanoferrocene or 1,1'-Diisocyanoferrocene Ligands. *Inorg. Chem.* **2015**, *54*, (22), 10711-10724.

(31) K. N., J.; Ray, P. C.; Matsuoka, I.; Bhadbhade, M. M.; Puranik, V. G.; Das, P. K.; Nishihara, H.; Sarkar, A. Ferrocene in Conjugation with a Fischer Carbene: Synthesis, NLO, and Electrochemical Behavior of a Novel Organometallic Push-Pull System. *Organometal.* **1999**, *18*, 3851-3858.

(32) David, E.; Thirumoorthy, K.; Palanisami, N. Ferrocene-Appended Donor—Acceptor Schiff Base: Structural, Nonlinear Optical, Aggregation-Induced Emission and Density Functional Theory Studies. *Appl. Organomet. Chem.* **2018**, *32*, (11), 1-12.

(33) Jin, W.-T.; Weng, W.-Z.; Zhou, Z.-h. Mixed-Valence Vanadium (IV/V) Glycolates and Lactates with N-Heterocycle Ligands: Localized Structures and Catalytic Oxidation of Thioanisole. *Eur. J. Inorg. Chem.* **2019**, 1228-1235.

(34) Sutradhar, M.; Kirillova, M. V.; Guedes da Silva, M. F. C.; Martins, L. M. D. R. S.; Pombeiro, A. J. L. A Hexanuclear Mixed-Valence Oxovanadium(IV,V) Complex as a Highly Efficient Alkane Oxidation Catalyst. *Inorg. Chem.* **2012**, *51*, 11229-11231.

(35) Kornecki, K. P.; Berry, J. F. Introducing a Mixed-Valent Dirhodium(II,III) Catalyst with Increased Stability in C-H Amination. *Chem. Commun.* **2012**, *48*, 12097-12099.
(36) Rossi, S.; Bisello, A.; Cardena, R.; Santi, S. Testing the Conjugative Properties of Benzodithiophene and Benzotrithiophene in Charge Transfer Multi(ferrocenyl) Systems. *Organometal.* **2018**, *37*, (22), 4242-4249.
(37) Heinze, K.; Hempel, K.; Beckmann, M. Multielectron Storage and Photo-Induced Electron Transfer in Oligonuclear Complexes Containing Ruthenium(II) Terpyridine and Ferrocene Building Blocks. *Eur. J. Inorg. Chem.* **2006**, *2006*, (10), 2040-2050.
(38) Pienkos, J. A.; Webster, A. B.; Piechota, E. J.; Agakidou, A. D.; McMillen, C. D.; Pritchett, D. Y.; Meyer, G. J.; Wagenknecht, P. S. Oxidatively Stable Ferrocenyl-π-Bridge-Titanocene D-π-A Complexes: an Electrochemical and Spectroscopic Investigation of the Mixed-Valent States. *Dalton Trans.* **2018**, *47*, (32), 10953-10964.
(39) Stanlake, L. J.; Stephan, D. W. Reactions of Zn Bis-Ferrocenyl-β-diketiminates with $[Ph_3C][B(C_6F_5)_4]$. *Dalton Trans.* **2011**, *40*, (22), 5836-5840.
(40) Ohkubo, A.; Fujita, T.; Ohba, S.; Aramaki, K.; Nishihara, H. A Novel Intramolecular Metallacycle-phosphine Reaction of an Electrochemically Oxidized Cobaltacyclopentadiene Complex. *J. Chem. Soc., Chem. Commun.* **1992**, 1553-1555.
(41) Vanicek, S.; Jochriem, M.; Hassenrück, C.; Roy, S.; Kopacka, H.; Wurst, K.; Müller, T.; Winter, R. F.; Reisner, E.; Bildstein, B. Redox-Rich Metallocene Tetrazene Complexes: Synthesis, Structure, Electrochemistry, and Catalysis. *Organometal.* **2018**, *38*, (6), 1361-1371.
(42) Rai, D. K.; Tauqeer, M.; Chatterjee, S.; Krishnan, S.; Mobin, S. M.; Mathur, P. Modulation of Electronic Communication between Two Equivalent Ferrocenyl Groups Mediated Through Tricarbonylcyclobutadieneiron. *Eur. J. Inorg. Chem.* **2019**, (5), 668-675.
(43) Hildebrandt, A.; Schaarschmidt, D.; Claus, R.; Lang, H. Influence of Electron Delocalization in Heterocyclic Core Systems on the Electrochemical Communication in 2,5-Di- and 2,3,4,5-Tetraferrocenyl Thiophenes, Furans, and Pyrroles. *Inorg. Chem.* **2011**, *50*, (21), 10623-10632.
(44) Dong, T.-Y.; Lee, S.-H.; Chang, C.-K.; Lin, H.-M.; Lin, a. K.-J. Pronounced Effects of Ring Tilting on Rates of Intramolecular Electron Transfer in Polyalkyl-Substituted Mixed-Valence Biferrocenium Triiodides. *Organometal.* **1997**, *16*, 2773-2786.
(45) Multani, K.; Stanlake, L. J. E.; Stephan, D. W. Ti and Zr complexes of ferrocenyl amidinates. *Dalton Trans.* **2010**, *39*, 8957-8966.
(46) Gibson, V. C.; Gregson, C. K. A.; Halliwell, C. M.; Long, N. J.; Oxford, P. J.; White, A. J. P.; Williams, D. J. The synthesis, coordination chemistry and ethylene polymerisation activity of ferrocenediyl nitrogen-substituted ligands and their metal complexes. *J. Organometal. Chem.* **2005**, *690*, (26), 6271-6283.
(47) Stegner, P.; Farber, C.; Oetzel, J.; Siemeling, U.; Wiesinger, M.; Langer, J.; Pan, S.; Holzmann, N.; Frenking, G.; Albold, U.; et al. d–d Dative Bonding Between Iron and the Alkaline Earth Metals Calcium, Strontium and Barium. *Angew. Chem. Int. Ed.* **2020**, *59*, 2-8.
(48) Wei, J.; Diaconescu, P. L. Redox-Switchable Ring-Opening Polymerization with Ferrocene Derivatives. *Acc. Chem. Res.* **2019**, *52*, 415-424.
(49) Green, A. G.; Kiesz, M. D.; Oria, J. V.; Elliott, A. G.; Buechler, A. K.; Hohenberger, J.; Meyer, K.; Zink, J. I.; Diaconescu, P. L. Characterization of an Iron-Ruthenium Interaction in a Ferrocene Diamide Complex. *Inorg. Chem.* **2013**, *52*, 5603-5610.
(50) Huang, W.; Carver, C. T.; Diaconescu, P. L. Transmetalation Reactions of a Scandium Complex Supported by a Ferrocene Diamide Ligand. *Inorg. Chem.* **2011**, *50*, (3), 978-984.
(51) Huang, W.; Khan, S. I.; Diaconescu, P. L. Scandium Arene Inverted-Sandwich Complexes Supported by a Ferrocene Diamide Ligand. *J. Am. Chem. Soc.* **2011**, *133*, (27), 10410-10413.
(52) Diaconescu, P. L. Reactons of Aromatic N-Heterocycles with d^0f_n-Metal Alkyl Complexes Supported by Chelating Diamide Ligands. *Acc. Chem. Res.* **2010**, *43*, (10), 1352-1363.
(53) Wong, A. W.; Miller, K. L.; Diaconescu, P. L. Reactions of aromatic N-heterocycles with a lutetium benzyl complex supported by a ferrocene-diamide ligand. *Dalton Trans.* **2010**, *39*, 6726-6731.
(54) Sato, M.; Sekino, M.; Akabori, S. $Pd(BF_4)_2$ Complexes of 1,1'-Bis[(alkyl- or aryl-)thio]-and 1,1'-Bis(diphenylphosphino)-Ferrocenes. Bond Formation Between the Fe and Pd Atoms. *J. Organometal. Chem.* **1988**, *344*, C31-C34.
(55) Nothling, M. D.; Xiao, Z.; Bhaskaran, A.; Blyth, M. T.; Bennett, C. W.; Coote, M. L.; Connal, L. A. Synthetic Catalysts Inspired by Hydrolytic Enzymes. *ACS Catal.* **2018**, *9*, (1), 168-187.
(56) Seefedlt, L. C.; Hoffman, B., M.; Dean, D. R. Electron Transfer in Nitrogenase Catalysis. *Curr. Opin. Chem. Biol.* **2012**, *16*, 19-25.
(57) Noodleman, L.; Lovell, T.; Liu, T.; Himo, F.; Torres, R. A. Insights Into Properties and Energetics of Iron–Sulfur Proteins From Simple Clusters to Nitrogenase. *Curr. Opin. Chem. Biol.* **2002**, *6*, 259-273.
(58) Lanzilotta, W. N.; Parker, V. D.; Seefeldt, L. C. Electron Transfer in Nitrogenase Analyzed by Marcus Theory: Evidence for Gating by MgATP. *Biochemistry.* **1998**, *37*, 399-407.
(59) Dutta, S. K.; Kumar, S. B.; Bhattacharyya, S.; Tiekink, E. R. T.; Chaudhury, M. Intramolecular Electron Transfer in $(BzImH)[(LOV)_2O]$ (H_2L = S-Methyl 3-((2-Hydroxyphenyl)methyl)dithiocarbazate): A Novel μ-Oxo Dinuclear Oxovanadium(IV/V) Compound with a Trapped-Valence $(V_2O_3)^{3+}$ Core. *Inorg. Chem.* **1997**, 4954-4960.
(60) Beinert, H.; Holm, R. H.; Münck, E. Iron-Sulfur Clusters: Nature's Modular, Multipurpose Structures. *Science.* **1997**, *277*, 653-659.
(61) Hassner, M.; Fiedler, J.; Ringenberg, M. R. (Spectro)electrochemical and Electrocatalytic Investigation of 1,1'-Dithiolatoferrocene-Hexacarbonyldiiron. *Inorg. Chem.* **2019**, *58*, (3), 1742-1745.
(62) Nemykin, V. N.; Purchel, A. A.; Spaeth, A. D.; Barybin, M. V. Probing the Electronic Properties of a Trinuclear Molecular Wire Involving Isocyanoferrocene and Iron(II) Phthalocyanine Motifs. *Inorg. Chem.* **2013**, *52*, (19), 11004-11012.
(63) Kaleta, K.; Hildebrandt, A.; Strehler, F.; Arndt, P.; Jiao, H.; Spannenberg, A.; Lang, H.; Rosenthal, U. Ferrocenyl-Substituted Metallacycles of Titanocenes: Oligocyclopentadienyl Complexes with Promising Properties. *Angew. Chem. Int. Ed.* **2011**, *50*, (47), 11248-11252.
(64) Nakaya, T.; Namiki, K.; Murata, M.; Kanaizuka, K.; Kurashina, M.; Fujita, T.; Nishihara, H. Electronic Communication in the Mixed-valence States of Cyclobutadienecobalt Complexes having Two Ferrocenes and Two Anthraquinones. *J. Inorg. Organomet. Polym.* **2007**, *18*, (1), 124-130.
(65) Jing, S.; Morley, C. P.; Webster, C. A.; Di Vaira, M. Synthesis and Characterization of Pd and Pt Complexes of 1,3-Bis(ferrocenylchalcogeno)propanes: Crystal Structures of $FcSe(CH_2)_3SeFc$ and $[M\{FcE(CH_2)_3E'Fc\}_2](PF_6)_2$ (M = Pd, Pt; E, E' = Se, Te; Fc = $[Fe(\eta^5\text{-}C_5H_5)(\eta^5\text{-}C_5H_4)]$). *Dalton Trans.* **2006**, (36), 4335-4342.
(66) Dong, T.-Y.; Lin, M.-c.; Chiang, M.; Wu, J.-Y. Development of Polynuclear Molecular Wires Containing Ruthenium(II) Terpyridine Complexes. *Organometal.* **2004**, *23*, 3921-3930.
(67) Lehrich, S. W.; Hildebrandt, A.; Korb, M.; Lang, H. Electronic Modification of Redox Active Ferrocenyl Termini and Their Influence on the Electrontransfer Properties of 2,5-Diferrocenyl-N-Phenyl-1*H*-Pyrroles. *J. Organometal. Chem.* **2015**, *792*, 37-45.

(68) Hildebrandt, A.; Schaarschmidt, D.; Lang, H. Electronically Intercommunicating Iron Centers in Di- and Tetraferrocenyl Pyrroles. *Organometal.* **2011**, *30*, (3), 556-563.
(69) Shah, H. H.; Al-Balushi, R. A.; Al-Suti, M. K.; Khan, M. S.; Woodall, C. H.; Molloy, K. C.; Raithby, P. R.; Robinson, T. P.; Dale, S. E.; Marken, F. Long-Range Intramolecular Electronic Communication in Bis(ferrocenylethynyl) Complexes Incorporating Conjugated Heterocyclic Spacers: Synthesis, Crystallography, and Electrochemistry. *Inorg. Chem.* **2013**, *52*, (9), 4898-4908.
(70) Rohde, G. T.; Sabin, J. R.; Barrett, C. D.; Nemykin, V. N. Long-Range Metal–Metal Coupling in Transition-Metal 5,10,15,20-Tetraferrocenylporphyrins. *New. J. Chem.* **2011**, *35*, (7), 1440-1448.
(71) Magdzinski, E.; Gobbo, P.; Workentin, M. S.; Ragogna, P. J. A Novel Diiminopyridine Ligand Containing Redox Active Co(III) mixed sandwich complexes. *Inorg. Chem.* **2013**, *52*, 11311-11319.
(72) Magdzinski, E.; Gobbo, P.; Martin, C. D.; Workentin, M. S.; Ragogna, P. J. The Syntheses and Electrochemical Studies of a Ferrocene Substituted Diiminopyridine Ligand and its P, S, Se, and Te Complexes. *Inorg. Chem.* **2012**, *51*, (15), 8425-8432.
(73) Roemer, M.; Nijhuis, C. A. Syntheses and Purification of the Versatile Synthons Iodoferrocene and 1,1'-Diiodoferrocene. *Dalton Trans.* **2014**, *43*, (31), 11815-11818.
(74) Leonidova, A.; Joshi, T.; Nipkow, D.; Frei, A.; Penner, J.-E.; Konatschnig, S.; Patra, M.; Gasser, G. An Environmentally Benign and Cost-Effective Synthesis of Aminoferrocene and Aminoruthenocene. *Organometal.* **2013**, *32*, (6), 2037-2040.
(75) Görl, C.; Beck, N.; Kleiber, K.; Alt, H. G. Iron(III) Complexes with Meta-Substituted Bis(arylimino)pyridine Ligands: Catalyst Precursors for the Selective Oligomerization of Ethylene. *J. Mol. Catal. A: Chem.* **2012**, *352*, 110-127.
(76) Britovsek, G. J. P.; Bruce, M.; Gibson, V. C.; Kimberley, B. S.; Maddox, P. J.; Mastroianni, S.; McTavish, S. J.; Redshaw, C.; Solan, G. A.; Stromberg, S.; et al. Iron and Cobalt Ethylene Polymerization Catalysts Bearing 2,6-Bis(imino)pyridyl Ligands: Synthesis, Structures, and Polymerization Studies. *J. Am. Chem. Soc.* **1999**, *121*, (38), 8728-8740.
(77) Small, B. L.; Brookhart, M.; Bennett, A. M. A. Highly Active Iron and Cobalt Catalysts for the Polymerization of Ethylene. *J. Am. Chem. Soc.* **1998**, *120*, 4049-4050.
(78) Yousef, R. I.; Walfort, B.; Rüffer, T.; Wagner, C.; Schmidt, H.; Herzog, R.; Steinborn, D. Synthesis, Characterization and Schlenk Equilibrium Studies of Methylmagnesium Compounds with O- and N-donor Ligands–the Unexpected Behavior of [MgMeBr(pmdta)] (pmdta = N, N, N', N", N" -Pentamethyldiethylenetriamine). *J. Organometal. Chem.* **2005**, *690*, 1178-1191.
(79) Wright, G. F. The Relative Reactivities of Methylmagnesium Chloride and Dimethylmagnesium. *J. Am. Chem. Soc.* **1939**, *71*, (5), 1152-1156.
(80) Rankin, D. W. H., Mitzel, N. W., Morrison, C. A. *Structural Methods in Molecular Inorganic Chemistry*, John Wiley & Sons: Chichester, 2013.
(81) Stevenson, P. J. Second-Order NMR Spectra at High Field of Common Organic Functional Groups. *Org. Biomol. Chem.* **2011**, *9*, 2078-2084.
(82) Akabori, S.; Kumagai, T.; Shirahige, T. Preparation of Novel Platinum and Palladium Complexes by Reaction of 1,1'-Metallocenedichalcogenols with Tetrakis(triphenylphosphine)palladium(0) or -platinum(0). The Important Role of the Coordinating Ability of the Metal Atom of the Metallocene in Product Formation. *Organometal.* **1987**, *6*, 526-531.
(83) Akabori, S.; Kumagai, T.; Shirahige, T. Preparation and Crystal Structures of (1,1'-Ruthenocenedithiolato-*S,S',Ru*)(triphenylphosphine)-nickel(II) and (1,1'-Metallocenedioxalato-*o,o',Fe*-(or *Ru*))(triphenylphosphine)palladium(II): The Metal (Fe or Ru)-Metal (Pd or Ni) Dative Bond. *Organometal.* **1987**, *6*, 2105-2109.
(84) Russell, S. K.; Bowman, A. C.; Lobkovsky, E.; Wieghardt, K.; Chirik, P. J. Synthesis and Electronic Structure of Reduced Bis(imino)pyridine Manganese Compounds. *Eur. J. Inorg. Chem.* **2012**, *2012*, (3), 535-545.
(85) Bart, S. C.; Chłopek, K.; Bill, E.; Bouwkamp, M. W.; Lobkovsky, E.; Neese, F.; Wieghardt, K.; Chirik, P. J. Electronic Structure of Bis(imino)pyridine Iron Dichloride, Monochloride, and Neutral Ligand Complexes: A Combined Structural, Spectroscopic, and Computational Study. *J. Am. Chem. Soc.* **2006**, *128*, 13901-13912.
(86) Schulz, J.; Uhlík, F.; Speck, J. M.; Císařová, I.; Lang, H.; Štěpnička, P. Synthesis, Crystal Structures, and Electrochemical Behavior of Fe–Ru Heterobimetallic Complexes with Bridged Metallocene Units. *Organometal.* **2014**, *33*, (18), 5020-5032.
(87) Tahara, K.; Akita, T.; Katao, S.; Kikuchi, J.-i. Construction of Di- and Tetra-Ferrocenyl Spiroborate Complexes from Catechol Building Blocks and their Redox Behaviors. *Dalton Trans.* **2014**, *43*, (3), 1368-1379.
(88) Noss, M. E.; Hylden, A. T.; Carroll, P. J.; Berry, D. H. Electrochemistry of Ruthenium Bis(imino)pyridine Compounds: Evidence for an ECE Mechanism and Isolation of Mono and Dicationic Complexes. *Inorg. Chem.* **2018**, *57*, (1), 435-445.
(89) LeSeur, R. J.; Geiger, W. E. Improved Electrochemistry in Low-Polarity Media Using Tetrakis(pentafluorophenyl)borate Salts as Supporting Electrolytes. *Angew. Chem. Int. Ed.* **2000**, *39*, (1), 248-250.
(90) Connelly, N. G.; Geiger, W. E. Chemical Redox Agents for Organometallic Chemistry. *Chem. Rev.* **1996**, *96*, (2), 877-910.
(91) Resa, I.; Carmona, E.; Gutierrez-Puebla, E.; Monge, A. Decamethyldizincocene, a Stable Compound of Zn(I) with a Zn–Zn Bond. *Science.* **2004**, *305*, 1136-1138.
(92) Schlöder, T.; Kaupp, M.; Riedel, S. Can Zinc Really Exist in Its Oxidation State +III? *J. Am. Chem. Soc.* **2012**, *134*, (29), 11977-11979.
(93) Duhović, S.; Diaconescu, P. L. An Experimental and Computational Study of 1,1′-Ferrocene Diamines. *Polyhedron.* **2013**, *52*, 377-388.
(94) Sohn, Y. S.; Hendrickson, D. N.; Gray, H. B. Electronic Structure of Metallocenes. *J. Am. Chem. Soc.* **1971**, *93*, (15), 3603-3612.
(95) Noviandri, I.; Brown, K. N.; Fleming, D. S.; Gulyas, P. T.; Lay, P. A.; Masters, A. F.; Phillips, L. The Decamethylferrocenium/Decamethylferrocene Redox Couple: A Superior Redox Standard to the Ferrocenium/Ferrocene Redox Couple for Studying Solvent Effects on the Thermodynamics of Electron Transfer. *J. Phys. Chem. B.* **1999**, *103*, 6713-6722.
(96) Miessler, G. L.; Fischer, p. J.; Tarr, D. A. *Inorganic Chemistry*, 5th; Pearson: Boston, 2013.
(97) Zhu, P.; Zhang, X.; Wang, H.; Zhang, Y.; Bian, Y.; Jiang, J. Ferrocene-Decorated (Phthalocyaninato)(Porphyrinato) Double- and Triple-Decker Rare Earth Complexes: Synthesis, Structure, and Electrochemical Properties. *Inorg. Chem.* **2012**, *51*, (10), 5651-5659.
(98) Kaim, W.; Fiedler, J. Spectroelectrochemistry: the Best of Two Worlds. *Chem. Soc. Rev.* **2009**, *38*, 3373-3382.
(99) Hayashi, M.; Takahashi, Y.; Yoshida, Y.; Sugimoto, K.; Kitigawa, H. Role of d-Elements in a Proton−Electron Coupling of d−π Hybridized Electron Systems. *J. Am. Chem. Soc.* **2019**, *141*, (29), 11586-11693.
(100) Takashi, K.; Misako, O.; Katsuaki, M.; Akio, I.; Kazuhiro, N. Synthesis, Structure, and Cooperative Proton−Electron Transfer Reaction of Bis(5,6-diethylpyrazinedithiolato)metal Complexes (M) Ni, Pd, Pt). *Inorg. Chem.* **2004**, *43*, 7301-7307.
(101) Tanabe, Y.; Nakajima, K.; Nishibayashi, Y. Phosphine Oxidation with Water and Ferrocneium(III) Cation Induced by Visible-Light Irradiation. *Chem. Eur. J.* **2018**, *24*, 18618-18622.

(102) Yamaguchi, Y.; Ding, W.; Sanderson, C. T.; Borden, M. L.; Morgan, M. J.; Kuta, C. Electronic Structure, Spectroscopy, and Photochemistry of Group 8 Metallocenes. *Coord. Chem. Rev.* **2007**, *251*, 515-524.
(103) Toma, S.; Sebestra, R. Applications of Ferrocenium Salts in Organic Synthesis. *Synthesis.* **2015**, *47*, 1683-1695.
(104) Kiernicki, J. J.; Zeller, M.; Szymczak, N. K. Examining the Generality of Metal-Ligand Cooperativity Across a Series of First-Row Transition Metals: Capture, Bond Activation, and Stabilization. *Inorg. Chem.* **2020**, *59*, (13), 9279-9286.
(105) Aramburu-Trošelj, B. M.; Oviedo, P. S.; Ramírez-Wierzbicki, I.; Baraldo, L. M.; Cadranel, A. Inversion of Donor–Acceptor Roles in Photoinduced Intervalence Charge Transfers. *Chem. Commun.* **2019**, *55*, 7659-7662.
(106) Giuffrida, G.; Campagna, S. Influence of Peripheral Ligands on the Metal-Metal Interaction in Dinuclear Metal Complexes with N-Heterocyclic Bridging Ligands. *Coord. Chem. Rev.* **1994**, *135*, (136), 517-531.
(107) Brunschwig, B. S.; Sutin, N. Optical transitions of symmetrical mixed-valence systems in the Class II–III transition regime. *Chem. Soc. Rev.* **2002**, *31*, 168-184.
(108) Wang, Q.; Zhang, S.; Cui, P.; Weberg, A. B.; Thierer, L. M.; Manor, B. C.; Gau, M. R.; Carroll, P. J.; Thomson, N. C. Interdependent Metal-Metal Bonding and Ligand Redox-Activity in a Series of Dinuclear Macrocyclic Complexes of Iron, Cobalt, and Nickel. *Inorg. Chem.* **2020**, *59*, 4200-4214.
(109) Kubo, T.; Ohashi, M.; Miyazaki, K.; Ichimura, A.; Nakajima, K. Synthesis, Structure, and Cooperative Proton−Electron Transfer Reaction of Bis(5,6-diethylpyrazinedithiolato)metal Complexes (M = Ni, Pd, Pt). *Inorg. Chem.* **2004**, *43*, 7301-7307.
(110) Paw, W.; Cummings, S. D.; Adnan, M. M.; William, C. B.; Geiger, D. K.; Eisenberg, R. Luminescent Platinum Complexes: Tuning and Using the Excited State. *Coord. Chem. Rev.* **1998**, *171*, 125-150.
(111) Pfaff, U.; Hildebrandt, A.; Korb, M.; Schaarschmidt, D.; Rosenkranz, M.; Popov, A.; Lang, H. Five-Membered Heterocycles as Linking Units in Strongly Coupled Homobimetallic Group 8 Metal Half-Sandwich Complexes. *Organometal.* **2015**, *34*, (12), 2826-2840.
(112) Podolan, G.; Hettmanczyk, L.; Hommes, P.; Sarkar, B.; Reissig, H.-U. Synthesis and (Spectro)electrochemistry of Ferrocenyl-Substituted Pyridine Derivatives. *Eur. J. Org. Chem.* **2015**, 7317-7323.
(113) Coe, B. J.; Fielden, J.; Foxon, S. P.; Asselberghs, I.; Clays, K.; Cleuvenbergen, S. V.; Brunschwig, B. S. Ferrocenyl Diquat Derivatives: Nonlinear Optical Activity, Multiple Redox States, and Unusual Reactivity. *Organometal.* **2011**, *30*, 5731-5743.
(114) Jurca, T.; Ouanounou, S.; Shih, W.; Ong, T.-G.; Yap, G. P. A.; Korobkov, I.; Gorelsky, S.; Richeson, D. Structural and Electronic Trends for Five Coordinate 1st Row Transition Metal Complexes: Mn(II) to Zn(II) Captured in a Bis(iminopyridine) Framework. *Dalton Trans.* **2016**, *45*, (36), 14327-14334.
(115) Hutchison, K.; Morris, J. C.; Nile, T. A.; Walsh, J. L.; Thompson, D. W.; Petersen, J. D.; Schoonover, J. R. Spectroscopic and Photophysical Properties of Complexes of 4′-Ferrocenyl-2,2′:6′,2″-terpyridine and Related Ligands. *Inorg. Chem.* **1999**, *38*, 2516-2523.
(116) Gallagher, M.; Wieder., N. L.; Dioumaev, V. K.; Carroll, P. J.; Berry, D. H. Low-Valent Ruthenium Complexes of the Non-innocent 2,6-Bis(imino)pyridine Ligand. *Organometal.* **2010**, *29*, 591-603.
(117) D'Alessandro, D. M.; Keene, F. R. Intervalence Charge Transfer (IVCT) in Trinuclear and Tetranuclear Complexes of Iron, Ruthenium, and Osmium. *Chem. Rev.* **2006**, *106*, 2270-2298.
(118) Wojdyr, M. Fityk: a general-purpose peak fitting program. *J. Appl. Crystallogr.* **2010**, *43*, 1126-1128.
(119) *Gaussian 09*; Gaussian, Inc.: Wallingford, CT, 2009.
(120) Stephens, P. J.; Devlin, F. J.; Chabalowski, C. F.; Frisch, M. J. Ab Initio Calculation of Vibrational Absorption and Circular Dichroism Spectra Using Density Functional Force Fields. *J. Phys. Chem.* **1994**, *98*, (45), 11623-11627.
(121) Becke, A. D. Density-Functional Thermochemistry. III. The Role of Exact Exchange. *J. Phys. Chem.* **1993**, *98*, 5648-5652.
(122) Scalmani, G.; Frisch, M., J. Continuous surface charge polarizable continuum models of solvation. I. General formalism. *J. Phys. Chem.* **2010**, *132*, 114110.
(123) Dolomanov, O. V.; Bourhis, L. J.; Gildea, R. J.; Howard, J. A.; Puschmann, H. OLEX2: a complete structure solution, refinement and analysis program. *J. Appl. Crystallogr.* **2009**, *42*, (2), 339-341.
(124) Sheldrick, G. M. A short history of SHELX. *Acta Crystallogr. Sect. A: Found. Crystallogr.* **2008**, *64*, (1), 112-122.
(125) Yakelis, N. A.; Bergman, R. G. Safe Preparation and Purification of Sodium Tetrakis[(3,5-bistrifluoromethyl)phenyl]borate ($NaBArF_{24}$): Reliable and Sensitive Analysis of Water in Solutions of Fluorinated Tetraarylborates. *Organometal.* **2005**, *24*, 3579-3581.
(126) Carter, C.; Kratish, Y.; Jurca, T.; Gao, Y.; Marks, T. J. Bis-Ferrocenyl-Pyridinediimine Trinuclear Mixed-Valent Complexes with Metal-Binding Dependent Electronic Coupling: Synthesis, Structures, and Redox-Spectroscopic Characterization. *J. Am. Chem. Soc.* **2020**, *142*, (43), 18715-18729.
(127) Connelly, N. G.; Damhus, T.; Hartshorn, R. M.; Hutton, A. T. *Nomenclature of Inorganic Chemistry*, RSC Publishing: Cambridge, 2005.
(128) Aspinall, H. C. *Chemistry of the f-Block Elements*, Gordon and Breach Science Publishers: Amsterdam, 2001.
(129) Shannon, R. D. Revised effective ionic-radii and systematic studies of interatomic distances in halides and chalcogenides. *Acta Crystallogr., Sect. A.* **1976**, *A32*, 751.
(130) Martinez-Gomez, N. C.; Vu, H. N.; Skovran, E. Lanthanide Chemistry: From Coordination in Chemical Complexes Shaping Our Technology to Coordination in Enzymes Shaping Bacterial Metabolism. *Inorg. Chem.* **2016**, *55*, (20), 10083-10089.
(131) Kong, X. H.; Wu, Q. Y.; Lan, J. H.; Wang, C. Z.; Chai, Z. F.; Nie, C. M.; Shi, W. Q. Theoretical Insights into Preorganized Pyridylpyrazole-Based Ligands toward the Separation of Am(III)/Eu(III). *Inorg. Chem.* **2018**, *57*, (23), 14810-14820.
(132) Klamm, B. E.; Windorff, C. J.; Celis-Barros, C.; Marsh, M. L.; Meeker, D. S.; Albrecht-Schmitt, T. E. Experimental and Theoretical Comparison of Transition-Metal and Actinide Tetravalent Schiff Base Coordination Complexes. *Inorg. Chem.* **2018**, *57*, (24), 15389-15398.
(133) McNeece, A. J.; Chang, M. C.; Filatov, A. S.; Anderson, J. S. Redox Activity, Ligand Protonation, and Variable Coordination Modes of Diimino-Pyrrole Complexes of Palladium. *Inorg. Chem.* **2018**, *57*, (12), 7044-7050.
(134) Wright, A. C.; Du, Y. E.; Stoltz, B. M. Small-Scale Procedure for Acid-Catalyzed Ketal Formation. *J. Org. Chem.* **2019**, *84*, (17), 11258-11260.
(135) Frenzel, P.; Korb, M.; Hildebrandt, A.; Lang, H. Synthesis and Electrochemical Behavior of Ferrocenyl-Functionalized Metallocenes $M(\eta^5\text{-}C_5H_5)_2(EFc)_2$ (M = Ti, Zr; E = O, S, Se). *Eur. J. Inorg. Chem.* **2018**, (27), 3156-3163.
(136) Clough, B. A.; Mellino, S.; Clot, E.; Mountford, P. New Scandium Borylimido Chemistry: Synthesis, Bonding, and Reactivity. *J. Am. Chem. Soc.* **2017**, *139*, (32), 11165-11183.
(137) Brunschwig, B. S.; Sutin, N. Energy surfaces, reorganization energies, and coupling elements in electron transfer. *Coord. Chem. Rev.* **1999**, *187*, (1), 233-254.

(138) Richardson, D. E.; Taube, H. Mixed-valence molecules: Electronic delocalization and stabilization. *Coord. Chem. Rev.* **1984**, *60*, 107-129.
(139) Hayashi, M.; Takahashi, Y.; Yoshida, Y.; Sugimoto, K.; Kitagawa, H. Role of d-Elements in a Proton−Electron Coupling of d−π Hybridized Electron Systems. *J. Am. Chem. Soc.* **2019**.
(140) Warratz, R.; Tuczek, F. Low-Energy Bands of Ferrocene-Ferrocenium Dimers: Bandshape Analysis with a Four-Level Two-Mode Vibronic Coupling Configuration Interaction (VCCI) Model Including Asymmetry. *Inorg. Chem.* **2009**, *48*, (8), 3591-3607.
(141) Axe, J. D.; Burns, G. Influence of Covalency upon Rare-Earth Ligand Field Splittings. *Phys. Rev.* **1966**, *152*, (1), 331-340.
(142) Brunschwig, B. S.; Creutz, C.; Sutin, N. Optical transitions of symmetrical mixed-valence systems in the Class II-III transition regime. *Chem. Soc. Rev.* **2002**, *31*, (3), 168-184.
(143) Aguirre-Etcheverry, P.; O'Hare, D. Electronic communication through unsaturated hydrocarbon bridges in homobimetallic organometallic complexes. *Chem. Rev.* **2010**, *110*, (8), 4839-4864.
(144) Borys, A. *Schlenk Line Survival Guide*. https://schlenklinesurvivalguide.com/ (accessed October 18, 2022).
(145) C R McLlwrick, C. S. P. The removal of oxygen from gas streams: applications in catalysis and gas chromatography. *J. Phys. E: Sci. Instrum.* **1973**, *6*, 1208.
(146) Bradley, D. C.; Ghotra, J. S.; Hart, F. A. Low co-ordination numbers in lanthanide and actinide compounds. Part I. The preparation and characterization of tris{bis(trimethylsilyl)-amido}lanthanides. *J. Chem. Soc., Dalton Trans.* **1973**, (10), 1021-1023.
(147) Neese, F. Software update: The ORCA program system—Version 5.0. *Wiley Interdiscip. Rev. Comput. Mol. Sci.* **2022**.
(148) Becke, A. D. Density-functional thermochemistry. III. The role of exact exchange. *J. Phys. Chem.* **1993**, *98*, (7), 5648-5652.
(149) Lee, C.; Yang, W.; Parr, R. G. Development of the Colle-Salvetti correlation-energy formula into a functional of the electron density. *Phys. Rev. B: Condens. Matter Mater. Phys.* **1988**, *37*, (2), 785-789.
(150) Vosko, S. H.; Wilk, L.; Nusair, M. Accurate spin-dependent electron liquid correlation energies for local spin density calculations: a critical analysis. *Canadian Journal of Physics.* **1980**, *58*, (8), 1200-1211.
(151) Wohlfarth, C. *Static Dielectric Constants of Pure Liquids and Binary Liquid Mixtures (Supplement to IV/6)*, Springer Materials: Heidelberg, 2008.
(152) Wohlfarth, C. *Refractive Indices of Pure Liquids and Binary Liquid Mixtures (Supplement to III/38)*, 1; Springer: Heidelberg, 2008.
(153) Dolomanov, O. V.; Blake, A. J.; Champness, N. R.; Schröder, M. OLEX: new software for visualization and analysis of extended crystal structures. *J. Appl. Crystallogr.* **2003**, *36*, (5), 1283-1284.
(154) Sheldrick, G. M. SHELXT - Integrated Space-Group and Crystal-Structure Determination. *Acta. Crystallogr. A. Found. Adv.* **2015**, *71*, (Pt 1), 3-8.
(155) Sheldrick, G. M. Crystal structure refinement with SHELXL. *Acta. Crystallogr. C. Struct. Chem.* **2015**, *71*, (Pt 1), 3-8.

Appendices

Appendix A: Supplementary information to Chapter 2

Table A.1. Crystal data and structure refinement details for reported crystals x-ray structures

Identification code	Fc_2PDI	$(Fc_2PDI)CoCl_2$	$(Fc_2PDI)ZnCl_2$	$(Fc_2PDI)FeCl_2$	$(Fc_2PDI)MgCl_2$
Empirical formula	$C_{30}H_{29}N_3Cl_4Fe_3$	$C_{31}H_{31}Cl_6CoFe_2N_3$	$C_{30}H_{29}Cl_4Fe_2N_3Zn$	$C_{30}H_{29}N_3Cl_4Fe_3$	$C_{30}H_{29}Cl_4Fe_2MgN_3$
Formula weight	305.33	828.92	750.43	740.91	709.37
Temperature/K	100	99.85	100.01	100.02	100.01
Crystal system	orthorhombic	triclinic	monoclinic	triclinic	triclinic
Space group	Pbcn	P-1	$P2_1/c$	P-1	P-1
a/Å	12.0007(8)	9.2390(11)	21.6448(7)	14.1955(3)	14.2488(10)
b/Å	12.1927(8)	12.5728(15)	8.3566(3)	14.7849(3)	14.8011(11)
c/Å	10.6658(8)	14.949(2)	16.6205(5)	16.9301(3)	16.8432(13)
α/°	90	91.582(8)	90	70.6612(9)	70.900(5)
β/°	90	94.519(8)	101.738(2)	66.7458(9)	66.706(4)
γ/°	90	110.169(7)	90	74.9582(11)	74.830(4)
Volume/$Å^3$	1560.63(19)	1622.2(4)	2943.40(17)	3046.24(11)	3047.0(4)
Z	4	2	4	4	4
$\rho_{calc}g/cm^3$	1.299	1.697	1.693	1.616	1.546
μ/mm^{-1}	0.840	1.910	12.297	1.786	1.349
F(000)	652.0	838.0	1520.0	1504.0	1448.0
Crystal size/mm^3	0.298 × 0.114 × 0.114	0.249 × 0.074 × 0.014	0.123 × 0.084 × 0.021	0.623 × 0.213 × 0.07	0.515 × 0.282 × 0.032
Radiation	MoKα (λ = 0.71073)	MoKα (λ = 0.71073)	CuKα (λ = 1.54178)	MoKα (λ = 0.71073)	MoKα (λ = 0.71073)
2Θ range for data collection/°	4.762 to 60.06	4.282 to 58.258	4.17 to 130.386	2.71 to 61.164	2.72 to 52.924
Index ranges	$-16 \le h \le 16, -16 \le k \le 17, -14 \le l \le 14$	$-12 \le h \le 12, -17 \le k \le 17, -20 \le l \le 19$	$-25 \le h \le 25, -9 \le k \le 9, -19 \le l \le 19$	$-20 \le h \le 20, -21 \le k \le 21, -23 \le l \le 24$	$-17 \le h \le 17, -18 \le k \le 18, -16 \le l \le 20$
Reflections collected	16807	23016	33048	80243	37084
Independent reflections	2275 [R_{int} = 0.0422, R_{sigma} = 0.0302]	8427 [R_{int} = 0.0523, R_{sigma} = 0.0703]	5027 [R_{int} = 0.0830, R_{sigma} = 0.0485]	18663 [R_{int} = 0.0575, R_{sigma} = 0.0514]	12305 [R_{int} = 0.0695, R_{sigma} = 0.0990]
Data/restraints/parameters	2275/0/139	8427/14/398	5027/0/363	18663/0/725	12305/0/725
Goodness-of-fit on F^2	1.043	1.031	1.022	1.077	1.039
Final R indexes [I>=2σ (I)]	R_1 = 0.0296, wR_2 = 0.0670	R_1 = 0.0426, wR_2 = 0.0920	R_1 = 0.0349, wR_2 = 0.0754	R_1 = 0.0490, wR_2 = 0.1214	R_1 = 0.0641, wR_2 = 0.1415
Final R indexes [all data]	R_1 = 0.0490, wR_2 = 0.0737	R_1 = 0.0669, wR_2 = 0.1018	R_1 = 0.0491, wR_2 = 0.0817	R_1 = 0.0661, wR_2 = 0.1314	R_1 = 0.1177, wR_2 = 0.1654
Largest diff. peak/hole / e $Å^{-3}$	0.39/-0.36	0.78/-0.77	0.46/-0.33	1.82/-1.45	0.89/-1.03

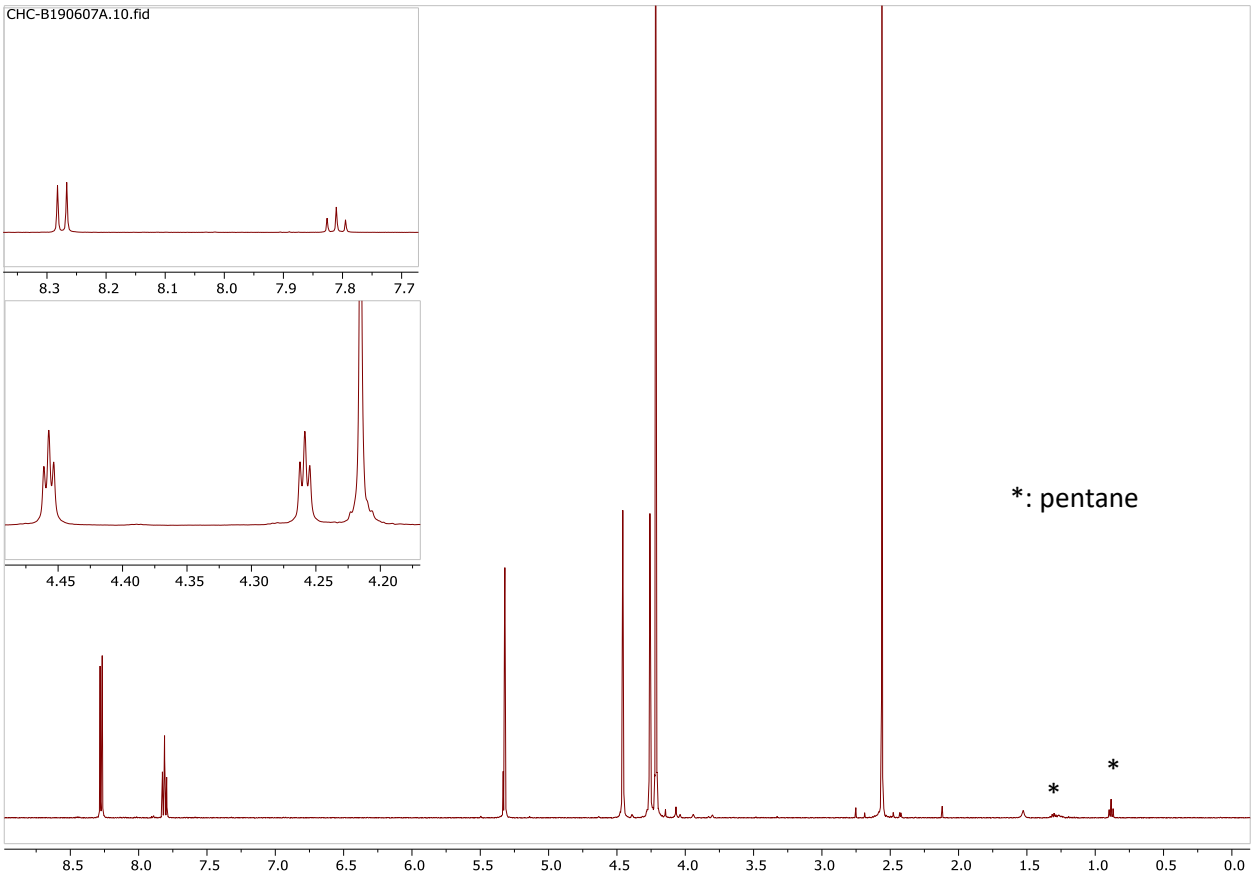

Figure A.1: 500 MHz ^{1}H NMR spectrum of Fc_2PDI in DCM

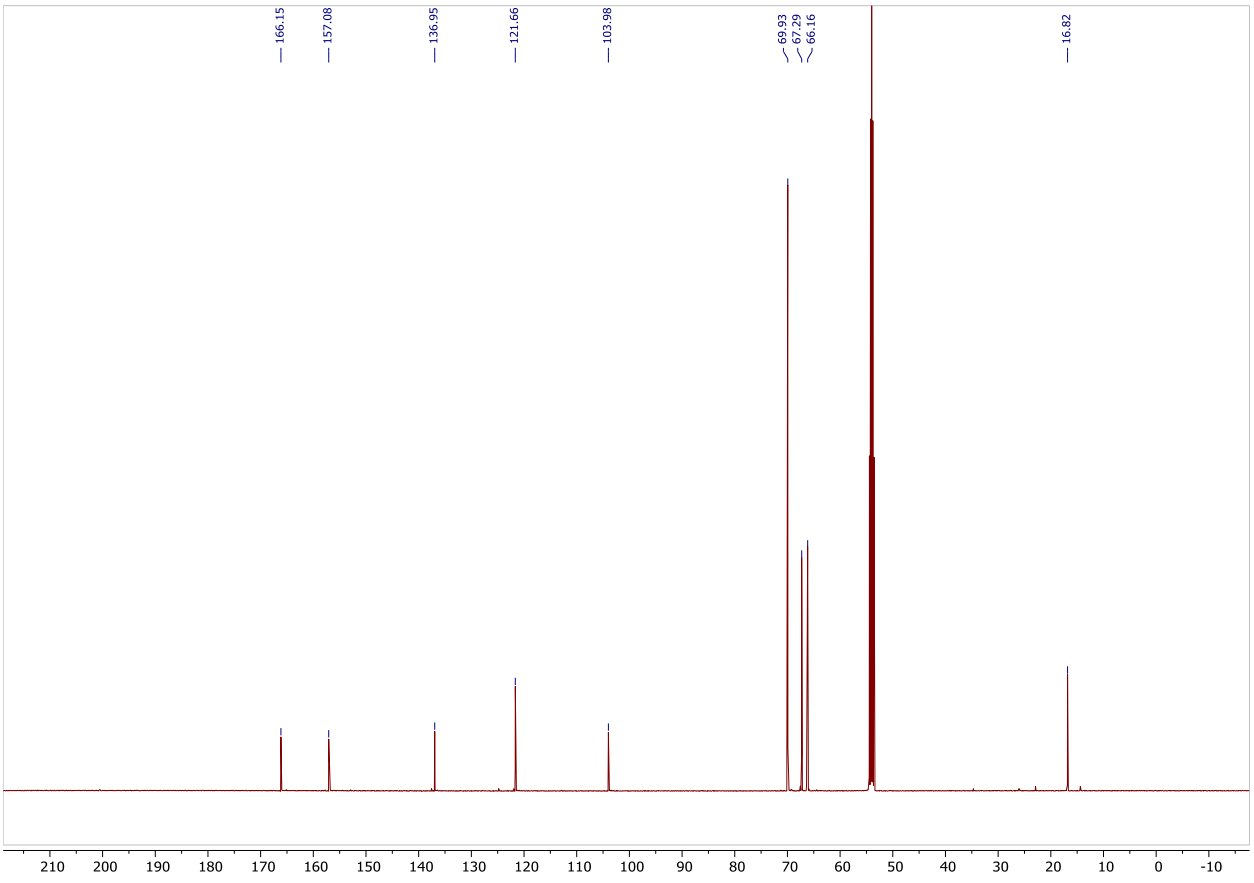

Figure A.2: 126 MHz ^{13}C NMR spectrum of Fc_2PDI in DCM

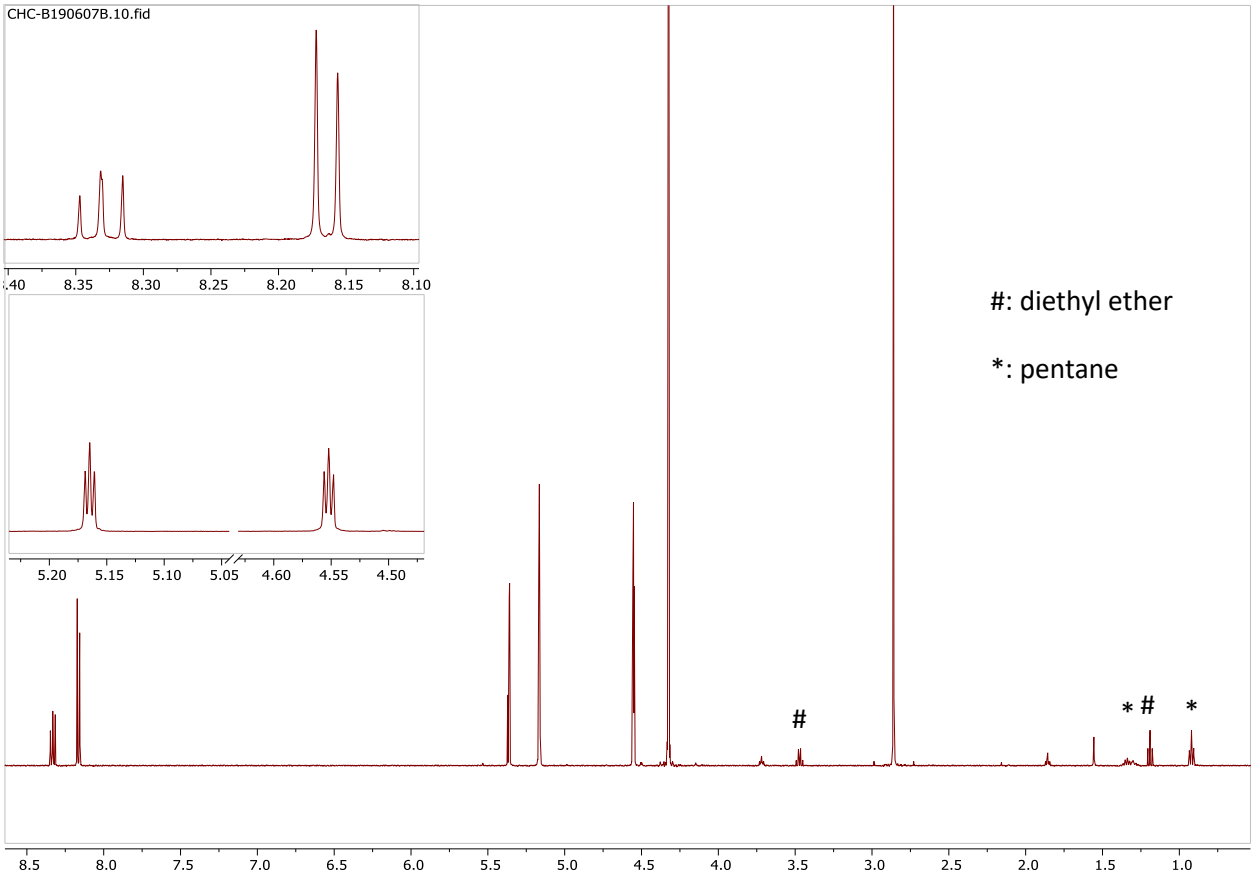

Figure A.3: 500 MHz ^{1}H NMR of $(Fc_2PDI)ZnCl_2$ in DCM

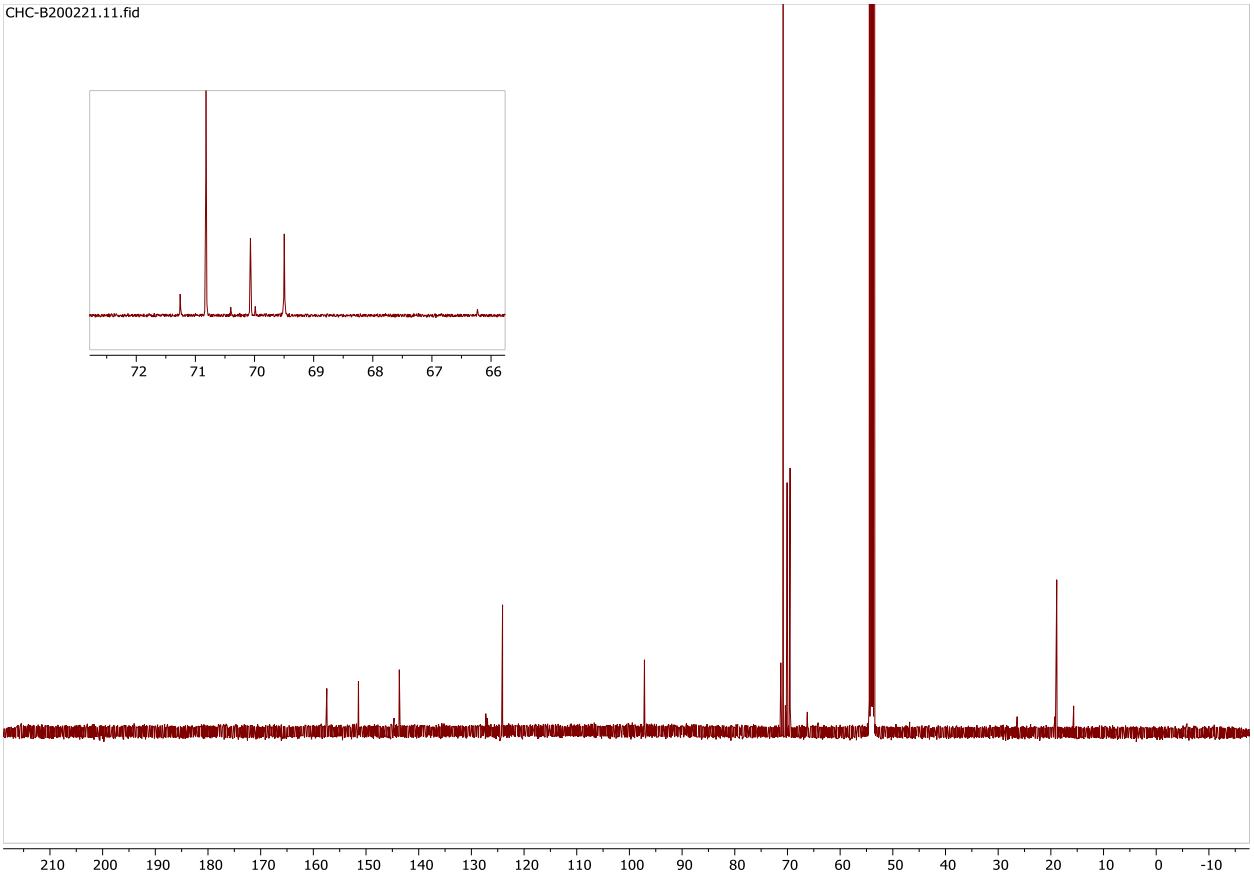

Figure A.4: 500 MHz ^{13}C NMR of $(Fc_2PDI)ZnCl_2$ in DCM

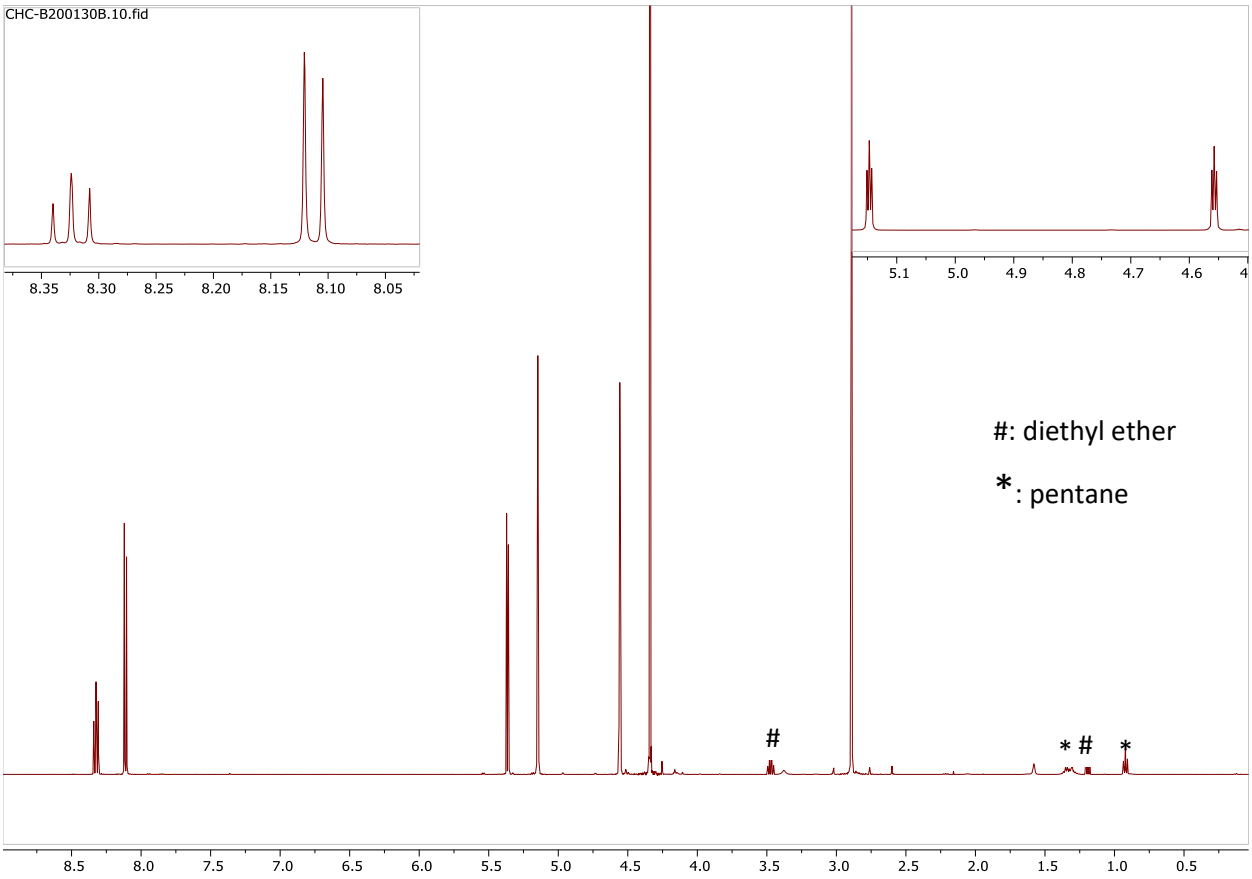

Figure A.5: 500 MHz ^{1}H spectrum of $(Fc_2PDI)MgCl_2$ in DCM

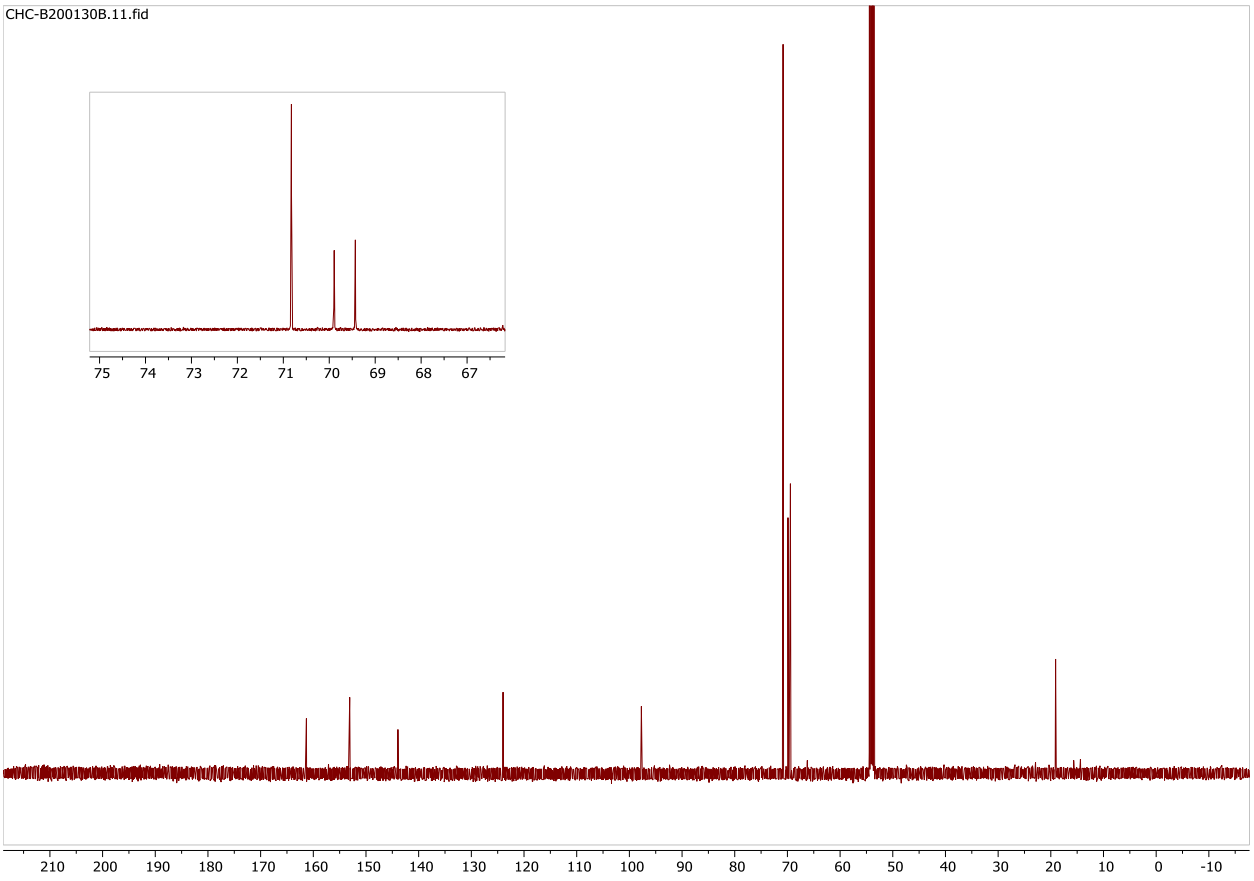

Figure A.6: 126 MHz ^{13}C NMR of $(Fc_2PDI)MgCl_2$ in DCM

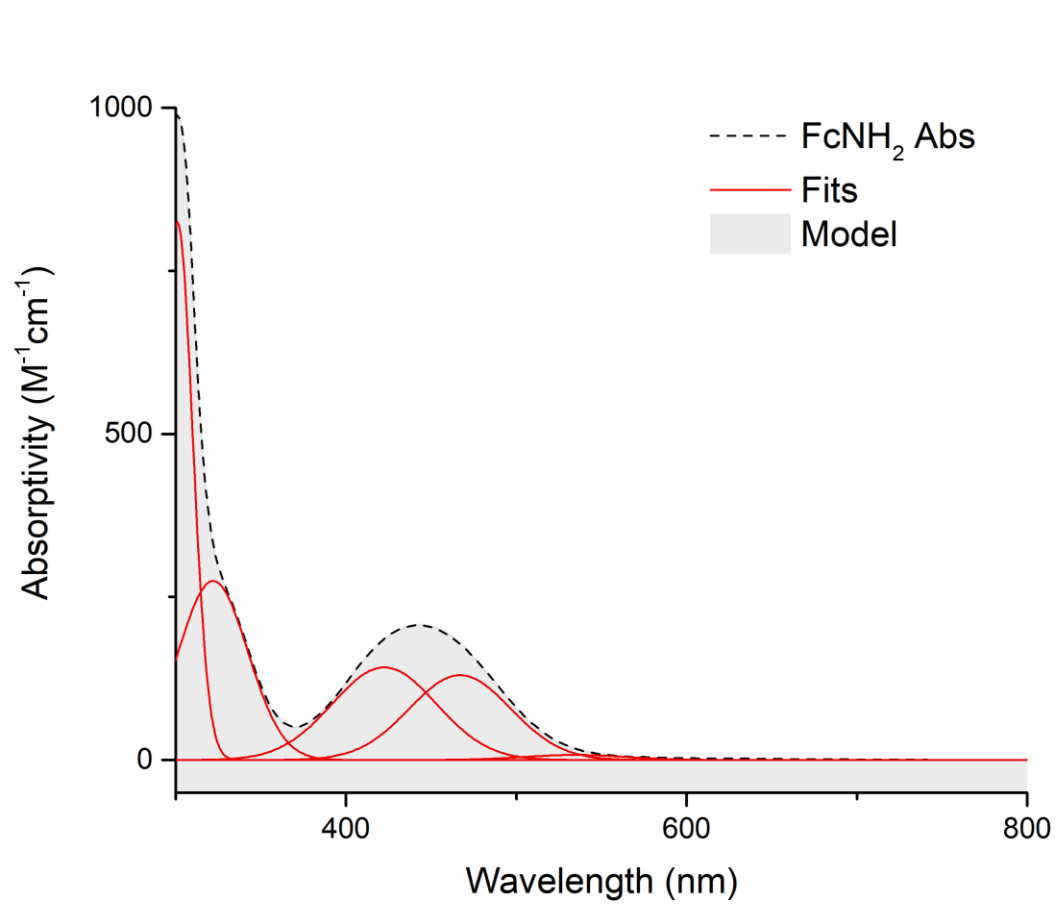

Figure A.7: Gaussian fitting of $FcNH_2$ absorption data taken in DCM

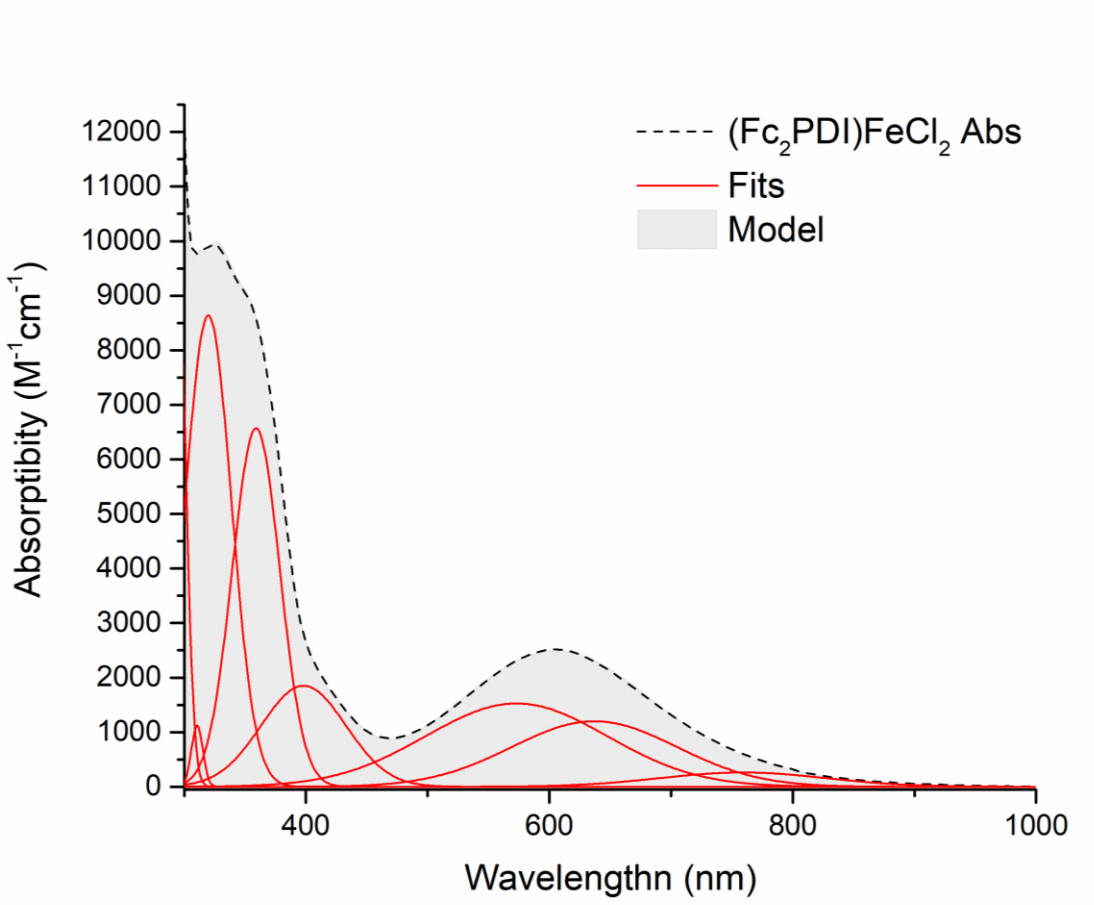

Figure A.8: Gaussian fitting of $(Fc_2PDI)ZnCl_2$ absorption data taken in DCM

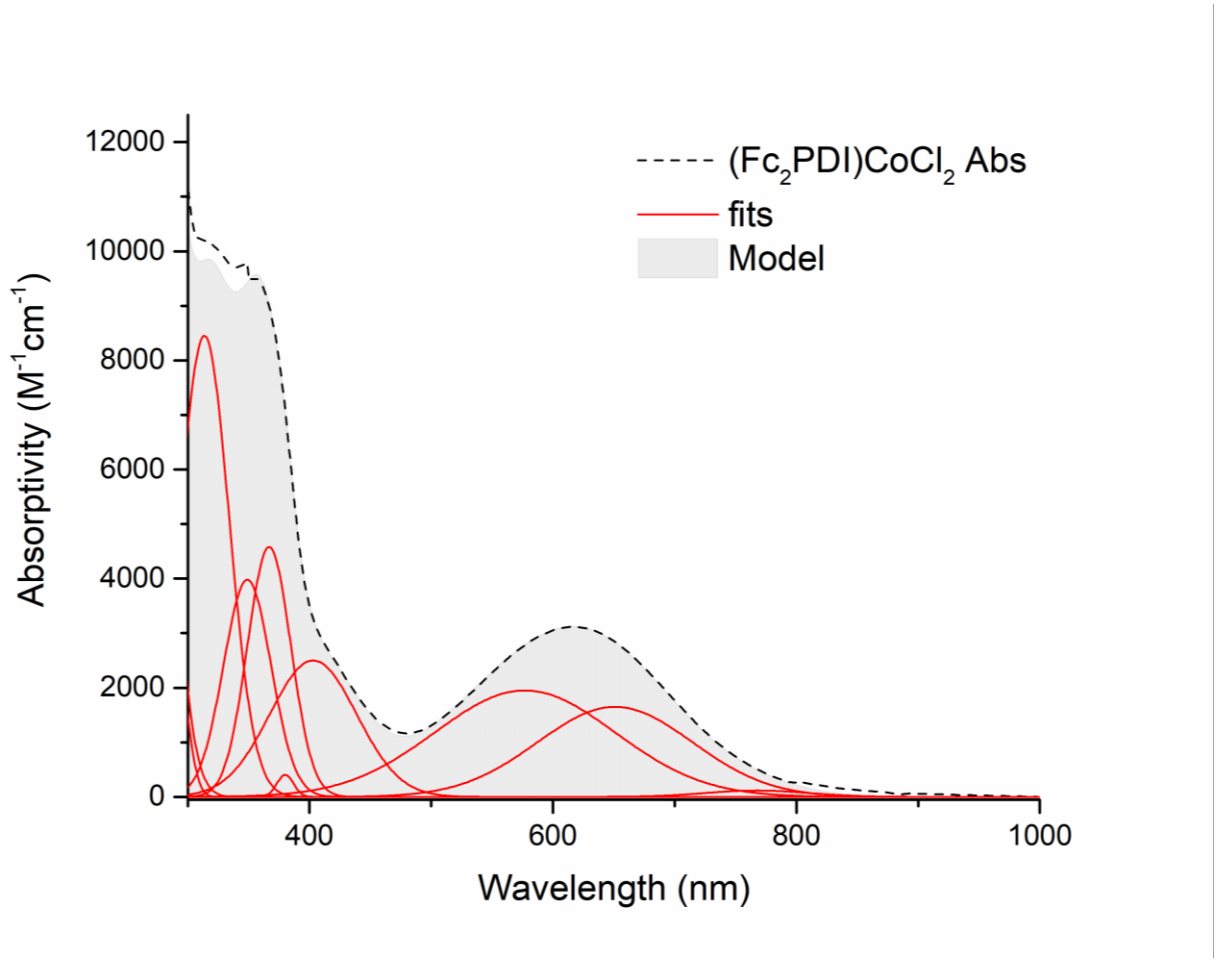

Figure A.9: Gaussian fitting of $(Fc_2PDI)CoCl_2$ absorption data taken in DCM

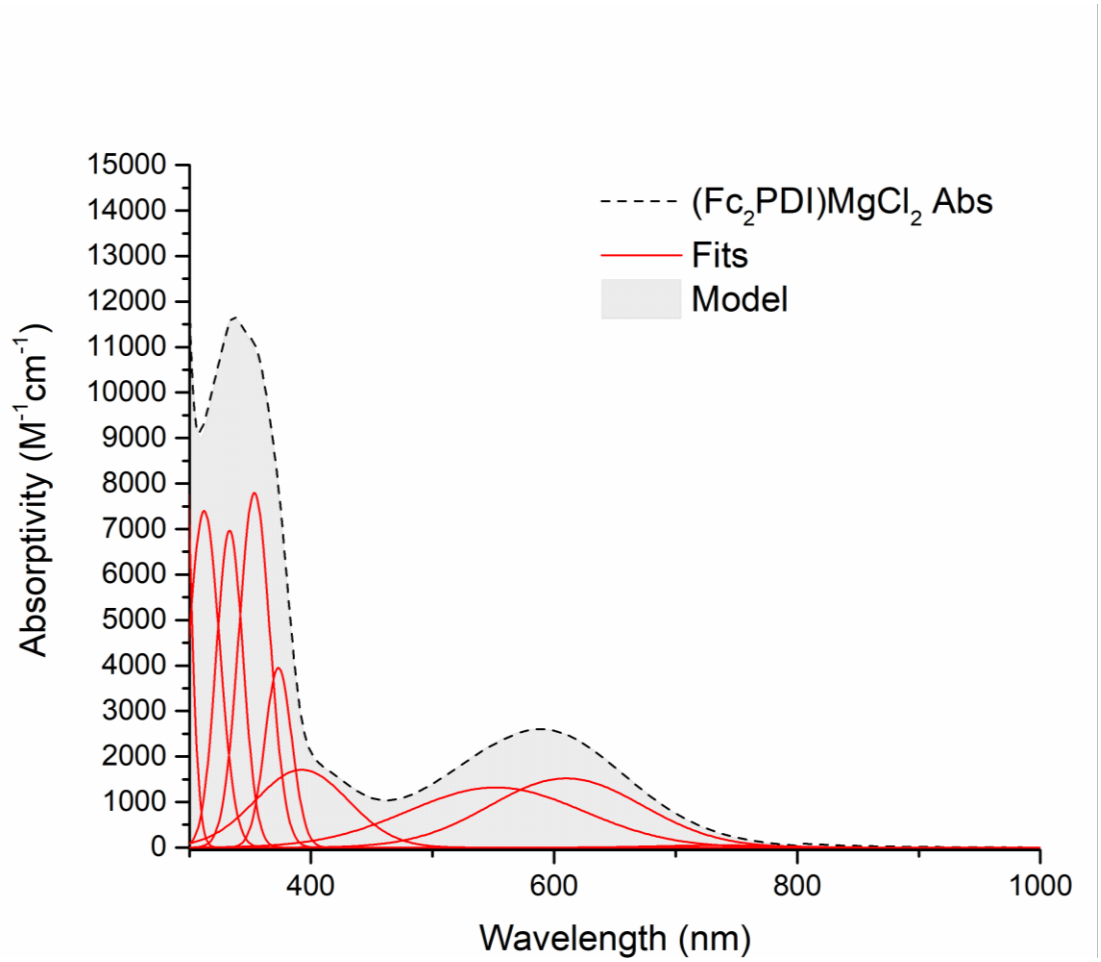

Figure A.10: Gaussian fitting of $(Fc_2PDI)MgCl_2$ absorption data taken in DCM

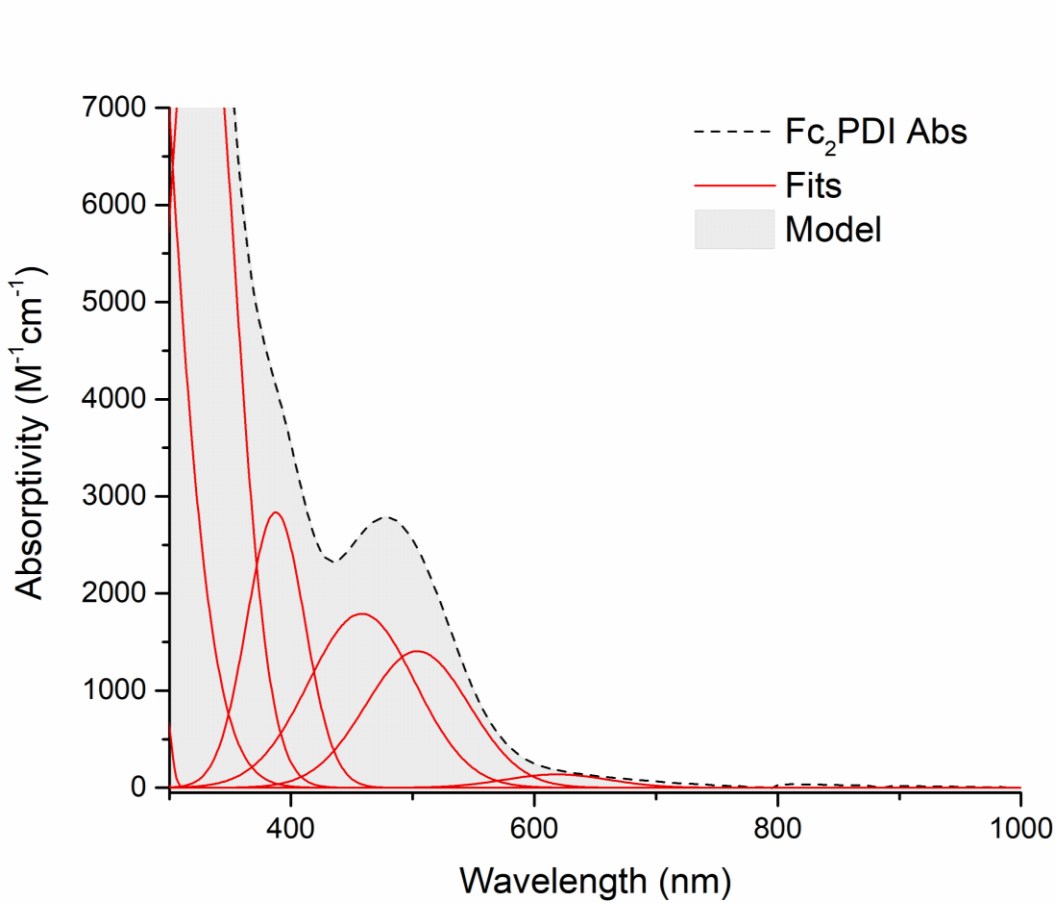

Figure A.11: Gaussian fitting of Fc_2PDI absorption data taken in DCM

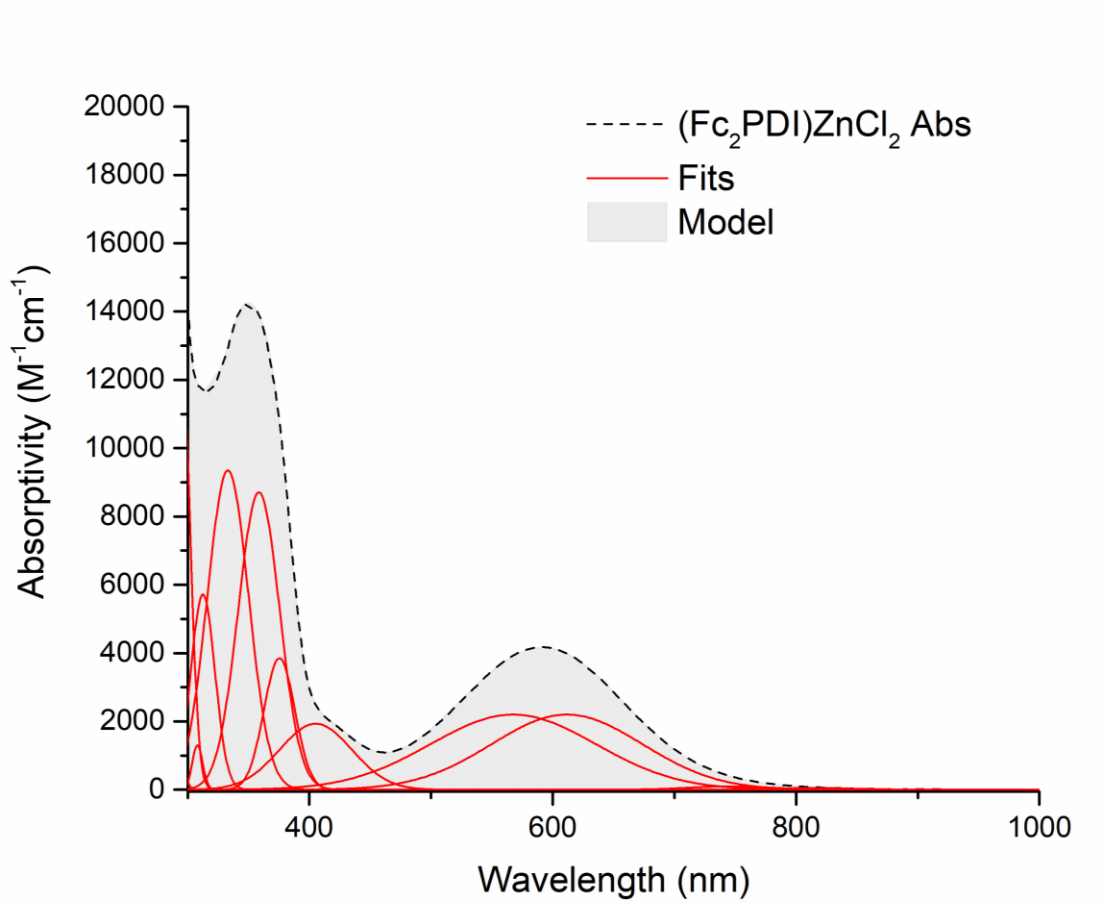

Figure A.12: Gaussian fitting of $(Fc_2PDI)FeCl_2$ absorption data taken in DCM

Calculated UV-vis bands for (Fc_2PDI)MCl_2 (M=Mg, Zn, Co, Fe) complexes

According to the DFT calculations, all four complexes have almost identical frontier orbitals in which the highest occupied molecular orbital (HOMO) is localized on the d orbitals of the two ferrocene substituents and the lowest unoccupied molecular orbital (LUMO) is mainly delocalized over the pyridine and imines groups. The calculated UV-vis spectra are in good agreement with the experimental values (Table A.2). The observed absorption of these complexes in the range of 600 nm is attributed, according to the calculations, to the HOMO → LUMO transition.

Table A.2

Experimental and calculated UV-vis bands.		
Complex	Experimental UV-vis bands (λ)	Calculated UV-vis bands (λ)
(Fc_2PDI)$MgCl_2$	590	618
(Fc_2PDI)$ZnCl_2$	590	615
(Fc_2PDI)$CoCl_2$	616	649
(Fc_2PDI)$FeCl_2$	605	703

Appendix B: supporting information to chapter 3

Table B.1. Crystal data and refinement details for $Fc_2PyrDIH$ (**1**), $[Fc_2PyrDI][BF_4]$ (**1^+**) $Fc_2PyrDISc(N(TMS)_2)_2$ (**2-Sc**)

	$Fc_2PyrDIH$ (1)	**$[Fc_2PyrDI][BF_4]$ (1^+)**	**$Fc_2PyrDISc(N(TMS)_2)_2$ (2-Sc)**
Empirical formula	$C_{47}H_{47}Fe_2N_2$	$C_{40}H_{36}BF_4Fe_2N_3$	$C_{59}H_{78}Fe_2N_5ScSi_4$
Formula weight	751.56	757.23	1126.28
Temperature / K	100.15	100.00(10)	99.98(13)
Crystal system	triclinic	triclinic	triclinic
Space group	P-1	P-1	P-1
a / Å,	5.8906(2)	11.6441(2)	14.8078(2)
, b / Å	14.1842(4)	13.3137(2)	15.7995(3)
c / Å	22.8531(7)	14.0026(2)	15.8874(3)
α/°,	83.392(2)	72.1520(10)	92.2286(13)
β/°,	86.260(2)	70.2060(10)	115.7948(15)
γ/°	78.882(2)	68.7900(10)	116.0183(15)
Volume / $Å^3$	1859.36(10)	1861.80(5)	2883.60(9)
Z	2	2	2
ρ_{calc} / mg mm^{-3}	1.342	1.351	1.297
μ / mm^{-1}	0.816	0.831	6.076
F(000)	790.0	780.0	1192
Radiation	MoKα (λ = 0.71073)	Mo Kα (λ = 0.71073)	Mo Kα (λ = 0.71073)
2Θ range for data collection	4.398 to 67.55	4.1 to 82.44	6.444 to 157.338°
Index ranges	$-8 \le h \le 9$, $-21 \le k \le 20$, $-34 \le l \le 34$	$-21 \le h \le 21$, $-24 \le k \le 24$, $-25 \le l \le 25$	$-18 \le h \le 17$, $-20 \le k \le 19$, $-20 \le l \le 20$
Reflections collected	35451	129841	57152
Independent reflections	12744 [R_{int} = 0.0702, R_{sigma} = 0.0982]	24210 [R_{int} = 0.0529, R_{sigma} = 0.0429]	11942[R(int) = 0.0357]
Data/restraints/parameters	12744/0/463	24210/0/454	11942/379/720
Goodness-of-fit on F^2	1.072	1.069	1.024
Final R indexes [I>2σ(I)]	R_1 = 0.0916, wR_2 = 0.1971	R_1 = 0.0784, wR_2 = 0.2563	R_1 = 0.0341, wR_2 = 0.0921
Final R indexes [all data]	R_1 = 0.1413, wR_2 = 0.2179	R_1 = 0.0977, wR_2 = 0.2764	R_1 = 0.0360, wR_2 = 0.0933
Largest diff. peak/hole / e $Å^{-3}$	1.37/-0.88	7.75/-0.61	0.830/-0.421

Table B.2. Crystal data and refinement details for $(Fc_2PyrDI)_2Y(N(TMS)_2)$ (**3-Y)** $(Fc_2PyrDI)_3La$ (**4-La**)

	$(Fc_2PyrDI)_2YN(TMS)$ (3-Y)	**$(Fc_2PyrDI)_3La$ (4-La)**
Empirical formula	$C_{91}H_{98}Fe_4N_7Si_2Y$	$C_{60}Fe_3La_{0.5}N_{4.5}$
Formula weight	1658.25	1020.78
Temperature/K	100.00(10)	100.00(10)
Crystal system	triclinic	monoclinic
Space group	P-1	C2
a/Å	13.9283(2)	22.4858(6)
b/Å	17.1030(2)	19.0960(3)
c/Å	17.7214(3)	25.9621(6)
α/°	105.2180(10)	90
β/°	104.1650(10)	112.586(3)
γ/°	92.8370(10)	90
Volume/Å^3	3920.34(10)	10292.8(4)
Z	2	8
ρ_{calc}g/cm^3	1.405	1.317
μ/mm^{-1}	1.537	1.278
F(000)	1728.0	3985.0
Radiation	Mo Kα (λ = 0.71073)	MoKα (λ = 0.71073)
2Θ range for data collection/°	3.972 to 67.71	4.266 to 68.034
Index ranges	$-21 \le h \le 20$, $-26 \le k \le 25$, $-26 \le l \le 27$	$-35 \le h \le 35$, $-29 \le k \le 29$, $-37 \le l \le 39$
Reflections collected	250476	111507
Independent reflections	28996 [R_{int} = 0.0623, R_{sigma} = 0.0472]	36051 [R_{int} = 0.0560, R_{sigma} = 0.0683]
Data/restraints/parameters	28996/0/958	36051/1/546
Goodness-of-fit on F^2	1.264	2.285
Final R indexes [I>=2σ (I)]	R_1 = 0.0774, wR_2 = 0.1596	R_1 = 0.2108, wR_2 = 0.5203
Final R indexes [all data]	R_1 = 0.0953, wR_2 = 0.1643	R_1 = 0.2544, wR_2 = 0.5594
Largest diff. peak/hole / e Å^{-3}	1.37/-0.99	17.03/-7.96
Flack parameter	-	0.489(8)

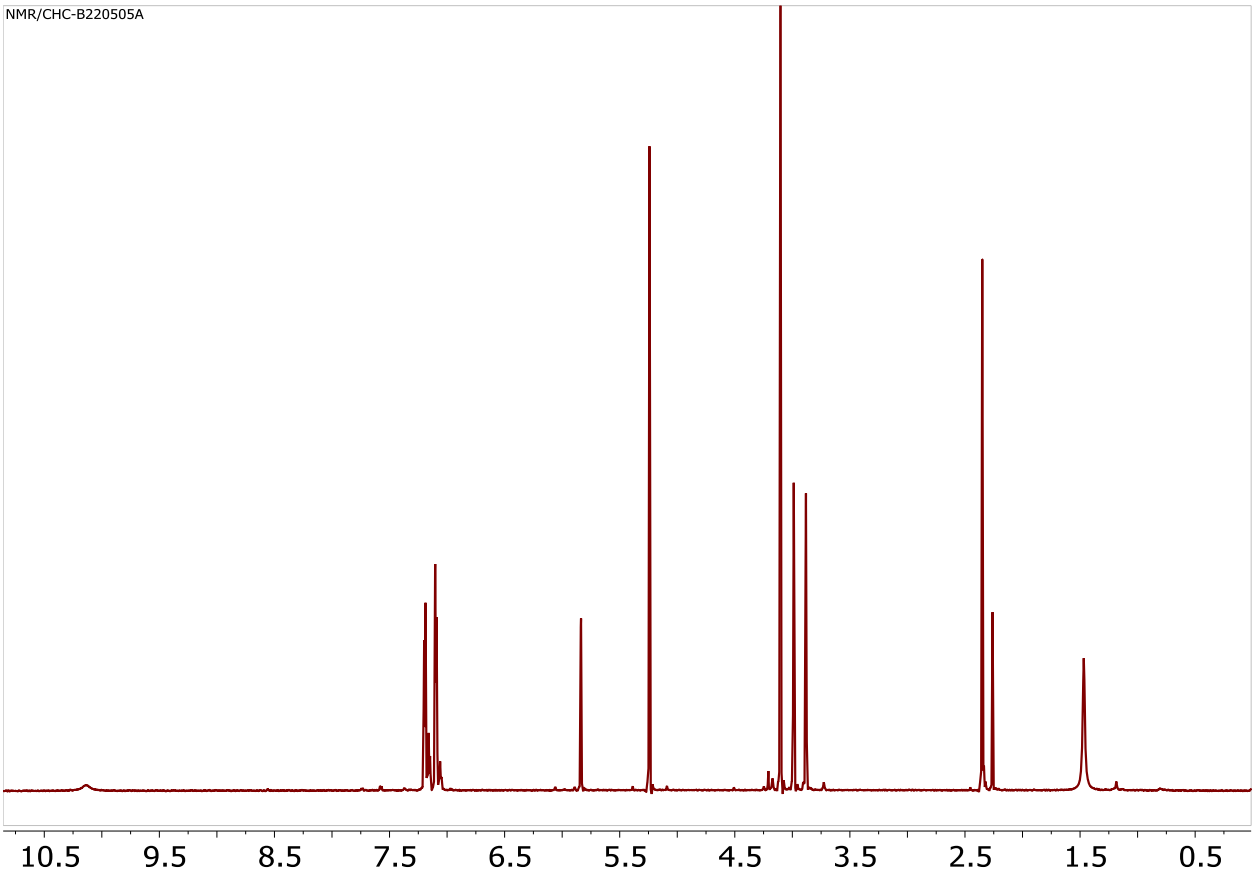

Figure B.1: 500 MHz ^{1}H NMR spectrum of $Fc_2PyrDIH$ (**1**) in C_6D_6

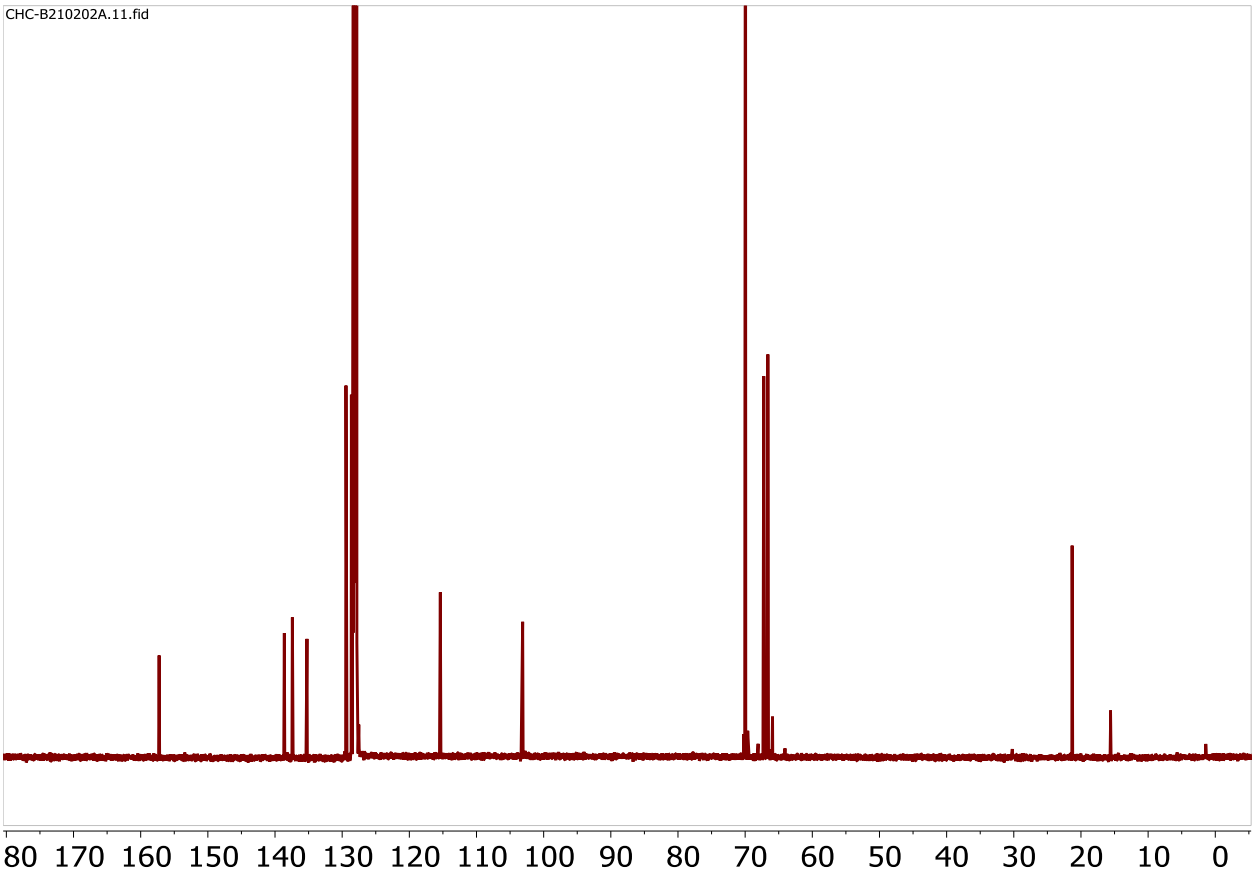

Figure B.2: 126 MHz ^{13}C NMR spectrum of $Fc_2PyrDIH$ (**1**) in C_6D_6

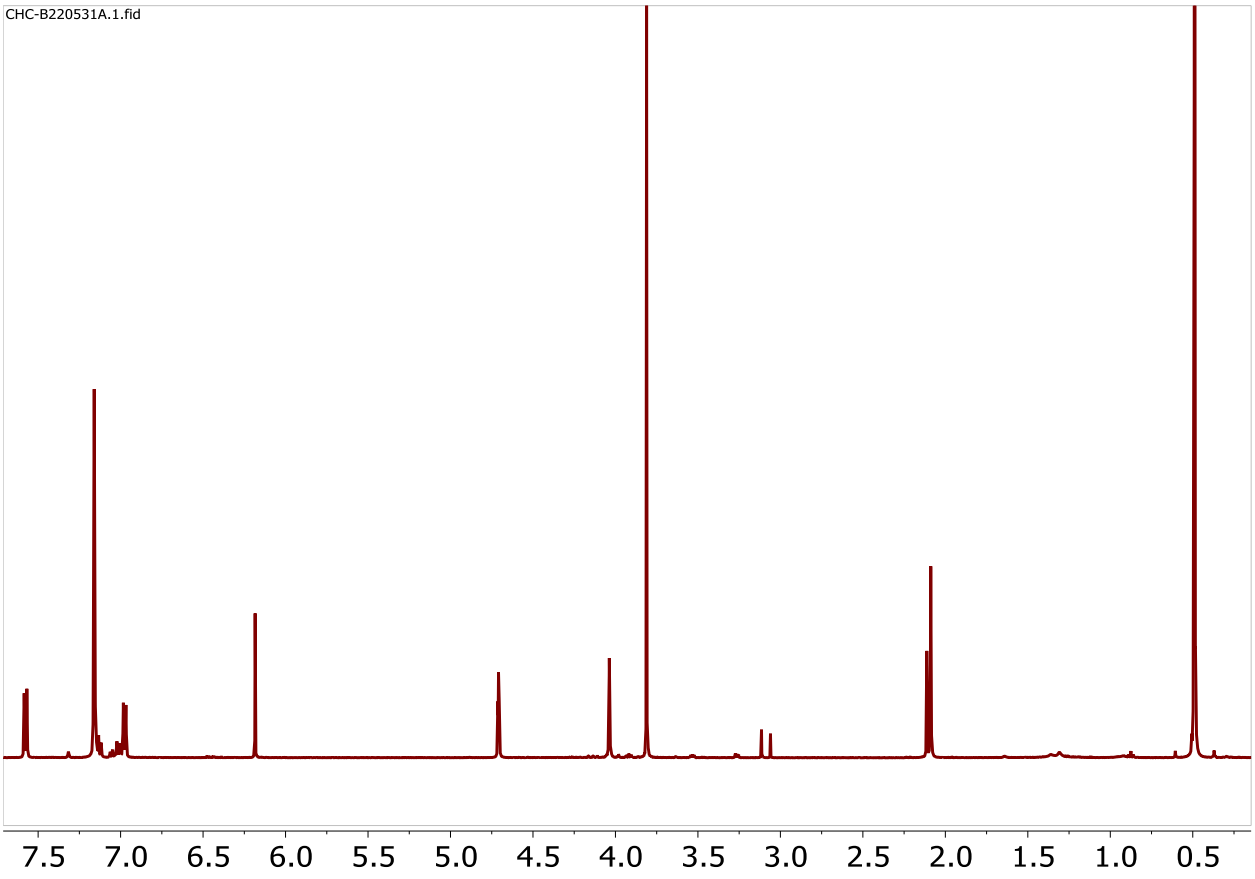

Figure B.3: 500 MHz ^{1}H NMR spectrum of $(Fc_2PyrDI)Sc(N(TMS)_2)_2$ (**2-Sc**) in C_6D_6

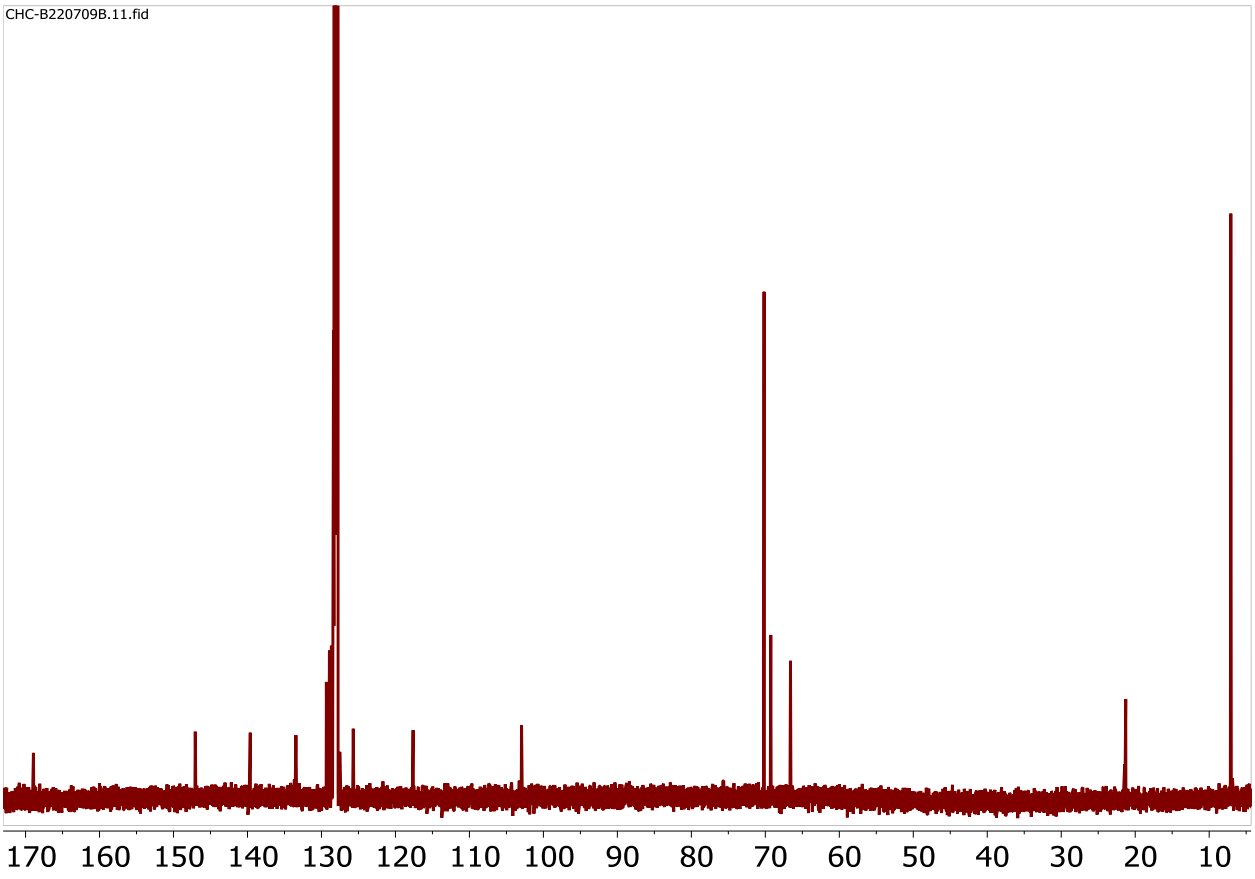

Figure B.4: 126 MHz ^{13}C NMR spectrum of $(Fc_2PyrD)Sc(N(TMS)_2)_2$ (**2-Sc**) in C_6D_6

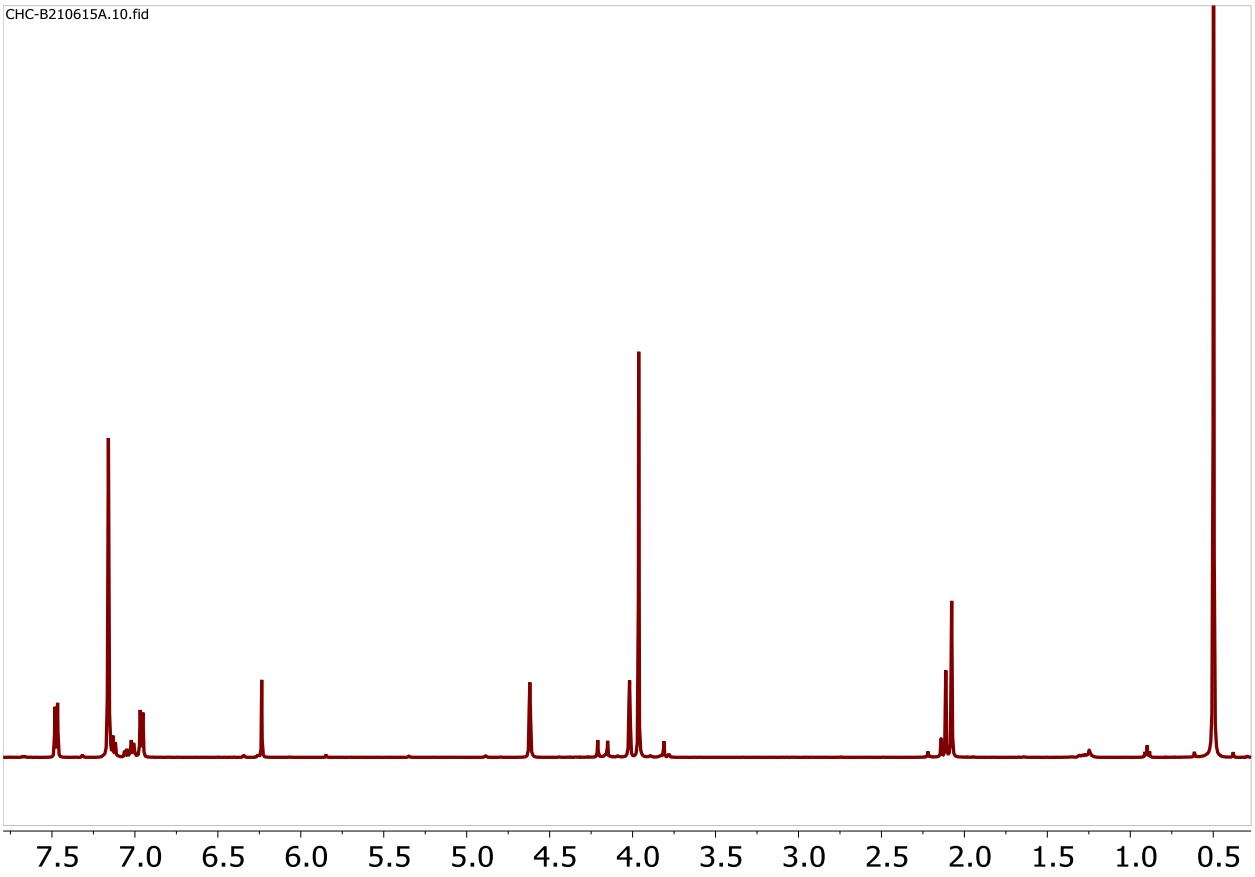

Figure B.5: 500 MHz ^{1}H NMR spectrum of $(Fc_2PyrDI)Y(N(TMS)_2)_2$ (**2-Y**) in C_6D_6

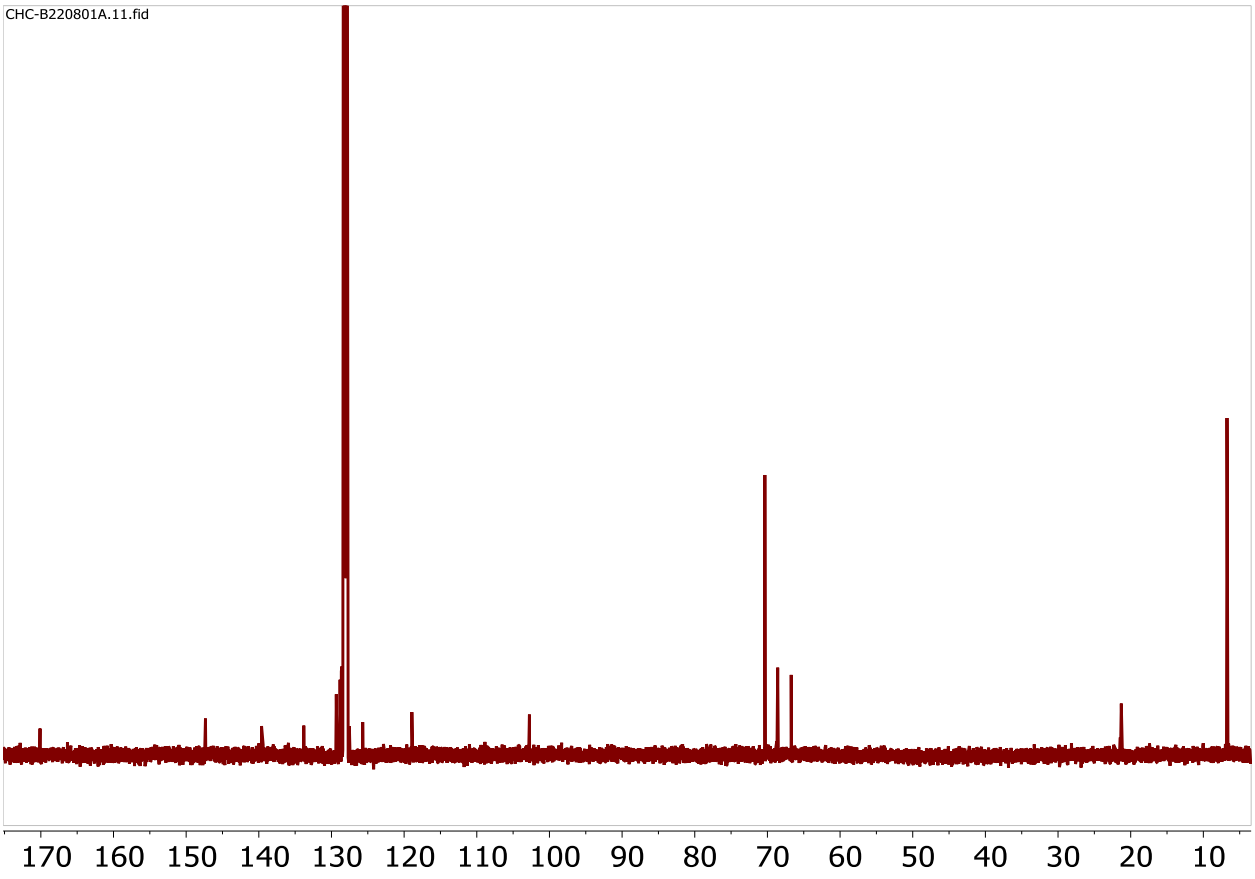

Figures B.6: 126 MHz ^{13}C NMR spectrum of $(Fc_2PyrDI)Y(N(TMS)_2)_2$ (**2-Y**) in C_6D_6

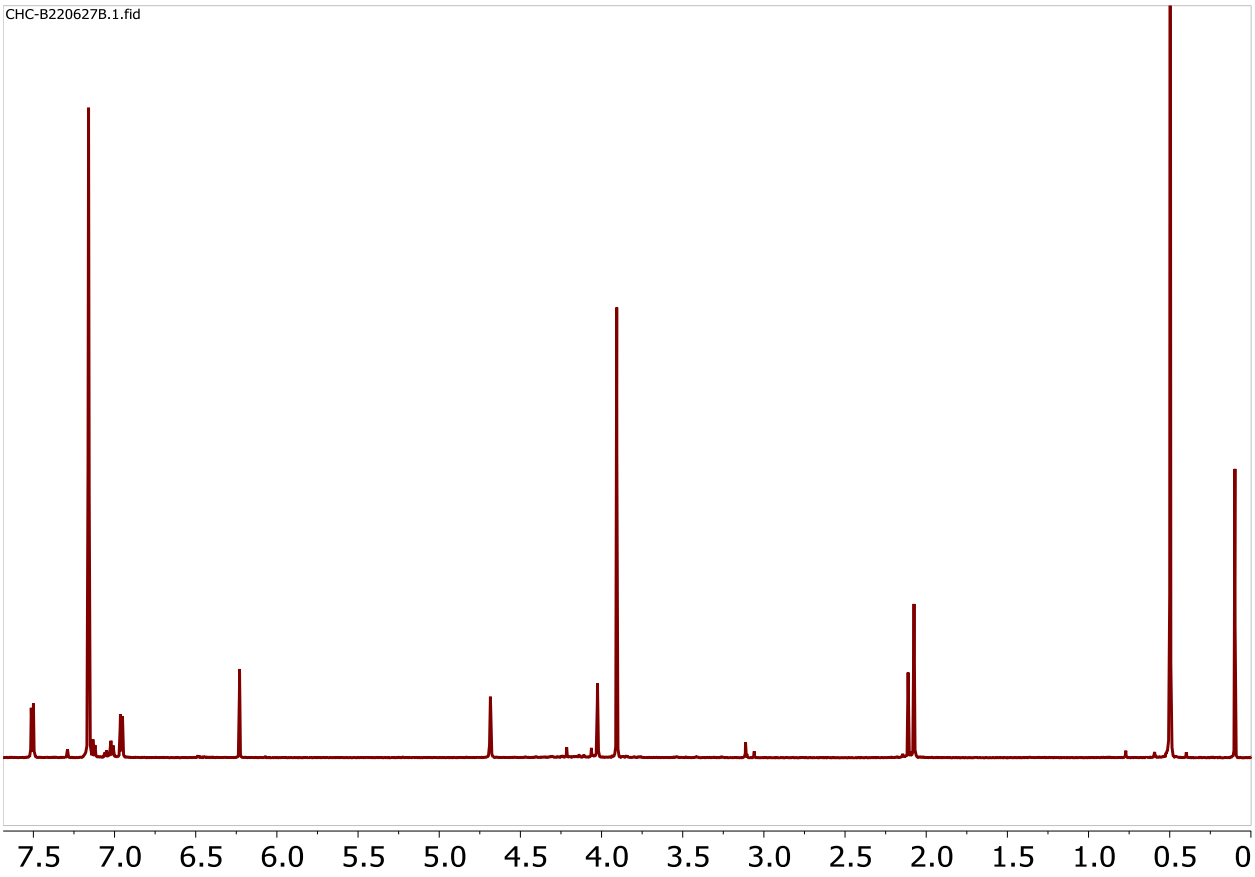

Figure B.7: 500 MHz ^{1}H NMR spectrum of $(Fc_2PyrDI)Lu(N(TMS)_2)_2$ (**2-Lu**) in C_6D_6

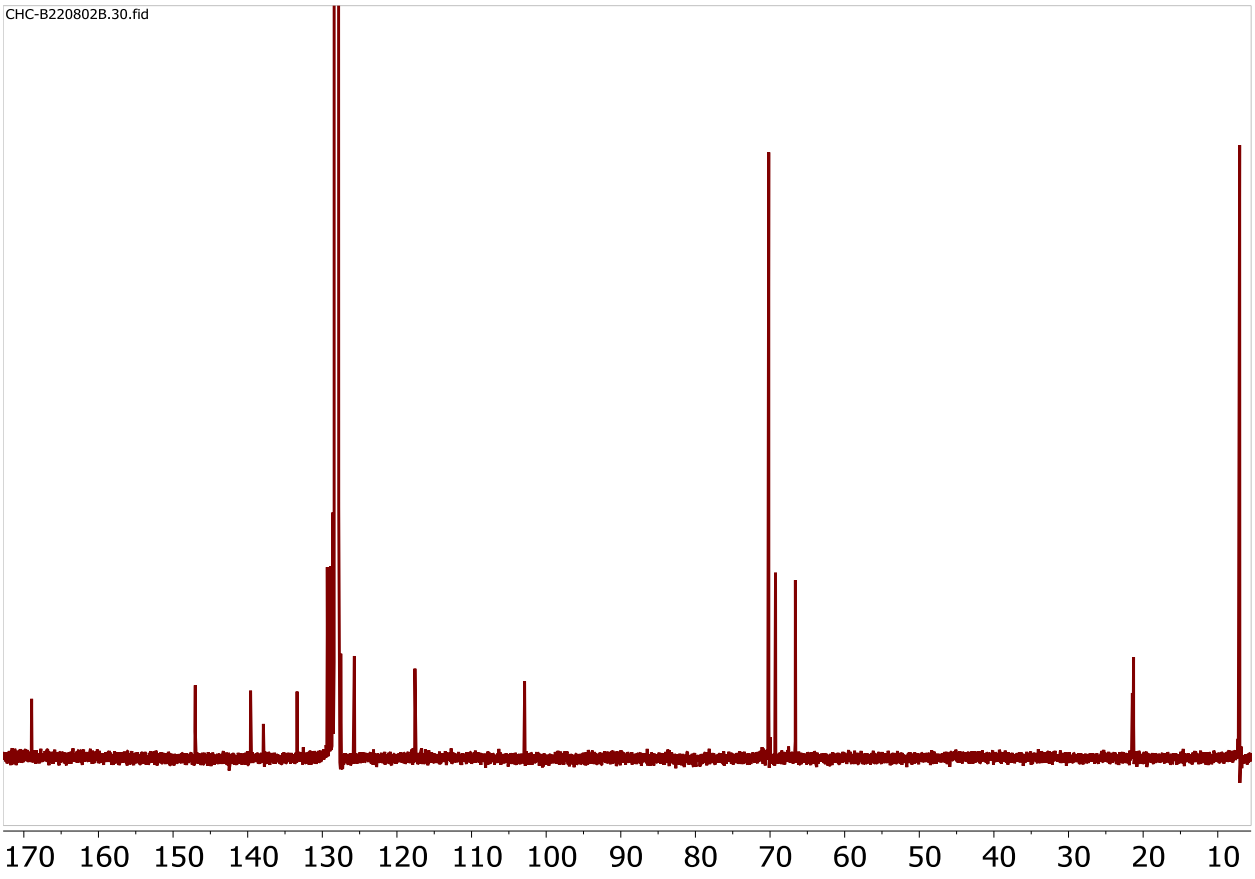

Figure B.8: 126 MHz ^{13}C NMR spectrum of $(Fc_2PyrDI)Lu(N(TMS)_2)_2$ (**2-Lu**), taken in C_6D_6

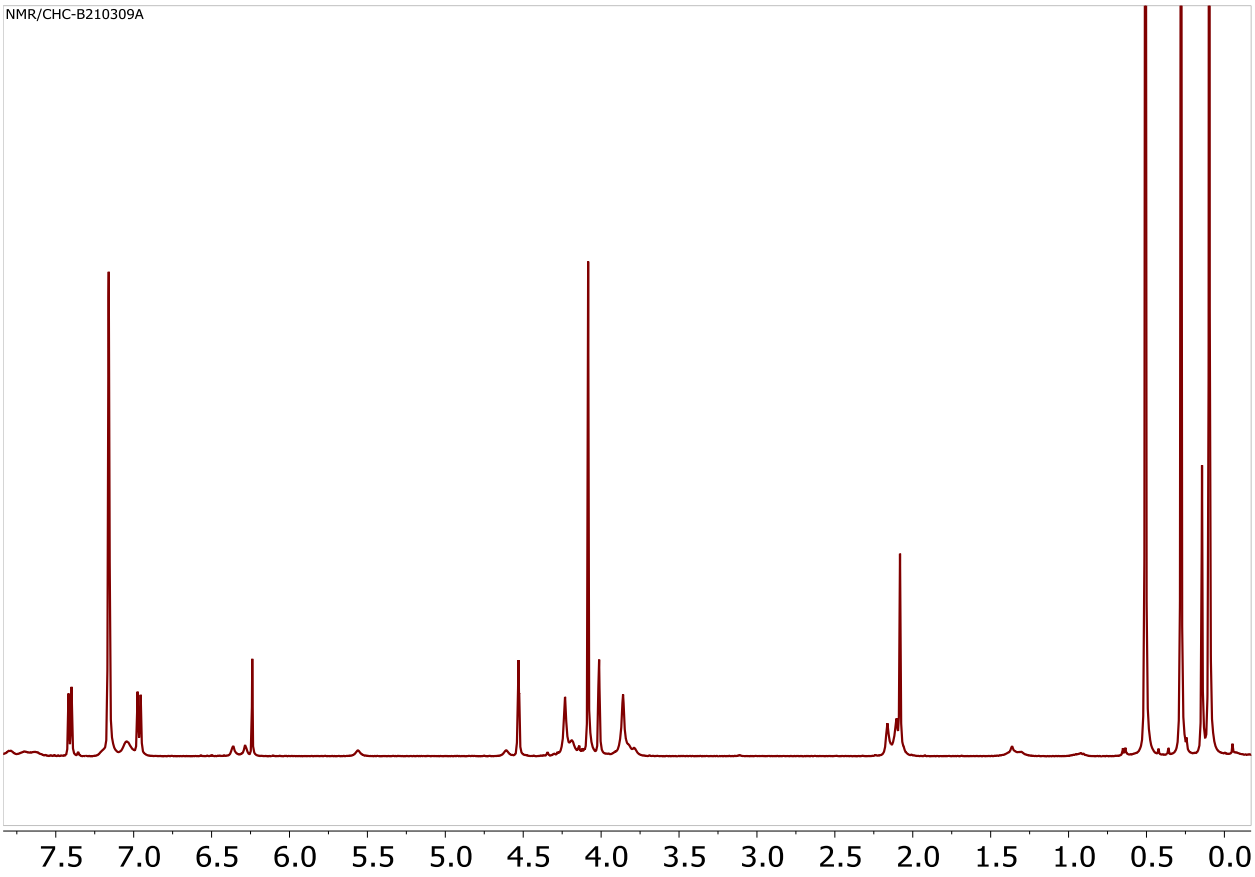

Figure B.9: 500 MHz ^{1}H NMR spectrum of in situ formation of $(Fc_2PyrDI)La(N(TMS)_2)_2$ (**2-La**) in C_6D_6

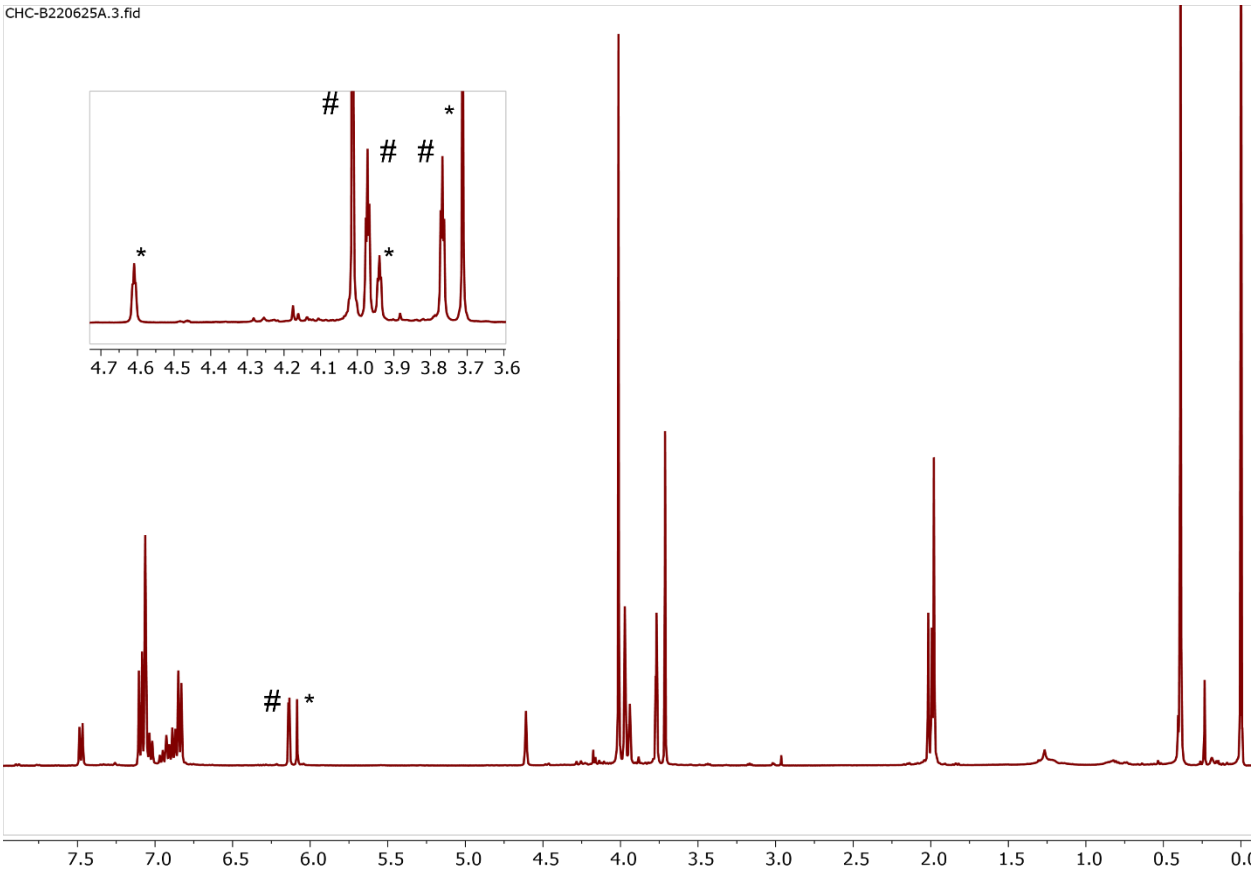

Figure B.10: Attempted NMR scale synthesis of **3-Sc** by reacting excess **1** with $Sc(N(TMS)_2)_3$. Stars represent **2-Sc** signals, while hashes show unreacted **1** signals. Negligible **3-Sc** is formed. Spectrum is taken at 500 MHz in C_6D_6 after heating overnight at 70 °C.

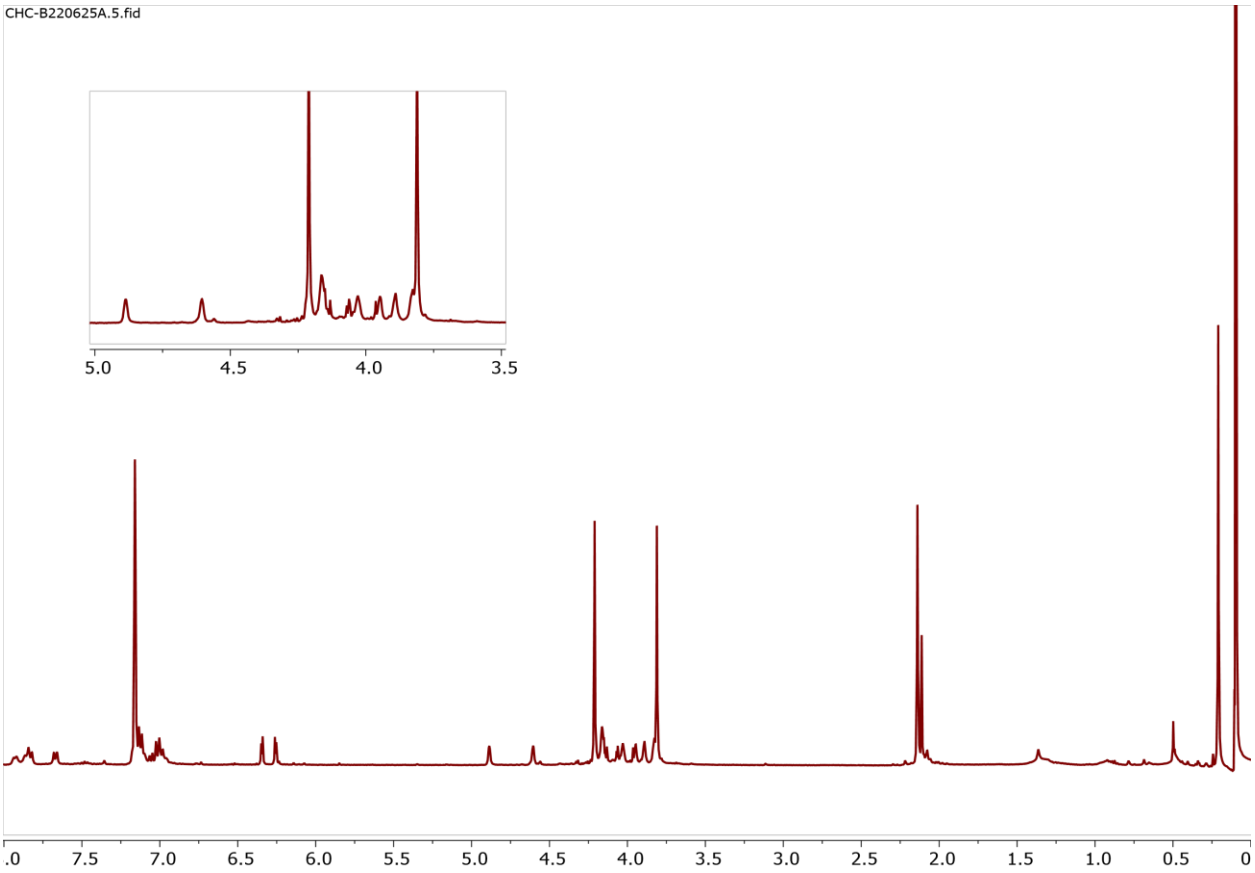

Figure B.11: NMR scale reaction of two equiv of **1** with $Y[N(TMS)_2]_3$ to produce **3-Y**. Remaining **2-Y** is negligible. On the basis of NOESY experiments (**Figure B.12**), resonances at 4.89, 4.60, 4.15, 3.94 ppm, belong to the same molecule, and both 4.20 and 3.81 belong to the same molecule, leading to the expected 6 peaks (3 per Fc_2PyrDI unit) The relative inegrations are 1:5, suggesting they are CH and C_5H_5 signals from Cp rings arising from the same molecule. Spectrum was taken at 500 MHz in C_6D_6 after heating overnight at 70 °C.

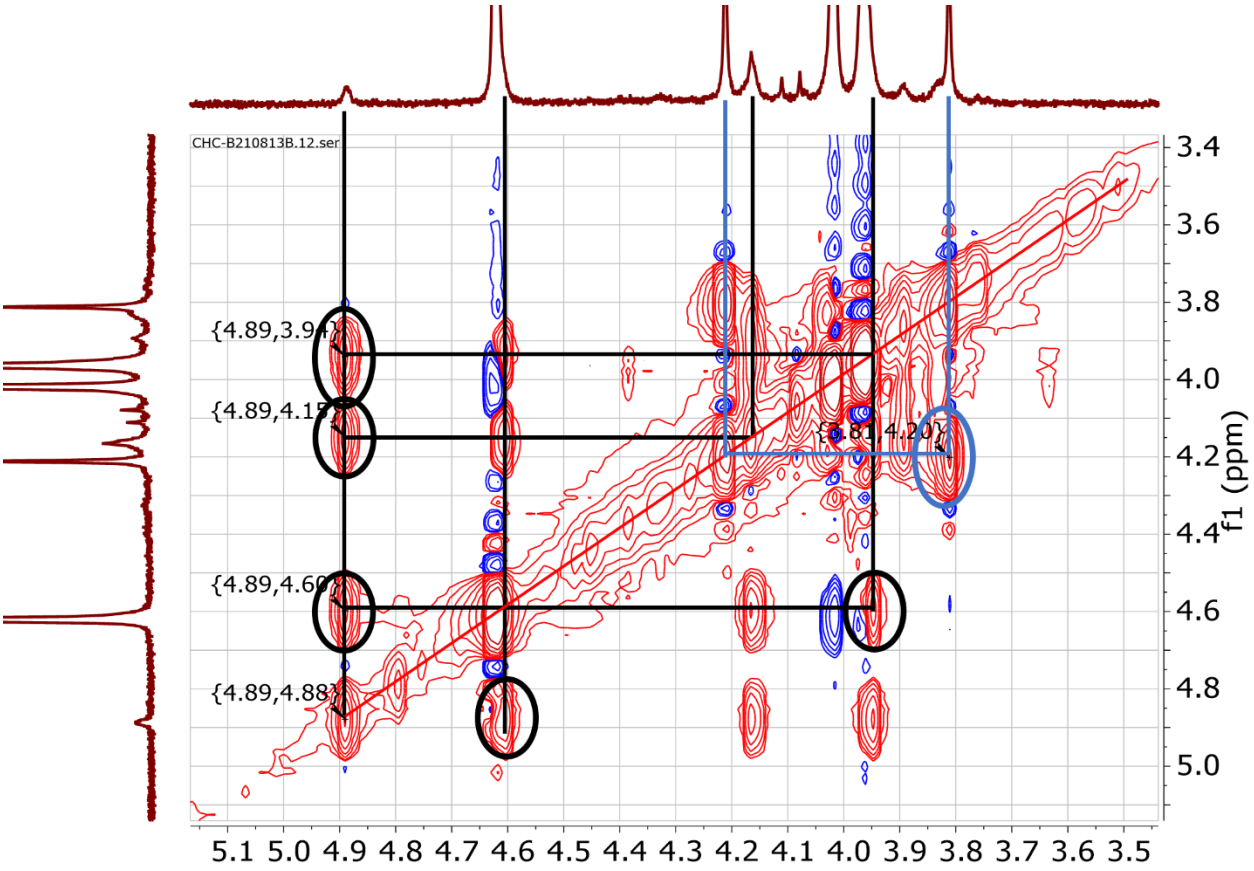

Figure B.12: ^{1}H NOESY spectrum of a sample of isolated **2-Y**, zooming in on the ferrocenyl region. Signals marked with circles represent proposed **3-Y** signals. Black indicates 4 CH Cp signals, and blue represents 2 C_5H_5 signals (consistent with 2 Fc_2PyrDI units in the complex). There is significant signal overlap with between preposed **3-Y** and **2-Y** signals. For this reason lines are drawn to guide the eye to show these correlations do not wholly overlap

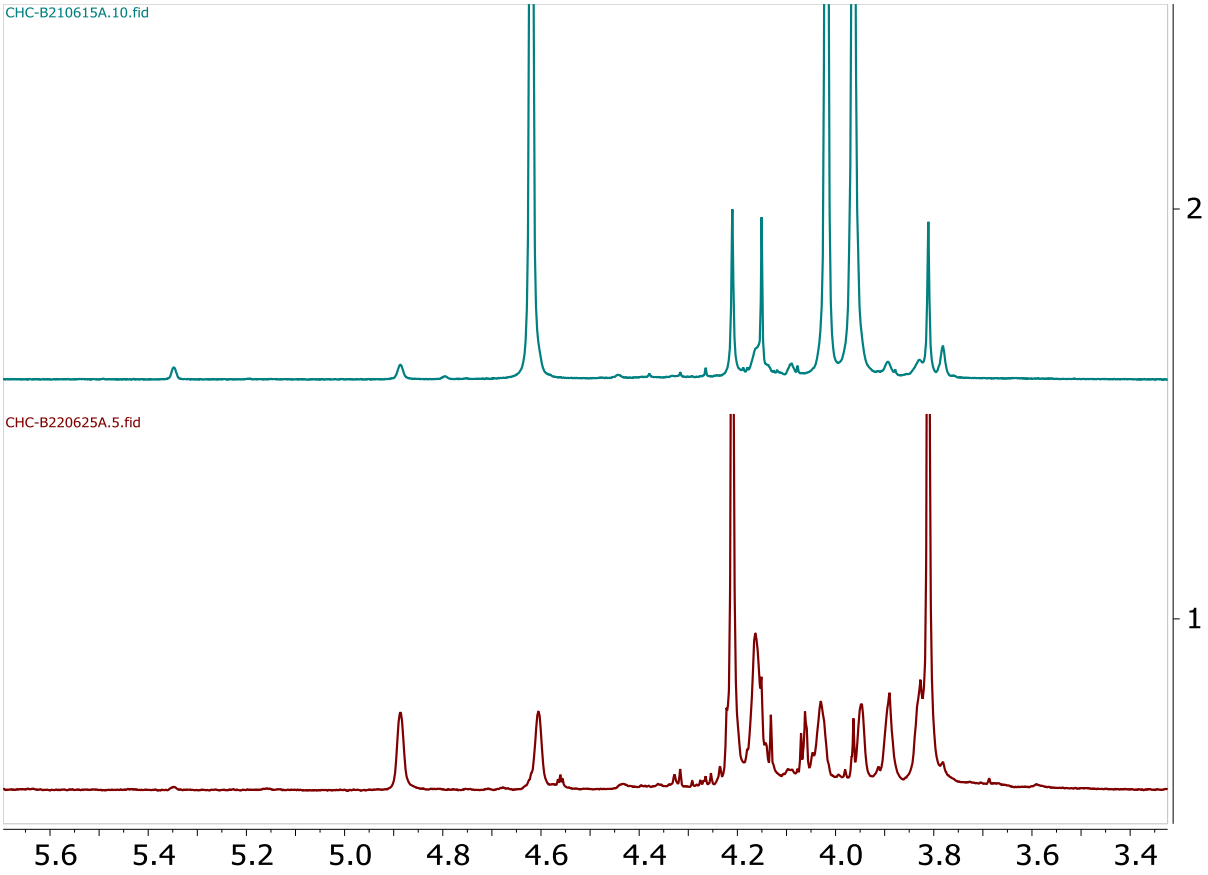

Figure B.13. Stacked comparison of 500 MHz ^{1}H NMR spectra of isolated **2-Y** (top) and the result of the NMR scale reaction showed in **Figure B.7** (bottom), zoomed in on the ferrocenyl region. Note that the bottom spectrum shows major resonances in the same positions as minor resonances in the top spectrum. We believe 6 of the 8 observed main resonances belong to **3-Y** (4 CH signals and 2 C_5H_5 signals; relative integrations are 1:5), and the remaining 2 are C_5H_5 signals from small amounts of **4-Y**. Resonances for the supporting **3-Y** as the main extra species after isolation. **3-Y** integrates to 5-10% compared to **2-Y** in the top spectrum.

Table B.3. Computed and experimental electronic transitions

Complex	Computed transitions (nm/cm^{-1})	Experimental transitions (nm/cm^{-1})
1	535/18740	497/20080
1^{+}	594/16870	616/16234
2-Sc	575/17521	566/17637
2-Sc^{+}	819/10798	878/11337
2-Lu	571/17508	565/17699
2-Lu^{+}	845/11839 1400/7192	Broad from 850 – 2000 nm. (See **Figure 5**)
2-Y	568/17589	557/17921
2-Y^{+}	1400/7144 855/11694	Broad from 900 – 2000 (see **Figure 5**)

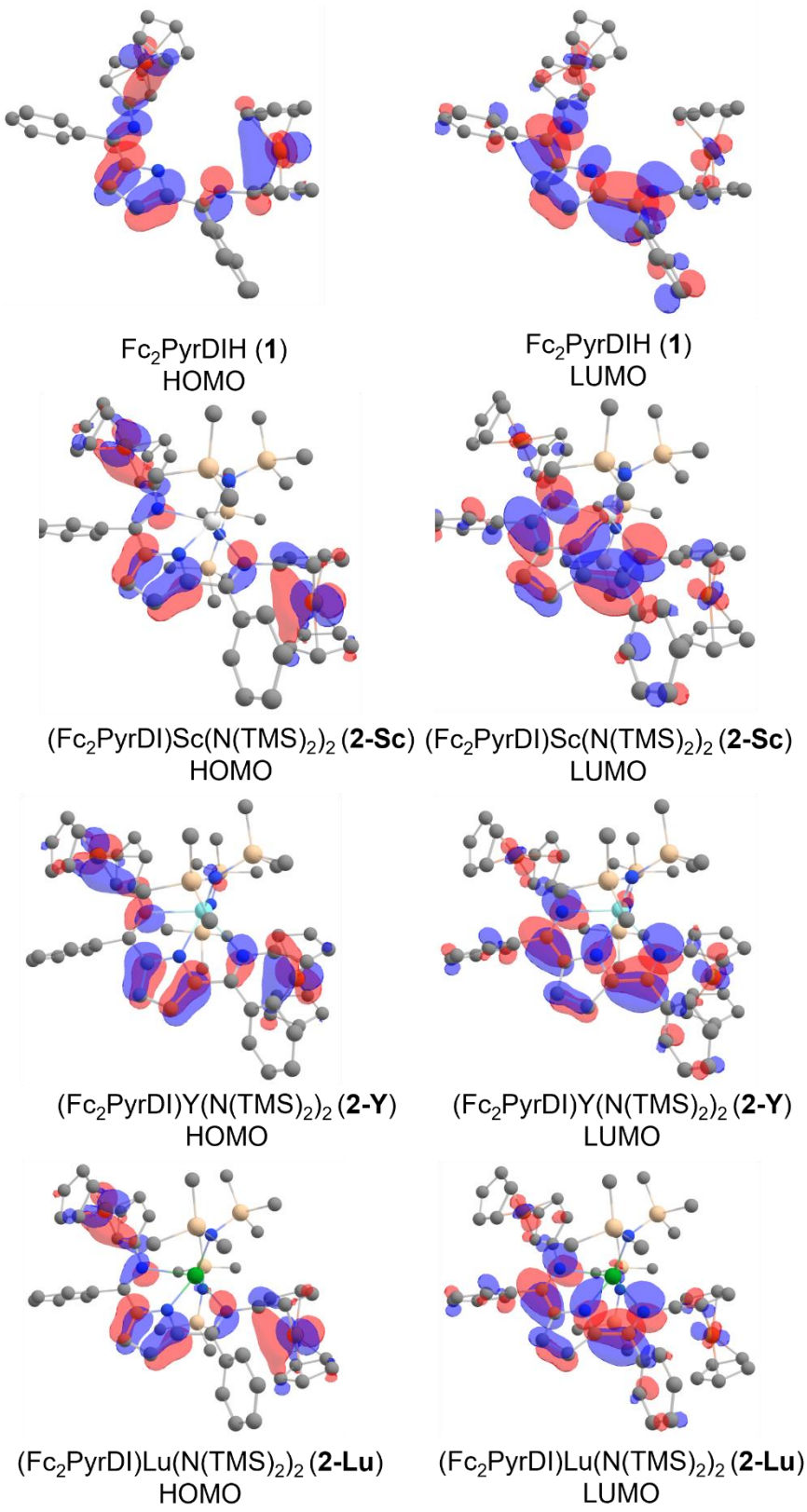

Figure B.14: Computed HOMOs and LUMOs for compounds **1**, **2-Sc**, **2-Y**, and **2-Lu**

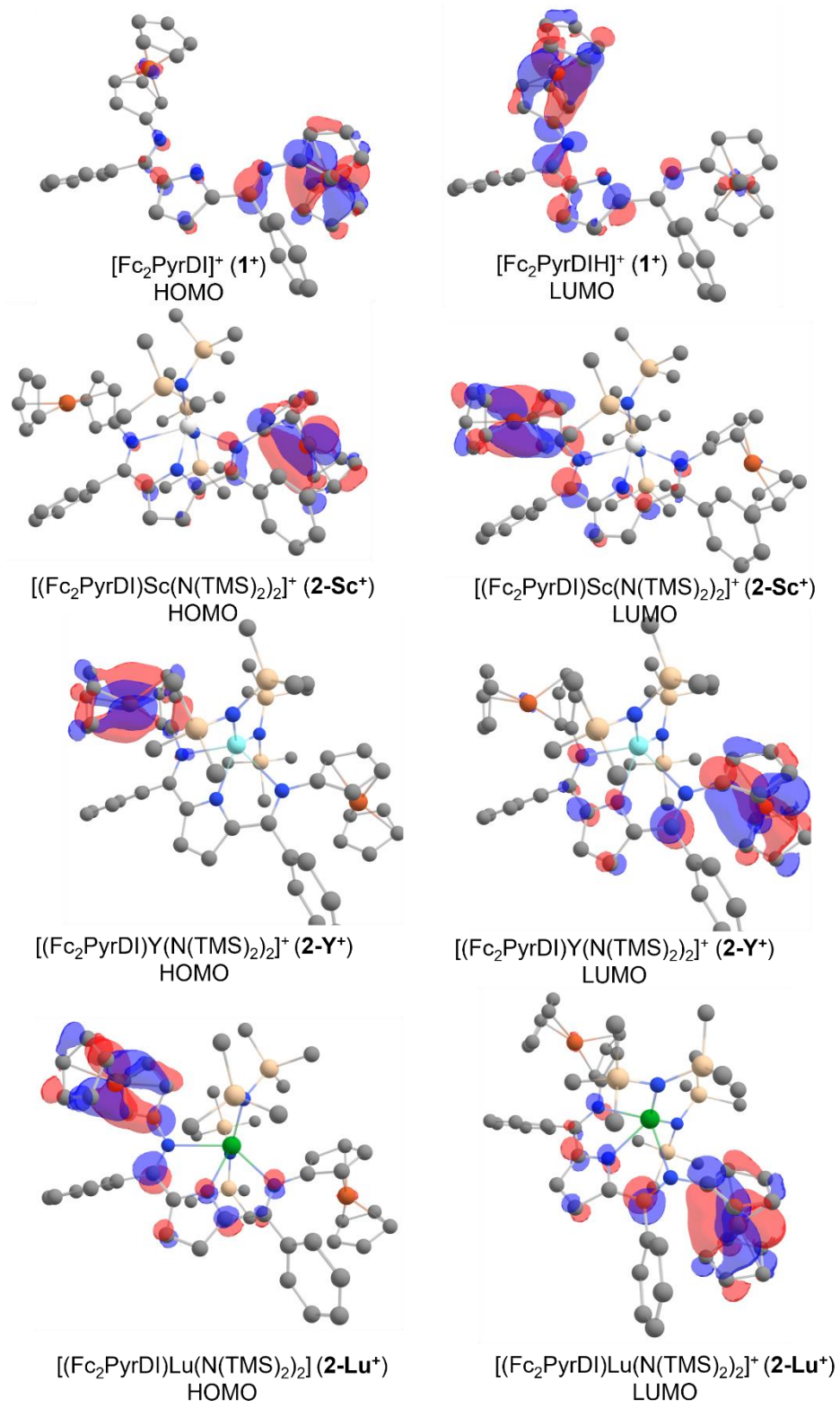

Figure B.15: Computed HOMOs and LUMOs for compounds **1**$^{+}$, **2-Sc**$^{+}$, **2-Y**$^{+}$, and **2-Lu**$^{+}$

CURRICULUM VITAE

SKILLS

- Solution and analysis of crystal structures
- Design and synthesis of (in)organic molecules
- Structural/electronic characterization techniques
- Extensive skill in Schlenk and high-vacuum work
- Efficient and rigorous literature searching
- Advanced 2D NMR experience
- Running and interpreting DFT calculations
- Repair of vacuum pumps and gloveboxes
- Strong written and verbal communication
- Analysis and communication of safety hazards

EDUCATION & HONORS

***Current*:** **NORTHWESTERN UNIVERISTY** - Weinberg College of Arts and Sciences▪ Evanston, IL

Ph.D. in Inorganic Chemistry: Marks Lab (GPA: 3.81)

Past: **UNIVERSITY OF CALIFORNIA, SAN DIEGO** - Revelle College ▪ La Jolla, CA

Bachelors of Science in Chemistry (Major GPA: 3.91)

▪ **UCSD Physical Sciences Departmental Dean's Award** ▪ *Top 1% for excellence in research*

▪ **Phi Beta Kappa Honors Society** ▪ *Top 2.3% of senior UCSD students for holistic academic excellence*

RESEARCH EXPERIENCE

Marks Lab – Inorganic Chemistry Evanston, IL ▪ December 2016 – Present

Graduate Student (focus: characterization of mixed valent catalysts and block copolymers)

- Expanded active catalysts to contain multiple metal centers
- Explored metal-metal communication in complex trinuclear complexes
- Designed, synthesized, and characterized mixed valent lanthanide complexes
- Fully assigned the structure of block copolymers with an array of 2D NMR techniques
- Ideated and executed research projects independently with minimal oversight
- Learned computational techniques through intensive personal study and independent direction
- Synthesized highly air sensitive materials via Schlenk and static highvacuum ($1x10^{-6}$ torr) techniques

Tezcan Lab - Bioinorganic Chemistry La Jolla, CA ▪ May 2013 – July 2016

Undergraduate Research Assistant (project: protein-protein interactions in nitrogenase)

- Independently generated and characterized mutants critical for studying nitrogenase
- Performed anaerobic harvest and rigorous enzyme purification via FPLC
- Collaborated to devise and optimize novel assays for product analysis
- Ran kinetic assays to assess the effect of personally prepared mutants

---

OTHER EXPERIENCE

Science Education Training

- Progressed through extensive coursework on education policy and science education research
- Studied the cognitive theory of learning and pedagogical barriers to efficient learning
- Went onsite at underserved schools in San Diego to assist teachers

Head Teaching Assistant ▪ Spring 2015 – Spring 2016

- Independently led discussion sections of 40-50 students in General Chemistry I & III
- Created and graded quizzes and exams, as well as held weekly review sessions for 200 students
- Guided students through both the theory and practice of various general chemistry experiments

Science in the Classroom ▪ Fall 2016 – Spring 2018

- Performed science demos for 3rd and 4th graders in Chicago
- Sparked excitement in science for students in underserved schools through hands on learning

ChemUnity mentor ▪ Fall 2017 – Fall 2018

- Matched with a first year student to serve as a personal and professional mentor

Lab Safety Officer ▪ Fall 2018 – present

- Organized recurring lab clean-ups to inventory & dispose of chemicals, and repair equipment
- Identified lab hazards and developed solutions to improve safety while maintaining efficiency
- Collaborated in rewriting safety protocols for use of highly pyrophoric materials
- Implemented replacements for mercury bubblers using oil without any loss of function

---

PUBLICATIONS

Tezcan Lab: Prepared nitrogenase surface mutants were characterized through kinetic and crystallographic studies to assess the effect of an electrostatic interaction on formation of an encounter complex and secondary sphere effects on turnover.

- C.P. Owens, F.E.H. Katz, **C.H. Carter**, M.A. Luca, F.A. Tezcan. Evidence for Functionally Relevant Encounter Complexes in Nitrogenase Catalysis, *J. Am. Chem. Soc.*, **2015**, 137 (39), 12704-12712 (10.1021/jacs.5b08310)
- C.P. Owens, F.E.H. Katz, **C.H. Carter**, O.F. Victoria, and F.A. Tezcan. Tyrosine-Coordinated P-Cluster in G. diazotrophicus Nitrogenase: Evidence for the Importance of O-Based Ligands in Conformationally Gated Electron Transfer, *J. Am. Chem. Soc.*, **2016**, 138 (32),10124-10127 (10.1021/jacs.6b06783)

Marks Lab: Incorporation of multiple metal centers into known redox "non-innocent" complexes to increase the number of easily accessible redox states and thus make multi-electron reactions more tractable for first row metals, and to study electronic and structural effects of extended nuclearity on metal-metal communication.

- **C. H. Carter**, T. Jurca, Y. Gao, T. J. Marks. Bis-Ferrocenyl-Pyridinediimine Trinuclear Mixed-Valent Complexes with metal-Binding Dependent Electronic Coupling: Synthesis, Structures and Redox-Spectroscopic Characterization, *J. Am. Chem. Soc.*, **2020**, *142, (43), 18715-18729* (10.1021/jacs.0c10015)
- **C. H. Carter**, Y. Kratish, T. J. Marks. Influence of Rare Earth Ion Radius on Metal-Metal Charge Transfer in Trinuclear Mixed-Valent Complexes, *submitted*

Independent: Review of literature and personal experiences with solving common safety hazards in synthetic chemistry, with recommendations for both safety professionals and practicing chemists

- **C. H. Carter**, M. Blayney. Improving Syntheses of Tetraaryl Borates: Recommendations from the Literature, *in preparation*

- **C. H. Carter**, B. Williams, M. Blayney. Evaluation and Recommendations of Modern Oil Replacements for Mercury Bubblers. *In preparation*

RECENT PRESENTATIONS

Chemical Institute of Canada: Global Inorganic Weekday Discussions Online Symposium

(July 7-8, 2020)

Worchester Polytechnic Institute guest lecture: An "Orbital Lego" approach to molecular design

(June 11, 2020)

Catalysis Club of Chicago Symposium

(Aug 27-28, 2020)

Open Science Presentations

(March 26, 2021)

Just Another (Chemistry) Webinar Series

(April 20, 2021)